

POLITECNICO DI MILANO

DEPARTMENT OF CIVIL AND ENVIRONMENTAL ENGINEERING

DOCTORAL PROGRAMME IN ENVIRONMENTAL AND INFRASTRUCTURE
ENGINEERING, XXXV CYCLE



POLITECNICO
MILANO 1863

Aerodynamic noise generation by perforated plates in ducts

Supervisor & Tutor:
Prof. Stefano MALAVASI

Doctoral dissertation of:
Luca Nicola QUARONI

Co-supervisor:
Prof. Islam RAMADAN

The Chair of the Doctoral Programme:
Prof. Monica RIVA

ACADEMIC YEAR 2022-2023

Alle mie nonne, Maria e Mariella

Abstract

This thesis deals with broadband aerodynamic noise generation by perforated plates with circular holes in ducted flows. In particular, the cases of incompressible flow in rectangular ducts and that of subsonic flow in pipes are treated. Through theoretical considerations based on the available literature, it is shown that the aerodynamically-generated internal acoustic pressure field may be partly modified in terms of its higher-order modal components by a careful choice of the disposition of the perforations in the plate, especially in the case of incompressible flows. An experimental campaign in a low Mach number test facility allows to validate this theoretical finding by estimation of the higher-order modal components of the emitted acoustic power for different orifice dispositions in a rectangular plate. To test whether this effect is limited to incompressible flows, a second experimental campaign is performed on a new test bench allowing for up to sonic conditions to be reached in the flow *vena contracta*. The validation of the newly-setup plant is described and the results of tests on perforated plates with different combinations of orifices' number, disposition and thickness are reported. Due to the presence of whistling for most of the geometries, no general remarks could be made on the influence of such parameters on broadband noise generation. However, the importance of the higher-order modes in the only case for which no whistling was detected is highlighted by coherence estimates of the wall pipe pressure fluctuations measured by sensor pairs at the same cross-section, far downstream of the perforated plate under test.

Keywords: perforated plates, aerodynamic noise, higher-order acoustic duct modes.

Acknowledgments

A PhD. is not too different from a journey. While we travel to discover new places and seek new experiences, more often than not what sticks with us the most are the people we've shared the trip with: those who were there from the beginning and those who we met along the road. We are, after all, social animals. In much the same way, while pursuing a PhD. has been an adventure in and by itself, what I'll probably remember the most are the people I've shared this adventure with. In one way or another, all these people have helped me make this journey a successful and memorable one. I'll try my best in this short note to thank them all for their support.

I wish to first thank my supervisor Prof. Stefano Malavasi, who believed in me enough to propose a PhD. thesis and who let me choose my research path and style independently. Secondly, my heartfelt thanks go to Prof. Islam Ramadan from Université de Poitiers, whom I met during my research stay in France and who co-supervised this thesis. His support has been instrumental: I can safely say that I wouldn't have obtained the same results weren't for his help, patience, and assistance. My thanks then go to Gabriele Mazzaro of Pibiviesse Srl, who very helpfully assisted me in the difficult task of setting up the new experimental setup at Politecnico di Milano. I want then to thank Prof. Emmanuel Perrey-Debain from Université de Technologie de Compiègne, who happily supported my exchange and with whom I shared many insightful discussions. I cannot then of course forget about my 'home' and my 'abroad' laboratory groups, with whom I shared many laughs and some misadventures. At 'home': Stefano, Davide (the two), Chiara, Leo, Daniel, Jack, Gian and Marco. 'Abroad': Simon, Alex (the two), Cristophe, Gregoire, Youcef, Camille, Amine and Carlos.

Finally, my thanks go to the people who were there from the beginning and

have been there ever since: my mother, my brother Andrea, my ‘brother-from-another-mother’ Marcello, and my friends Valentina, Davide, Pawl and Marzia.

Contents

List of Figures	viii
List of Tables	xvi
1 Introduction	1
1.1 Problem statement	1
1.2 Aims and methods	2
1.3 Original contributions	2
1.4 Structure	3
2 Background	4
2.1 Flow through perforated plates	4
2.1.1 Overview	4
2.1.2 Parameters affecting the flow through perforated plates	6
2.1.3 Normal working conditions	8
2.1.4 Choking	11
2.1.5 Determination of <i>vena contracta</i> pressure	12
2.2 Aerodynamic generation of sound	13
2.2.1 Free turbulent flows	13
2.2.2 Presence of solid surfaces	14
2.2.3 Whistling	16
2.3 Sound propagation in ducts	16
2.3.1 Modal decomposition	16
2.3.2 Modal shape functions	17
2.3.3 Cut-off modes	20
2.3.4 Influence of uniform flow	21
2.3.5 General solution for acoustic source distribution in a duct	22

2.4	Coincidence in circular pipes	22
3	Constriction noise in ducts: available theory and developments	25
3.1	Incompressible flows	25
3.1.1	Obstacles perpendicular to the flow	26
3.1.2	Generalized spectrum models	28
3.1.3	Pressure fluctuations on the surface of an orifice plate	32
3.2	Subsonic flows	33
3.2.1	General solution for a ducted quadrupole distribution	33
3.2.2	Experimental works	35
3.3	Selective modal excitation	39
3.3.1	Further developments for low Mach number flows . . .	39
4	Noise generation in ducted low Mach number flows through perforated plates	41
4.1	Experimental setup and measurement techniques	41
4.1.1	General characteristics	42
4.1.2	Plate geometries tested	43
4.1.3	2N-port method and setup	45
4.1.4	PIV setup and procedure	49
4.2	Preliminary work	51
4.2.1	Pressure losses	51
4.2.2	Microphones calibration	52
4.2.3	Acoustic behavior of empty duct	53
4.2.4	PIV validation on empty duct	56
4.3	Results	57
4.3.1	Added resistance of tested perforated plates	57
4.3.2	Noise generation	58
4.3.3	PIV Results	69
4.4	Summary	74
5	Noise generation by subsonic flow through perforated plates in a pipe	76
5.1	Experimental setup and methods	76
5.1.1	General characteristics	76
5.1.2	Plate geometries tested	80
5.2	Validation of the experimental setup	83
5.2.1	Background noise	83
5.2.2	Wall pressure fluctuations in empty pipe	84
5.3	Results	93
5.3.1	Thick multi-orifice perforated plate	94
5.3.2	Effect of relative thickness, orifice number and disposition	102

5.4	Summary	110
6	Conclusions	112
6.1	Main findings	112
6.2	Possible developments	113
	Bibliography	114
	Appendices	124
A	Appendix: ‘liquid pressure recovery factor’ calculation	124
A.1	Experimental setup and methods	124
A.1.1	Determination of F_L	125
A.1.2	Test conditions	126
A.2	Results and discussion	126
A.2.1	Cavitating behavior of A1-V1 plate	130
B	Appendix: recessed sensors characterization	132
B.1	Experimental setup and methods	132
B.2	Results	134

List of Figures

2.1	Example of a multi-orifice perforated plate to be inserted between two pipe flanges.	4
2.2	Scheme of flow through orifice plate.	5
2.3	General circular perforated plate geometry with relevant cross-sectional quantities.	6
2.4	From left to right: sharp-edged, rounded and chamfered plate edges with relevant geometrical quantities.	7
2.5	Equivalent nozzle within the flow through an orifice plate. . .	8
2.6	Displacement and expansion of the <i>vena contracta</i> for increasing Mach numbers (M_{vc}) in compressible flow through a thin sharp-edged perforated plate.	11
2.7	Infinite duct of rectangular cross-section with reference system.	17
2.8	Colour plot of the characteristic function ψ_{10} for a rectangular duct with an aspect ratio $b/h = 2$. The vertical nodal line is visible as white at the center while the sign of the acoustic pressure fluctuation p'_a is indicated at the center of each half of the section.	18
2.9	Colour plot of the distribution of mode (1,0) along the wall of a rectangular duct.	18
2.10	Colour plot of the characteristic function ψ_{10} for a circular pipe. The vertical nodal line is highlighted in white at the center while the sign of the acoustic pressure fluctuation p'_a is indicated at the center of each half of the section.	19
2.11	Colour plot of the distribution of 'spinning' mode (1,0) at the wall of a pipe.	20
2.12	Dispersion curve for the first four propagating modes in a pipe of 1 inch diameter.	21

2.13	Vibrational modal shapes of a pipe. Original pipe section in dotted gray, displacements at two time instants in black and blue. The indices indicate the mode (p, q) as defined in (2.47).	23
2.14	Acoustic power radiation from a thin walled pipe section downstream of a 90° mitred bend. Cut-on frequencies are also highlighted. Adapted from Bull & Norton [29].	23
3.1	Obstacle perpendicular to the flow in an infinite-length rectangular duct, relative coordinate systems and planar velocity components.	26
3.2	Generalized spectrum $K^2(St)$ for different spoiler widths and different constriction velocities, adapted from Nelson & Morfey [30].	30
3.3	Best-fit generalized spectrum for orifice plates as suggested by Kårekull et al. [35]	31
3.4	Power spectral density of the pressure fluctuations along the non-dimensional radius, adapted from Tao et al. [36]. Upstream side (left), downstream side (right). The position of the measurements are highlighted in green (upstream) and violet (downstream).	32
3.5	Proportionality between the non-dimensional far-field acoustic power Q downstream of a finite volume of isotropic turbulence in a rectangular duct and the product of a non-dimensional frequency β and the flow Mach number, from Davies & Ffowcs-Williams [38].	35
3.6	Possible visualization of circumferential instabilities of the vortex ring generated downstream of an orifice flow, as supposed by Kerschen & Johnston [40].	36
3.7	Power spectral density of fluctuating pressure at the wall at various non-dimensional distances $X = x_3/D_i$ downstream of an orifice subject to subsonic flow conditions, adapted from Agarwal [41].	38
4.1	Schematic of the low Mach number aeroacoustic test bench at the Roberval Laboratory of the University of Technology of Compiègne (UTC).	42
4.2	View of the Venturi-like flow meter upstream of the measurement section.	43
4.3	Measurement section and PIV setup	43
4.4	Sketch of orifices' positions of tested plate configurations.	44
4.5	Integration area (in red) to be applied in (3.25) (red) over checkerboard pattern of $ \psi_{11}(x'_1, x'_2) ^2$ for plates A1, A2-V1 and A4 from left to right.	45

4.6	Integration area (in red) to be applied in (3.25) over checker-board pattern of $ \psi_{10}(x'_1, x'_2) ^2$ for plates A2-V2, A2-V1 and A2-V3 from left to right.	45
4.7	Scheme of measurement sections for the 2N-port method in a duct.	46
4.8	Upstream part of the measurement section with movable loud-speaker mounted in one of the $N = 10$ positions on the upstream of the obstacle.	47
4.9	Scheme of the measurement section and the position of the microphones.	47
4.10	Fog generator discharging glycerine directly into the blower for PIV acquisitions.	50
4.11	Schematic showing the size and the position of the PIV measurement area with respect to orifice plate configuration. . . .	51
4.12	Average duct velocity v.s. squared root of measured and predicted test line pressure loss by employing 'an equivalent length' L_{eq} of 71 m of rectangular duct.	52
4.13	Phase calibration with respect to reference microphone with GRAS 51AB.	53
4.14	Amplitudes of the complex reflection coefficients (left) and transmission coefficient (right) for the plane wave (0,0) mode in both upstream to downstream and downstream to upstream directions.	55
4.15	Amplitudes of the complex upstream reflection coefficients (left) and upstream to downstream transmission coefficient (right) for the plane wave (0,0) mode for two average duct velocities.	55
4.16	Phase of the upstream to downstream transmission coefficient for the plane wave (0,0) mode for two different average duct velocities and for the no-flow case.	56
4.17	Average velocity amplitude (up, left) and average turbulence kinetic energy (up, right) on a visualization area of 185 x 185 mm as obtained through a 2D PIV setup. Convergence of average velocity amplitude (bottom, left) and turbulence kinetic energy (bottom, right) at a point in the flow visualization area.	57
4.18	Dimensional (left) and non-dimensional (right) relationship between pressure drop and averaged duct velocity for all plates tested.	58
4.19	Spectra of the absolute difference between upstream and downstream Sound Power Level (SWL) for the A1, A2-V1 and A4 plates at $M_j = 0.13$. Cut-on frequencies of higher order modes are also reported as dashed red lines; ± 2 dB band is highlighted in green.	59

4.20	Non-dimensional upstream acoustic power versus the jet Mach number M_j (log-scale) for constant Helmholtz numbers (top) and constant Strouhal numbers (bottom).	61
4.21	Upstream SWL spectrum at different mass flow rates for plate A4. Cut-on frequencies are highlighted in red.	62
4.22	Upstream SWL spectrum at $M_j = 0.13$ for plates A1, A2-V1 and A4. Cut-on frequencies are highlighted in red.	63
4.23	Generalized source spectra K^2 for (left) A4 plate at various jet Mach numbers and for plates A1, A2-V1 and (right) A4 at $M_j = 0.13$	64
4.24	Generalized source spectra K^2 for plates A1, A2-V1 and A4 at $M_j = 0.13$ v.s. the best fit.	65
4.25	Comparison of modal efficiency coefficient Ψ_{mn} between (left) plates A1, A2-V1 and A4 and (right) between plates A2-V1, A2-V2 and A2-V3 for the eight propagating acoustic modes in the duct in the frequency range 200 Hz to 3200 Hz.	65
4.26	Upstream modal SWL of all propagating modes in the frequency range [200 Hz, 3200 Hz] for the three main plate geometries A1, A2-V1 and A4 at the maximum mass flow rate tested ($M_j = 0.13$). (colors online)	67
4.27	Upstream modal SWL of all propagating modes in the frequency range [200 Hz, 3200 Hz] for the three two-orifice plate geometries A2-V1, A2-V2 and A2-V3 for the maximum mass flow rate tested ($M_j = 0.13$). (colors online)	68
4.28	Frame couple for PIV ‘instantaneous’ velocity field over the A2-V1 left orifice. Notice that the image on the right is brighter for the higher exposure time. The reflection of the lens’ ring is also visible on the same picture for the same reason.	69
4.29	Relative error between cumulative average at i -th image couple and final average value of: the mean flow velocity magnitude (left) and the turbulence kinetic energy (right) at a point located (49 mm, 30 mm).	70
4.30	Normalized mean flow velocity magnitude for plates A1 to A4 from left to right for $M_j = 0.13$ Values range from 1 (dark red) to 0 (dark blue). Solid surface is represented in gray and orifice’s position in white.	71
4.31	Normalized mean turbulence kinetic energy field for plates A1 to A4 from left to right for $M_j = 0.13$ Values range from 1 (dark red) to 0 (dark blue). Solid surface is represented in gray and orifice’s position in white.	71
4.32	Normalized mean vorticity field for plates A1 to A4 from left to right for $M_j = 0.13$ Values range from 1 (dark red) to -1 (dark blue). Solid surface is represented in gray and orifice’s position in white.	71

4.33	Squared-RMS of the normal velocity fluctuations at (top left)-(bottom left) 2 mm upstream, and (top right)-(bottom right) downstream for the tested orifice plates and a mass flow rate of 610 kg/h at the positions indicated in Figure 4.11. Vertical dashed lines correspond to the nondimensionalized ring's width.	73
5.1	Schematic of the experimental test bench for subsonic airflows at the Polytechnic University of Milan.	77
5.2	Overview of the experimental test bench for subsonic airflows at the Polytechnic University of Milan.	77
5.3	Schematic of the experimental test bench for subsonic airflows at the Polytechnic University of Milan.	78
5.4	Schematic of installation for the piezoelectric pressure sensors at section E-E' and disposition along the cross section.	79
5.5	Sections B-B', C-C' and D-D' (left) and section E-E' (right).	79
5.6	Scheme for identification of the characteristics of the perforated plate geometries in Table 5.3 and Table 5.4.	81
5.7	Background noise PSD of vibro-acoustic sensors in the relative dimensional units in the range 500 Hz to 20 kHz with a frequency resolution of 100 Hz.	84
5.8	Interpolating curve for tabular values of the attenuation \hat{C} of the measured wall pressure spectrum \hat{S}_{pp}^{msrd} of a turbulent boundary layer relative to the 'true' value \hat{S}_{pp}^{true} if no spatial averaging were present. Adapted from Corcos [64].	86
5.9	Magnitude-squared coherence $\hat{\gamma}_{s_1, s_2}^2$ between the two flush-mounted condenser microphones at sections C-C' and D-D' of Figure 5.3 for a pipe flow with average Mach number $M = 0.049$. Frequency resolution of 100 Hz.	87
5.10	Signal-to-noise ratio (SNR) of the two flush-mounted condenser microphones at sections C-C' (GRAS1) and D-D' (GRAS2) of Fig. 5.3 for a pipe flow with average Mach number $M = 0.049$. Frequency resolution of 100 Hz.	87
5.11	Non-dimensional PSD of the wall pressure fluctuations at section C-C' for pipe flow with Mach numbers from 0.049 to 0.074.	88
5.12	Schematic of the cylindrical Helmholtz' resonator resulting from the recessed installation of the fluctuating pressure sensor. Equivalent mass-spring system on the right.	89
5.13	Installation requirements for recessed configuration of piezoelectric pressure sensor PCB 113B28 as indicated by the manufacturer. Dimensions outside of square brackets are in centimeters.	90
5.14	Piezoelectric sensor PCB 113B28 dimensions as provided by the manufacturer. Dimensions outside of square brackets are in millimeters.	90

5.15	Magnitude-square coherence $\hat{\gamma}_{s_1, s_2}^2$ between the piezo-electric sensors PCB1-PCB2, PCB2-PCB3 and PCB1-PCB3 at section E-E' of Figure 5.3 for a pipe flow with average Mach number $M = 0.049$. Frequency resolution of 100 Hz.	91
5.16	piezo-electric sensors PCB1, PCB2 and PCB3 at section E-E' of Figure 5.3 for a pipe flow with average Mach number $M = 0.049$. Frequency resolution of 100 Hz.	91
5.17	Non-dimensional PSD of the wall pressure fluctuations at section E-E' as recovered by the sensor PCB1 for empty pipe configuration and Mach numbers from 0.048 to 0.074.	92
5.18	Non-dimensional PSD of the wall pressure fluctuations at section E-E' as recovered by the sensor PCB1 for empty pipe configuration and Mach numbers from 0.048 to 0.074 with no frequency scaling.	93
5.19	Mass flow rate \dot{m} versus Nozzle Pressure Ratio (NPR) (left) and versus the jet Mach number M_j (right) for 'thick' plate C4 with fixed upstream pressure of 2.5 barA.	94
5.20	Resistance coefficient K_L against the jet Mach number M_j of plate C4 for the tested conditions.	95
5.21	Discharge coefficient of plate C4 for incompressible and subsonic flow.	95
5.22	PSD of pipe wall pressure fluctuations at sections C-C' and D-D' for $M_j \approx 0.75$ for C4 plate. Cut-on frequencies of higher-order modes are included as dashed red lines. Bandwidth 100 Hz.	96
5.23	PSD of wall pipe pressure fluctuations at sections C-C' and D-D' for $M_j \approx 0.75$ for C4 plate and same quantity for equivalent flow through empty pipe (same average duct Mach numbers $Ma \approx 0.06$). Cut-on frequencies of higher-order modes are reported as dashed red lines. Bandwidth 100 Hz.	96
5.24	Total emitted acoustic power W_a against jet Mach number M_j for the plane wave-only frequency range $500 \text{ Hz} \leq f \leq 8 \text{ kHz}$ for the 'thick' perforated plate C4.	97
5.25	Magnitude-squared coherence $\hat{\gamma}_{s_1, s_2}^2$ and relative phase $\hat{\theta}_{s_1, s_2}$ between sensor pairs at section E-E' for $M_j \approx 0.75$ and C4 plate. Cut-on frequencies are indicated as dashed red lines. Bandwidth 100 Hz.	98
5.26	Acoustic pressure distribution of mode (1,0) (top) and mode (2,0) (bottom) at two time instants t_1 and t_2 for section E-E'.	99
5.27	Colour plot of the distribution of pressure fluctuations for a standing azimuthal mode (1,0) along the walls of a pipe. Propagation of the wave is from left to right.	100

5.28	Signal-to-noise ratio (SNR) for accelerometer positioned $\approx 45D_i$ downstream of perforated plate both in the presence of the C4 plate and in the empty duct configuration. Cut-on frequencies are indicated as dashed red lines. Bandwidth 100 Hz.	101
5.29	Magnitude-squared coherence $\hat{\gamma}_{s1,s2}^2$ between each sensor at section E-E' and the accelerometer positioned $\approx 45D_i$ downstream of perforated plate. Cut-on frequencies are indicated as dashed red lines. Bandwidth 100 Hz.	102
5.30	Non-dimensional mass flow rate \dot{m}^* versus squared root of the relative pressure drop (\sqrt{x}) for all tested geometries at the two relative thicknesses $t^* = 0.4$ (top) and $t^* = 1$ (bottom).	103
5.31	Resistance coefficient (K_L) versus squared root of the relative pressure drop (\sqrt{x}) for all tested geometries for the two relative thicknesses $t^* = 0.4$ (top) and $t^* = 1$ (bottom).	104
5.32	Mechanism of reattachment of the flow due to the expansion of the <i>vena contracta</i> for increasing jet Mach numbers. On the left, a 'transitional' plate, on the right a 'thick' plate.	105
5.33	Resistance coefficient K_L against the squared root of the relative pressure drop \sqrt{x} of plates A1-V1 and B1-V1.	105
5.34	Color map of the non-dimensional PSD \hat{S}_{pp} at section D-D' for increasing squared root of the relative pressure drop \sqrt{x} for 'A' plates ($t^* = 0.4$).	107
5.35	Color map of the non-dimensional PSD \hat{S}_{pp}^* at section D-D' for increasing squared root of the relative pressure drop \sqrt{x} for 'B' plates ($t^* = 1$).	108
5.36	Resistance coefficient K_L superposed on the colour map of the non-dimensional PSD \hat{S}_{pp}^* at section D-D' for increasing squared root of the relative pressure drop \sqrt{x} for A1-V1 plate (left) and for B1-V1 plate (right).	109
5.37	Dimensional PSD \hat{S}_{pp}^* for a microphone at section D-D', magnitude-squared coherence $\hat{\gamma}_{s1,s2}$ and relative phase $\hat{\theta}_{s1,s2}$ between two sensors 180° apart at section E-E'. Frequency resolution of 100 Hz.	110
A.1	Scheme of 'Control Valve' experimental test bench.	125
A.2	Flow rate Q versus squared root of the pressure drop $\sqrt{\Delta p_R}$ between $2D$ upstream of the 'A' plates and $6D$ downstream for different openings of the downstream throttling valve and an absolute upstream pressure of $p_{1,s} = 9$ barA. Fitting line for computing C_V is highlighted in red.	128

A.3	Flow rate Q versus squared root of the pressure drop $\sqrt{\Delta p_R}$ between $2D$ upstream of the ‘B’ plates and $6D$ downstream for different openings of the downstream throttling valve and an absolute upstream pressure of $p_{1,s} = 6$ barA. Fitting line for computing C_V is highlighted in red.	129
A.4	Flow rate Q versus squared root of the pressure drop $\sqrt{\Delta p_R}$ between $2D$ upstream of the C4 plate and $6D$ downstream for different openings of the downstream throttling valve and an absolute upstream pressure of $p_{1,s} = 9$ barA. Fitting line for computing C_V is highlighted in red.	130
A.5	Trend of loss coefficient K_L against pipe Reynolds number Re_p and cavitation number σ for plate A1-V1 subject to different upstream pressures $p_{1,s}$	131
B.1	External acoustic source (loudspeaker) installed at the upstream end of the downstream pipe of the AirLab’s test line.	132
B.2	Block diagram of PCB piezoelectric sensors measurement chain.	133
B.3	PSD of Gaussian white noise fed to the loudspeaker. Frequency resolution of 50 Hz.	134
B.4	Frequency response function of the system composed of power amplifier, loudspeaker and pipe within the frequency range 1-18 kHz. Frequency resolution of 50 Hz.	135
B.5	Frequency response function of the system composed of power amplifier, loudspeaker, pipe and PCB sensors within the frequency range 1-18 kHz. Frequency resolution of 50 Hz.	136
B.6	Frequency response functions of the PCB sensors within the frequency range 1-18 kHz. Frequency resolution of 50 Hz.	136

List of Tables

2.1	Solutions to $J'_m(\chi_{mn}) = 0$ for the first 7 modes.	19
4.1	Characteristics of the tested perforated plates	44
4.2	Cut-on frequencies for all propagating modes within the range 200 Hz to 3200 Hz for the rectangular duct under consideration.	48
4.3	Power law exponents at different constant Helmholtz and Strouhal numbers for the main plate geometries tested.	62
5.1	Characteristics of the instruments employed for the measure- ment of fluid-dynamic quantities at the experimental plant in the Polytechnic University of Milan.	80
5.2	Cut-on frequencies of the higher-order modes in the frequency range $500 \text{ Hz} \leq f \leq 20 \text{ kHz}$ for test-line pipe ($D_i = 24.3 \text{ mm}$) and no flow at ambient conditions.	80
5.3	Geometry, plate ID, position of the first orifice starting clock- wise from point A to point A' of Figure 5.6 and relative thick- ness of the one-holed and two-holed plates. Symmetry for the other perforations as indicated in the relative schemes.	82
5.4	Geometry, plate ID, position of the first orifice starting clock- wise from point A to point A' of Figure 5.6 and relative thick- ness of the four-holed plates. Symmetry for the other perfor- ations as indicated in the relative figures.	83
A.1	Summary of the results of the experimental campaign on the 'Control Valve' hydraulic loop.	127

*“Since things in motion sooner catch the eye
Than what stirs not.”*

(Troilus and Cressida, Act 3, Scene 3, 189-190 - William Shakespeare)

1.1 Problem statement

The fact that air flows generate sound under specific conditions has been known to humans from time immemorial, as the use of wind instruments in prehistoric societies testifies [1]. However, it is not until the 1950s that scientific theories have been developed to study the mechanisms behind such phenomenon [2]. This is because the issue of generating high levels of aerodynamic noise rose in importance only after the introduction of jet engines in commercial aircrafts. Their high sound emissions in fact prompted engineers to find ways to mitigate this phenomenon. To stress this fact, aerodynamically generated sound is usually referred to also as ‘noise’ instead of ‘sound’.

While developed principally in the field of aviation, the problem of aerodynamic generation of noise is by no means limited to such domain [3]. In many fluid-dynamic processes in fact, there is the need to perform some sort of flow rate control. In pipe and duct systems, this is usually done through the use of valves, which come under many different shapes and formats [4]. Their basic mechanism is to cause localized energy losses through flow constrictions so as to dissipate excess energy. This allows in turn to decrease the flow rate that the flow is able to convey. The majority of the energy is dissipated to heat through viscosity. However, a small part of it is converted into sound [5, 6]. The generated acoustic pressure waves then travel along the system and are transmitted to the outside environment through the vibrations of the ducts’ walls [7]. Due to the particular way in which acoustic waves propagate in closed systems (with non-homogeneous distributions over the cross-section known as higher-order modes), the internal flow geometry of the flow control device (e.g. valve) may selectively enhance or hinder sound propagation for a given frequency range [8]. Furthermore, for the case of pipes, such higher-order modes contribute particularly to the

noise transmitted to the outside environment [9]. A better understanding of the influence of the valve geometry on the generated acoustic field within the pipe/duct may hence permit the development of devices which mitigate sound production and/or its transmission to the outside environment.

1.2 Aims and methods

The present work is an attempt to gain a more robust understanding of the effects of a flow control device's geometry on its broadband aerodynamic noise generation. Due to the large variety of flow control devices available, it has been chosen to focus on the case of perforated plates. Such devices in fact display the same basic phenomena found in more complicated ones (e.g. flow constriction, noise generation) while keeping the geometry simpler and more amenable to a deeper analysis of the governing geometrical parameters.

The chosen approach is a blend of theoretical and experimental work: the available theory on the subject is used as guidance in the choice of the parameters most probably affecting noise generation. Experiments are then performed to validate the theoretical findings and to provide a useful reference for additional works on the topic.

In particular, two air flow conditions have been considered in the analysis. Firstly, the case for which compressibility effects are negligible due to the low velocities within the flow when compared to the speed of sound in the fluid. Such condition is common in Heating, Ventilation and Air Conditioning (HVAC) systems and will be referred to in the following as 'incompressible flow'. It has to be highlighted here that such a definition relates to the fluid-dynamic behavior of the flow, and not to the acoustic one. Secondly, the case for which compressibility effects are important but where the maximum local velocity is anyway less than the local speed of sound. Such case is common in the Oil & Gas (O&G) industry, where control valves usually operate up to the point where sonic conditions are reached. In the following, such flow regime will be referred to as 'subsonic flow'.

1.3 Original contributions

The present work provides some original contributions to the body of knowledge on the topic of broadband noise generation by flow through perforated plates. In particular, it is shown that, at least in the incompressible flow range, the modal content (in terms of higher-order acoustic modes) of the generated broadband noise can be modified through a choice of the position/number of the orifices in a perforated plate. A qualitative 'modal efficiency coefficient' for a preliminary characterization of the aptitude of

a given orifice geometry in exciting a specific higher order mode (m, n) is derived based on considerations on the available knowledge from the literature. An experimental campaign on an incompressible flow facility allows to obtain the generated acoustic power of a series of perforated plates as well as their modal composition. Finally, a new experimental test bench for the characterization of the acoustic emissions by subsonic flows through perforated plates is set up and validated.

1.4 Structure

The thesis is structured as follows. Chapter 2 discusses the necessary background to the present work, with a particular emphasis on the characteristic quantities related to the flow through perforated plates, the main mechanisms of aerodynamic noise generation and the propagation of sound in ducts. In Chapter 3, the available models for broadband noise generation by flow constrictions are treated in more detail and some indications on a possible noise reduction strategy based on a ‘selective modal excitation’ of the higher-order modes are made. In Chapter 4, this ‘selective model’ is tested through an experimental campaign involving an incompressible flow through perforated plates in a rectangular duct (HVAC case). In Chapter 5, the effect of orifice position/number are instead studied through experimental tests on subsonic flows through circular perforated plates. Finally, the main findings and possible future developments are summarized in Chapter 6.

The present chapter provides a theoretical background for the work discussed in the thesis. A description of the incompressible and compressible flow through perforated plates is first provided. Then, the basics of aerodynamic sound generation by unconfined turbulence are recalled. The propagation of sound waves in ducts filled with an ideal gas are also described, with a particular emphasis on the presence of higher-order acoustic modes. Finally, the particular coupling between the wall vibrations in a pipe and the internal acoustic pressure field is introduced.

2.1 Flow through perforated plates

2.1.1 Overview

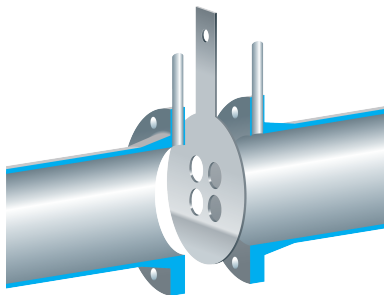


Figure 2.1: Example of a multi-orifice perforated plate to be inserted between two pipe flanges.

Perforated plates (Figure 2.1) are devices used for both control and/or measurement of the flow rate in a wide variety of internal flow systems. They are plates of thickness t with perforations varying in number, shape and

dimension, usually placed perpendicularly to the flow [4, 10]. Their overall shape is dependent on the cross-sectional shape of the duct. The two most common systems present square/rectangular ducts (mainly in HVAC systems) and circular pipes (especially in the O&G sector). The shape of the perforation depends on the application, even though circular holes of constant diameter d_h remain the most common configuration used and is the one investigated in the present work.

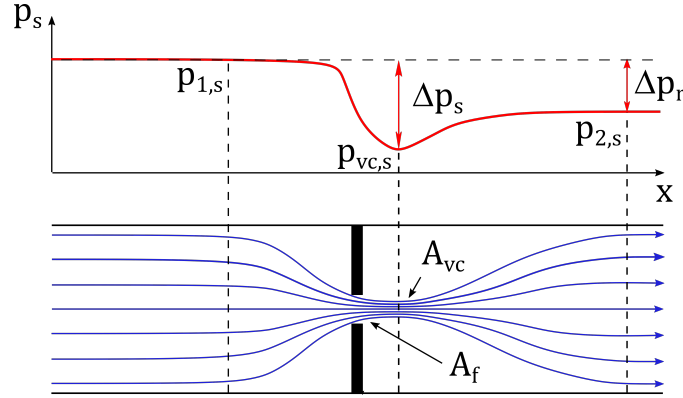


Figure 2.2: Scheme of flow through orifice plate.

Their basic functioning is to accelerate the fluid by constricting the flow through the perforations and letting it then expand downstream of the plate (Figure 2.2). The constriction causes the convected fluid to detach from the upstream edge of the orifice, accelerate and converge up to a section of minimum area, the *vena contracta*, of area A_{vc} (in the case of multiple perforations, A_{vc} is simply the sum of *vena contracta* areas produced by the holes). Depending on the type of fluid and/or flow regime, this acceleration is either at the expense of static pressure p_s (incompressible flows, liquids) or both static pressure and temperature T_s (compressible flows). As the flow expands downstream of the *vena contracta*, a large amount of turbulence is generated and a net pressure loss $\Delta p_R = p_{1,s} - p_{2,s}$ is measured between two sections upstream and downstream of the plate where the flow is fully developed. This is an efficient energy dissipation mechanism, allowing to reduce any excess pressure in the system.

This irreversible pressure loss can be expressed non-dimensionally through subdivision by the dynamic pressure of the incoming flow, obtaining the resistance or loss coefficient [11]:

$$K_L = \frac{\Delta p_R}{\frac{1}{2} \rho_1 U_1^2} \quad (2.1)$$

where U_1 and ρ_1 are the average axial velocity and the average density at

the upstream section. In order to be dimensionless, Δp_R must be in [Pa], ρ_1 in [kg/m³] and U_1 in [m/s]. Another parameter often employed to describe the performance of perforated plates is the discharge coefficient [10]:

$$C_d = \frac{\dot{m}}{\dot{m}_{th}} \quad (2.2)$$

where \dot{m} is the mass flow rate being conveyed and \dot{m}_{th} is the one theoretically obtainable for an ideal, frictionless flow through a nozzle of upstream area A and throat area A_f subject to a static pressure difference Δp_s between the upstream section and the throat. Its expression is different based on the type of flow, i.e. incompressible or compressible, see 2.1.3.

Independently of the fluid however, a limit condition can be reached for which the (mass) flow rate cannot increase by simply decreasing the downstream pressure $p_{2,s}$. This condition is known as ‘choking’ and is further discussed in 2.1.4.

2.1.2 Parameters affecting the flow through perforated plates

The flow through perforated plates is mainly influenced by the fluid properties (density ρ , dynamic viscosity μ and compressibility ε), by a characteristic flow velocity U_c and by some geometrical parameters of the orifices (Figure 2.3): the plate porosity $\phi = A_f/A$, the relative thickness $t^* = t/d_h$, the number and the relative inter-orifice distance or pitch $p_h^* = p_h/d_h$, the relative roundness of the edges $r^* = r/d_h$ (r is the edges’ radius of curvature) and the presence of chamfers (with relative depth $w^* = w/d_h$ and inclination θ), e.g. [10–13].

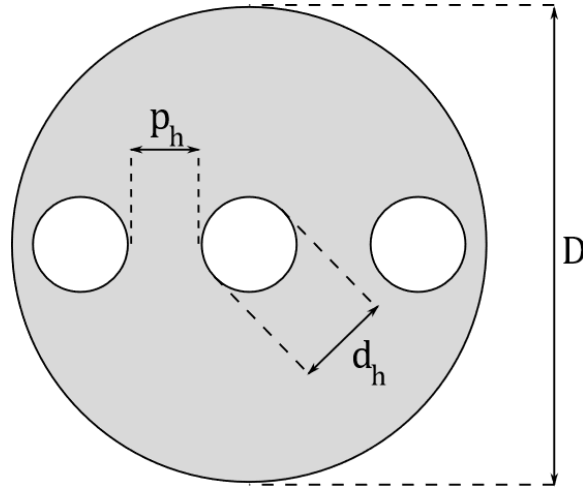


Figure 2.3: General circular perforated plate geometry with relevant cross-sectional quantities.

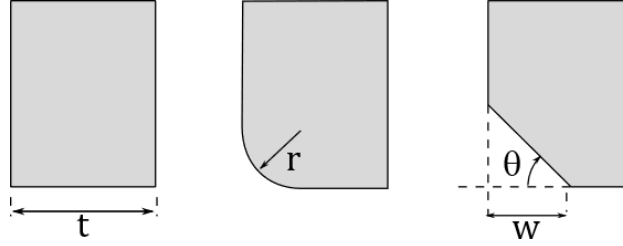


Figure 2.4: From left to right: sharp-edged, rounded and chamfered plate edges with relevant geometrical quantities.

The dependence on the flow regime (laminar, turbulent) is summarized by the Reynolds' number $Re = \rho U_c L_c / \mu$, where L_c is a characteristic length of the problem. This can be for example the pipe diameter D in pipe systems, the hydraulic radius R_h of the duct in the case of non-circular cross-sections or the hole diameter d_h for circular perforations. Though important, the choice of L_c does not change the overall trend observed for the dependence of the flow on Re : the tendency is for the flow to become independent of it once fully turbulent flow conditions are achieved [12]. This translates in constant values of both K_L and C_d after certain threshold values of Re are reached. It can be here also remarked that, from its definition in (2.1), a constant value of the resistance coefficient K_L is also equivalent to a proportionality between the pressure losses and the mass flow rate of the type:

$$\dot{m} \propto \sqrt{\rho_1 \Delta p_R} \quad (2.3)$$

Amongst the geometrical parameters, the plate porosity ϕ is the most influential one as it is the one most directly related to the added resistance opposed to the flow [11]. The relative thickness t^* is related to the flow reattachment past the *vena contracta*. If the bore is short enough ($t^* \leq 0.2$), the diverging flow is not able to reattach within the perforation and reattachment occurs downstream of the plate [14]. If t^* is large enough ($t^* > 0.75/0.8$), the flow expands until reaching the internal wall of the perforation. In this case, the velocity at the exit of the plate is lower than in the case with no reattachment and pressure losses are therefore lower. The number of perforations, and to a lesser extent their positions, if the plate porosity is kept constant, also affect the pressure losses generated by perforated plates [15]. A larger number of orifices in fact translates into a shorter jet length downstream of the perforation, with lower turbulent mixing. Increasing the number of orifices therefore decreases the pressure drop caused by the device. The rounding and the presence of chamfers finally affect the flow through perforated plates by partly preventing the flow from reattaching.

2.1.3 Normal working conditions

The fundamental relations between the fluid-dynamic quantities of interest for the flow through perforated plates are now derived for conditions far from ‘choking’.

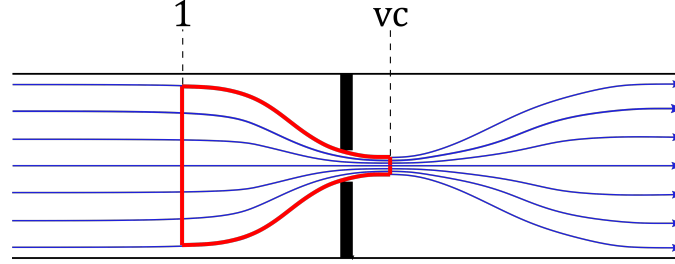


Figure 2.5: Equivalent nozzle within the flow through an orifice plate.

Incompressible case

Referring to Figure 2.5, neglecting energy losses, the energy balance between a section upstream of the perforated plate and the *vena contracta* is:

$$\frac{p_{1,s}}{\rho} + \frac{U_1^2}{2} = \frac{p_{vc,s}}{\rho} + \frac{U_{vc}^2}{2} \quad (2.4)$$

where U_1 is the average flow velocity upstream and $p_{vc,s}$ and U_{vc} are the static pressure and the average velocity in the *vena contracta*. For mass conservation:

$$U_{vc} = \frac{A_1}{A_{vc}} U_1 \quad (2.5)$$

As discussed above, in the case of perforated plates A_{vc} does not correspond to the flow passage area A_f because the flow is still contracting as it enters the perforations. Introducing the ‘vena contracta factor’ Γ_0 :

$$\Gamma_0 = \frac{A_{vc}}{A_f} \quad (2.6)$$

(2.4) can be rewritten in terms of the volumetric flow rate $Q_{th} = A_1 U_1$ passing through the duct, where the subscript ‘*th*’ indicates that this is a theoretical value (i.e. no losses are considered):

$$Q_{th} = \frac{A_1 \Gamma_0 \phi}{\sqrt{1 - \Gamma_0^2 \phi^2}} \sqrt{\frac{(p_{1,s} - p_{vc,s})}{\rho}} = \frac{A_1 \Gamma_0 \phi}{\sqrt{1 - \Gamma_0^2 \phi^2}} \sqrt{\frac{2 \Delta p_s}{\rho}} \quad (2.7)$$

The theoretical flow rate Q_{th} is therefore dependent on the squared root of the static pressure drop Δp_s between an upstream section and the *vena*

contracta section. For Reynolds numbers high enough, Γ_0 reaches a constant value, i.e. the ‘flow geometry’ is the same independently of the flow conditions [16]. For a circular orifice with sharp edges, the following formula is valid for the contraction coefficient Γ_0 [11, 17]:

$$\Gamma_0 = \frac{1}{1 + \sqrt{0.5 \left(1 - \frac{A_f}{A}\right)}} \quad (2.8)$$

For an ideal converging nozzle $\Gamma_0 = 1$ and therefore the expression of the discharge coefficient (2.2) becomes:

$$C_d = \frac{Q}{A_1 \phi \sqrt{\frac{2\Delta p_s}{\rho}}} \sqrt{1 - \phi^2} \quad (2.9)$$

It can also be noticed that, referring to (2.3), as $\rho_1 = \rho = \text{const.}$ and $Q = \dot{m}/\rho$, the flow rate is proportional to the squared root of the pressure loss Δp_R for ‘normal’ working conditions:

$$Q \propto \sqrt{\Delta p_R} \quad (2.10)$$

Compressible case

Compressibility modifies the flow through perforated plates. Assuming an ideal gas flowing adiabatically from the upstream section to the *vena contracta*, the energy balance is:

$$c_p T_{1,s} + \frac{U_1^2}{2} = c_p T_{vc,s} + \frac{U_{vc}^2}{2} \quad (2.11)$$

where c_p is the specific heat at a constant pressure for the ideal gas under consideration. Such a parameter can be also expressed as $c_p = \gamma R/(\gamma - 1)$, where $\gamma = c_p/c_v$, the ratio of the specific heats at constant pressure and volume of the gas under consideration. From which:

$$U_{vc} = \sqrt{\frac{2\gamma R T_{vc,s}}{\gamma - 1} \left(\frac{T_{1,s}}{T_{vc,s}} - 1 \right) + U_1^2} \quad (2.12)$$

If frictional losses can also be neglected, then the isentropic flow relationships are valid:

$$\frac{p_{vc}}{p_1} = \left(\frac{T_{vc}}{T_1} \right)^{\gamma/(\gamma-1)} \quad \frac{p_{vc}}{p_1} = \left(\frac{\rho_{vc}}{\rho_1} \right)^{\gamma} \quad \frac{\rho_{vc}}{\rho} = \left(\frac{T_{vc}}{T_1} \right)^{1/(\gamma-1)} \quad (2.13)$$

If $U_1 \ll U_{vc}$, the U_1^2 term can be neglected too and the static temperature and pressure $T_{1,s}$ and $p_{1,t}$ correspond to the stagnation quantities T_0 and

p_0 . It is also customary to report the ratio between p_{vc}/p_0 as its inverse p_0/p_{vc} , also known as Nozzle Pressure Ratio (NPR). Therefore, the previous equation can be rewritten as:

$$U_{vc} = \sqrt{\frac{2\gamma RT_{vc,s}}{\gamma - 1} \left(\text{NPR}^{\frac{\gamma-1}{\gamma}} - 1 \right)} \quad (2.14)$$

Such expression also provides a way to estimate the Mach number M_{vc} at the *vena contracta* (also referred to as jet Mach number M_j), as the speed of sound at the *vena contracta* is equal to $c_{vc} = \sqrt{\gamma RT_{vc,s}}$:

$$M_{vc} = \frac{U_{vc}}{c} = \sqrt{\frac{2}{\gamma - 1} \left(\text{NPR}^{\frac{\gamma-1}{\gamma}} - 1 \right)} \quad (2.15)$$

The mass flow rate \dot{m} through the perforated plate can be then computed as:

$$\dot{m} = \rho_{vc} \cdot U_{vc} \cdot A_{vc} = \rho_{vc} \cdot U_{vc} \cdot \Gamma_0 A_f \quad (2.16)$$

In an ideal converging nozzle no contraction takes place, i.e. $\Gamma_0 = 1$. The following expression for the discharge coefficient defined in C_d in the case of a compressible flow (2.2) can then be obtained:

$$C_d = \frac{\dot{m}}{A_f \cdot p_{1,t} \cdot \left(\frac{1}{\text{NPR}} \right)^{\frac{\gamma+1}{2\gamma}} \cdot \sqrt{\frac{2\gamma}{(\gamma-1) \cdot R \cdot T_{1,t}} \cdot \left(\text{NPR}^{\frac{\gamma-1}{\gamma}} - 1 \right)}} \quad (2.17)$$

A peculiarity of compressible flows is that now Γ_0 remains dependent on the flow conditions instead of stabilizing around a constant value. In fact, the *vena contracta* expands and retrocedes for increasing NPRs [14], , see Figure 2.6. This translates into a dependence of C_d on the flow conditions, as a variation of the *vena contracta* area corresponds effectively to a variation of the ‘nozzle geometry’ created by the flow.

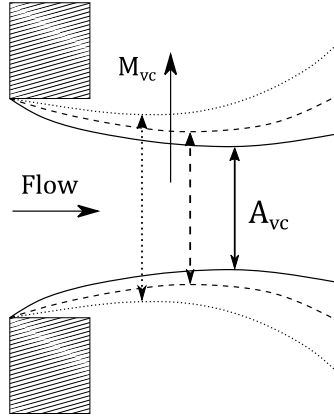


Figure 2.6: Displacement and expansion of the *vena contracta* for increasing Mach numbers (M_{vc}) in compressible flow through a thin sharp-edged perforated plate.

2.1.4 Choking

Incompressible case: cavitation

In liquids, the acceleration of the fluid caused by the constriction is limited by the fact that the pressure in the *vena contracta* $p_{vc,s}$ cannot decrease indefinitely. As $p_{vc,s}$ reaches the saturated vapor pressure p_{vap} at the operating temperature, the pressure is not able to decrease any further. Therefore, any change in $p_{2,s}$ is not ‘felt’ upstream of the *vena contracta* and the flow rate Q is ‘blocked’ at Q_{max} . Furthermore, vapor bubbles start forming in the low pressure area close to the *vena contracta*. As these bubbles are transported downstream, the recovery of pressure occurring as the flow re-expands after the constriction causes such bubbles to implode. Such phenomenon is known as *cavitation* and is a cause for concern for the potential damage caused by the shock pressure waves generated by the collapsing bubbles.

Compressible case: sonic flow

The mass flow rate through a constriction in the case of compressible flows is limited not by a ‘pressure limit’ (as in the case of incompressible flows) but instead by a ‘velocity limit’. If the upstream pressure p_1 is kept constant and the NPR is varied by varying the $p_{vc,s}$ only, then (2.15) predicts that for a given NPR* the speed of sound c is reached in the *vena contracta*, i.e. $M_{vc}(\text{NPR}^*) = 1$. For dry air as an example, $\text{NPR}^* = 1.89$ (as $\gamma = 1.4$). In such conditions, no pressure variations can be transmitted upstream of the *vena contracta* as the propagation velocity of such pressure variations is exactly the speed of sound. Hence, the mass flow rate can only be increased through either an enlargement of the *vena contracta* or an increase in the

upstream pressure p_1 .

It was stated above (2.1.3) that for sharp-edged perforated plates, Γ_0 is dependent on the flow conditions. Such phenomenon is of particular relevance when discussing choking. In fact, an increase of Γ_0 is equivalent to an increase in the size of the *vena contracta* area. Therefore, for choking to occur, it is not only necessary that U_{vc} reaches the speed of sound but also that the expansion of the *vena contracta* is prevented. In thick plates ($t^* \geq 0.75/0.8$), flow reattachment within the perforation bore limits the expansion of the *vena contracta* and the maximum mass flow rate \dot{m}_{max} is reached for values of NPR close to the theoretically predicted one. In thin plates ($t^* \leq 0.2$), the increase of A_{vc} is not prevented and fully choked conditions are reached for values of NPR much higher than the theoretical limit.

2.1.5 Determination of *vena contracta* pressure

It is evident from the previous paragraphs that the knowledge of the pressure at the *vena contracta* $p_{vc,s}$ would provide enough information for a complete characterization of the flow through the perforated plate. In fact, its value is needed to compute the discharge coefficient in both incompressible and compressible flows as well as the jet Mach number in the case of compressible flows. However, the experimental determination of its value is not straightforward, as the position of the *vena contracta* is itself an unknown.

To overcome this issue, the perforated plate can be tested by removing any downstream piping and letting it discharge freely in the atmosphere [14, 18]. If the *vena contracta* occurs downstream of the constriction, then $p_{vc,s} = p_{amb}$. The disadvantage of such a procedure is that in case of flow reattachment within the perforation, the downstream back-pressure does not coincide anymore with the pressure at the *vena contracta*.

Another approach is possible by considering the only case for which the *vena contracta* pressure is known at the same time as the ‘recovered’ downstream one $p_{2,s}$, that is, at cavitation inception. Defining the ‘liquid pressure recovery factor’ F_L as [19]:

$$F_L = \sqrt{\frac{p_{1,s} - p_{2,s}}{p_{1,s} - p_{vc,s}}} \quad (2.18)$$

and making the hypothesis that F_L remains constant up to cavitation inception, its value can be used to retrieve $p_{vc,s}$ once $p_{1,s}$ and $p_{2,s}$ are known. The standard IEC-60534-2-3 [19] suggests a test procedure for its computation in water. In particular, it provides a formula for F_L based on the maximum

flow rate Q_{max} attainable on the experimental plant if the upstream pressure $p_{1,s}$ is kept constant and the flow rate is increased by gradual opening of a downstream valve (and hence a decrease of $p_{2,s}$):

$$F_L = \frac{Q_{max}}{0.865 \cdot C_V} \sqrt{\frac{1}{p_{1,s} - 0.96 \cdot p_{vap}}} \quad (2.19)$$

where Q_{max} is expressed in [m³/h], the pressures are in [bar] and C_V is the average dimensional ‘flow coefficient’ defined, in water and in non-cavitating conditions, as:

$$C_V = \frac{Q}{0.865} \sqrt{\frac{1}{\Delta p_R}} \quad \left[\frac{\text{gpm}}{\text{psi}^{0.5}} \right] \quad (2.20)$$

with Q in [m³/h] and Δp_R in [bar]. It is worth noticing that the definitions of C_V and K_L are related through the formula:

$$K_L = \frac{A^2}{\frac{1}{2} \rho_1 C_V^2} \times 1.7321 \cdot 10^{12} \quad (2.21)$$

with ρ_1 in [kg/m³] and A in [m²]. A constant K_L hence means a constant C_V .

2.2 Aerodynamic generation of sound

2.2.1 Free turbulent flows

The theory of aerodynamic generation of sound is based on the pivotal work by Lighthill [5, 6]. Starting from the equations of motion for real viscous fluids (i.e. the Navier-Stokes equations), he was able to derive an inhomogeneous wave equation for the pressure fluctuations p' (both turbulent and acoustic) for an unconfined free turbulent flow. In tensor notation:

$$\frac{1}{c^2} \frac{\partial^2 p'}{\partial t^2} - \frac{\partial^2 p'}{\partial x_i^2} = \frac{\partial^2 T_{ij}}{\partial x_i \partial x_j} \quad (2.22)$$

where T_{ij} is Lighthill’s stress tensor, defined as:

$$T_{ij} = \rho u'_i u'_j + p' \delta_{ij} - \tau_{ij} - c^2 \rho' \delta_{ij} \quad (2.23)$$

with $\rho u'_i u'_j$ the fluctuating Reynolds’ stress, and τ_{ij} the fluctuating viscous shear stress. Generally, viscous shear stresses τ_{ij} are negligible when compared to the fluctuating Reynolds’ ones. Also, provided that pressure fluctuations are small enough and heat exchanges can be neglected (adiabatic flow) $p' \delta_{ij} = c^2 \rho' \delta_{ij}$. Hence, in unconfined high-Reynolds number turbulent flows $T_{ij} \approx \rho u'_i u'_j$, i.e. the aerodynamic sound is mainly produced by

the turbulent velocity fluctuations. The solution for the (acoustic) pressure fluctuation outside of a source volume V to (2.22) is of the form [5]:

$$p'_a(\vec{x}, t) = \frac{\partial^2}{\partial x_i \partial x_j} \int_V \frac{T_{ij} \left(\vec{y}, t - \frac{|\vec{x} - \vec{y}|}{c} \right)}{4\pi |\vec{x} - \vec{y}|} d^3 \vec{y} \quad (2.24)$$

This result is also known as the ‘Lighthill’s acoustic analogy’, since the form of the solution (a double divergence of a force per unit volume) is that corresponding to an acoustic quadrupole distribution over the volume V . The term ‘analogy’ referring to (2.24) is justified by the fact that it allows to compute the sound produced by a turbulent free flow as if that generated in an acoustic medium by a distribution of acoustic quadrupoles in a source region. The ‘only’ information needed is then the fluctuating flow field. Such consideration is the reason behind the widespread success of Lighthill’s acoustic analogy in jet flows, especially ever since advancements in Computational Fluid Dynamics (CFD) methods have allowed to obtain more precise fluctuating flow fields, e.g. [20]. Through dimensional considerations, it is also possible to show that, starting from (2.24), the acoustic power emitted by free turbulence in the far field scales as:

$$W_a^Q \propto \frac{\rho L_c^2}{c^5} \cdot U_c^8 \quad (2.25)$$

where the superscript Q refers to the quadrupole nature of the source and L_c and U_c are respectively a characteristic length and velocity of the flow (e.g., the nozzle diameter and the jet velocity for free jets). Expression (2.25) also goes by the name of ‘eighth-power law’ since it states that the acoustic power W_a emitted by an unconfined turbulent flow is proportional to the eighth power of a characteristic velocity, a fact which has been also widely experimentally verified [6]. It might be useful here to recall the definition of the sound power W_a of an acoustic source:

$$W_a = \int_S \vec{I} \cdot d\vec{S} \quad (2.26)$$

where S is the surface enclosing the source and \vec{I} the mean intensity vector, i.e. the average flow of power per unit normal area:

$$\vec{I} = \frac{1}{T} \int_0^T p'_a \vec{u}_a dt \quad (2.27)$$

with \vec{u}_a the acoustic velocity vector [7].

2.2.2 Presence of solid surfaces

The presence of solid boundaries greatly affects sound generation by fluid flows. Introducing a fluid-solid interface in fact causes an exchange of forces

between the flow and the solid due to both the average and fluctuating pressures within the flow field. In the case of a rigid surface (i.e., no vibrations are allowed), Curle [21] derived a second acoustic analogy, starting from that of Lighthill's. The solution in terms of pressure fluctuations can be written as:

$$p'(\vec{x}, t) = \frac{\partial^2}{\partial x_i \partial x_j} \int_V \frac{T_{ij} \left(\vec{y}, t - \frac{|\vec{x} - \vec{y}|}{c} \right)}{4\pi |\vec{x} - \vec{y}|} d^3 \vec{y} - \frac{\partial}{\partial x_i} \int_S \frac{f_i \left(\vec{y}, t - \frac{|\vec{x} - \vec{y}|}{c} \right)}{4\pi |\vec{x} - \vec{y}|} dS(\vec{y}) \quad (2.28)$$

where the first term is the free turbulence component of (2.24) and the second is the additional contribution due to the presence of the fixed surface. In particular, f_i is the fluctuating force per unit area acting on the fluid at the solid-fluid interface. It is composed of both the turbulent pressure fluctuations of the impacting fluid and of the acoustic pressure fluctuations generated by the quadrupole distribution in the source volume being reflected off the fixed surface. The term acoustic ‘analogy’ is again justified by the fact that the additional surface integral of (2.28) is the same form of solution expected by a distribution of acoustic dipoles along a surface S of strength f_i [8]. Through dimensional considerations, it is again possible to obtain a proportionality of the type in (2.25) between the generated acoustic power in the far-field and the characteristic quantities of the flow:

$$W_a^D \propto \frac{\rho L_c^3}{c^3} \cdot U_c^6 \quad (2.29)$$

where the superscript D refers to the dipole nature of the source. It is interesting to compare the relative efficiency of the two mechanisms of aerodynamic sound generation, i.e. free turbulence (2.25) and surface pressure fluctuations (2.29) by taking their ratio:

$$\frac{W_a^Q}{W_a^D} \propto \left(\frac{U_c}{c} \right)^2 \quad (2.30)$$

where $U_c/c = M$ is the Mach number based on the characteristic velocity U_c . It can then be seen that the free turbulence contribution to aerodynamic sound generation is ever more negligible with respect to the dipolar source the lower the Mach number is. In particular, for incompressible flows ($M \ll 1$, i.e. low Mach number or ‘incompressible’ flows), noise generation can be considered essentially dipolar in nature whenever a solid obstacle is present. This leads to useful approximations which will be more thoroughly dealt with in Chapter 3.

2.2.3 Whistling

While the work in this thesis is focused on noise generation from turbulence, this is however not the only way in which sound can be generated aerodynamically. A well-known mechanism is in fact related to the presence of self-sustained oscillations, whereby small fluctuations within the flow can be amplified without any external intervention [22]. The flow fluctuations can occur independently of turbulence and a classical example is the so called Kelvin-Helmholtz instability, responsible for the break-down of a jet into vortical structures due to the presence of a shear layer with the surrounding fluid [23]. Such flow fluctuations however translate in self-sustained oscillations whenever a feedback loop with the main flow is established [24]. A loop can be due for example to a solid obstacle causing a reflection of the flow instabilities so that a phased superposition with the incoming fluctuations occurs and the fluctuations increase in amplitude at the end of every cycle [25].

From this qualitative description of self-sustained oscillations it can be inferred how any sound produced by such type of mechanism is bound to be limited to specific frequencies for which the feedback loop actually occurs. In fact, noise from self-sustained oscillations is typically tonal in nature and is usually referred to as ‘whistling’. A noise source partly showing this behavior is discussed in Chapter 5.

2.3 Sound propagation in ducts

2.3.1 Modal decomposition

Sound propagation satisfies the homogeneous wave equation for the acoustic pressure fluctuations p'_a [26]:

$$\frac{1}{c^2} \frac{\partial^2 p'_a}{\partial t^2} - \frac{\partial^2 p'_a}{\partial x_i^2} = 0 \quad (2.31)$$

provided that suitable boundary conditions are set (e.g. zero-flux at solid walls, anechoic terminations...).

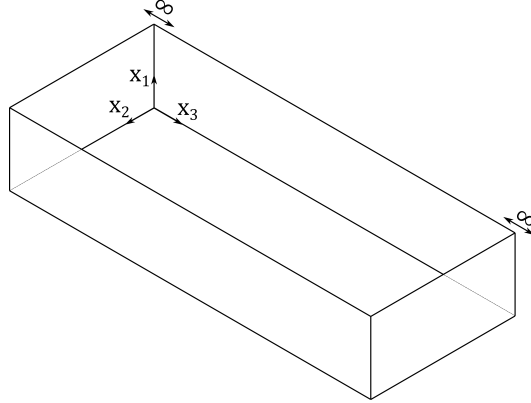


Figure 2.7: Infinite duct of rectangular cross-section with reference system.

For rigid ducts of constant cross-section (e.g. Figure 2.7), infinite length and harmonically varying acoustic pressure fluctuations in time, the most general solution for the acoustic pressure in the positive axial x_3 direction satisfying (2.31) can be written in complex notation as [24]:

$$p'_a(\vec{x}, t) = \sum_{m,n} C_{mn} \psi_{mn}(x_1, x_2) e^{-i(\omega t - k_{mn} x_3)} \quad (2.32)$$

where ψ_{mn} are normalized characteristic or ‘shape’ functions describing the acoustic pressure distribution along the duct’s cross-section of the mode (m, n) , C_{mn} is the amplitude of such mode, $\omega = 2\pi f$ is the angular frequency, $k_{mn} = \omega/c_{mn}$ the axial modal wave number and c_{mn} the propagational speed of the mode (m, n) . Sound hence travels inside a duct as a summation of different waves, with specific distributions of the acoustic pressure within the cross-section given by $\psi_{mn}(x_1, x_2)$ and with an axial distribution specified by the wavenumber k_{mn} along the axial direction x_3 . A property of the shape functions ψ_{mn} is their orthogonality:

$$\frac{1}{A} \iint_A \psi_{\mu\nu} \psi_{mn} dA = \begin{cases} 0, & \text{if } \mu, \nu \neq m, n \\ 1, & \text{if } \mu, \nu = m, n \end{cases} \quad (2.33)$$

Such property is fundamental if the average acoustic power W_a is to be computed from (2.32), as any cross-product between the modes will cancel out and W_a will be given by the summation of the power carried by each (propagating) mode [8].

2.3.2 Modal shape functions

The reason for the nomenclature (m, n) is clearer once the form of the characteristic functions is provided for the two cross sections considered in this thesis, i.e. rectangular and circular ducts.

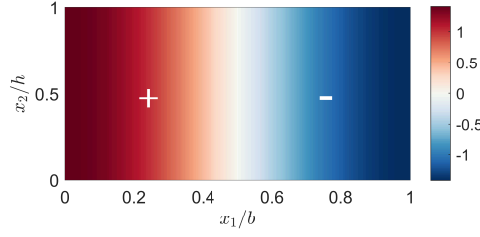


Figure 2.8: Colour plot of the characteristic function ψ_{10} for a rectangular duct with an aspect ratio $b/h = 2$. The vertical nodal line is visible as white at the center while the sign of the acoustic pressure fluctuation p'_a is indicated at the center of each half of the section.

For rectangular ducts of width b and height h , the modal shape function ψ_{mn} is given by [26]:

$$\psi_{mn}(x_1, x_2) = N_{mn} \cos\left(\frac{m\pi x_1}{b}\right) \cos\left(\frac{n\pi x_2}{h}\right) \quad (2.34)$$

where N_{mn} is a normalizing factor equal to 1 for the mode $(0, 0)$, $\sqrt{2}$ for the modes $(m, 0)$ and $(0, n)$ and 2 for the modes (m, n) with m, n positive integers. The mode (m, n) presents therefore a ‘checkerboard’ distribution with m vertical and n horizontal nodal lines and opposite signs of the pressure fluctuation p'_a across such lines.

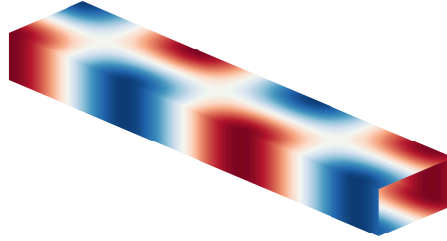


Figure 2.9: Colour plot of the distribution of mode $(1, 0)$ along the wall of a rectangular duct.

For circular pipes of internal radius R instead, the shape functions ψ_{mn} in cylindrical coordinates are given by [7]:

$$\psi_{mn}(r, \theta) = N_{mn} J_m(k_{r_{mn}} r) e^{im\theta} \quad (2.35)$$

where $N_{mn} = 1/J_m(k_{r_{mn}} R)$ is again a normalization constant, J_m is the m -th order Bessel function of the first kind, $k_{r_{mn}}$ is the radial modal wave number and m is an integer value which can be either positive (clockwise rotation) or negative (anti-clockwise rotation). The solution in terms of the

pressure fluctuations p'_a within the duct for an harmonic wave travelling in the positive x_3 direction is hence:

$$p'_a(r, \theta, x_3, t) = \sum_{m=-\infty}^{+\infty} \sum_{n=0}^{+\infty} C_{mn} \psi_{mn}(r, \theta) e^{-i(\omega t - k_{mn} x_3)} \quad (2.36)$$

The value of $k_{r_{mn}}$ is determined by imposing that the first derivative $J'_m(k_{r_{mn}} R) = 0$ to satisfy the rigid walls condition. Its values are usually reported in tabular form as $\chi_{mn} = k_{r_{mn}} R$, see Table 2.1.

m	n	χ_{mn}
0	0	0
1	0	1.8412
2	0	3.0542
0	1	3.8317
3	0	4.2012
4	0	5.3175
1	1	5.3314

Table 2.1: Solutions to $J'_m(\chi_{mn}) = 0$ for the first 7 modes.

Expression (2.35) hence describes an acoustic pressure distribution with m azimuthal and n radial nodal lines, e.g. Figure 2.10 for the first cut-on mode (1,0).

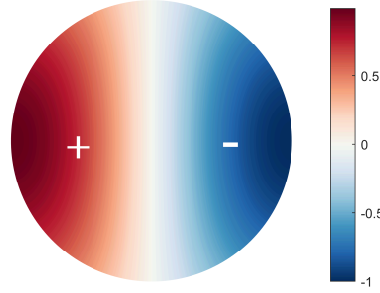


Figure 2.10: Colour plot of the characteristic function ψ_{10} for a circular pipe. The vertical nodal line is highlighted in white at the center while the sign of the acoustic pressure fluctuation p'_a is indicated at the center of each half of the section.

Substituting (2.35) in (2.36) and expressing $\text{Re}\{e^{i(m\theta + k_{mn}x_3)}\} = \cos(m\theta + k_{mn}x_3)$, it is easy to see that a mode with m at a fixed time instant t will have a constant phase along a spiralling surface [27]:

$$m\theta + k_{mn}x_3 = \text{const.} \quad (2.37)$$

If on the other hand the axial coordinate x_3 is fixed, then always from (2.32) it is easy to see that the nodal line rotates with angular frequency ω . This is the reason why such modes are usually indicated as ‘spinning’ modes (Figure 2.11).

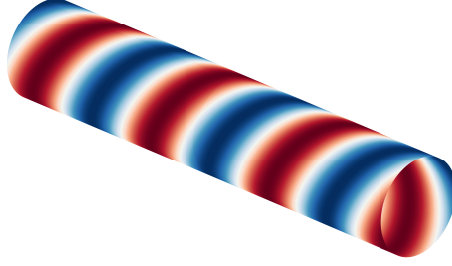


Figure 2.11: Colour plot of the distribution of ‘spinning’ mode $(1,0)$ at the wall of a pipe.

The mode $(0,0)$ is known as the ‘plane wave’ mode and it corresponds to the one-dimensional acoustic wave displaying a constant pressure distribution along the cross-section. The modes with $(m \neq 0, n > 0)$ are instead the ‘higher order’ acoustic modes of a given sound field.

2.3.3 Cut-off modes

Not all modes propagate at all frequencies. From (2.32), it can be seen that if the axial wavenumber k_{mn} is a complex value, the mode (m,n) tends to zero exponentially along x_3 . For wave sustainability, in fact, the following condition must be met [26]:

$$k^2 = \frac{\omega^2}{c^2} = \sum_j k_j^2 \quad (2.38)$$

where k is the total wave number and k_j is the wave number along the j -th direction. In rectangular ducts, the axial wave number k_{mn} is hence given by:

$$k_{mn} = \sqrt{\left(\frac{\omega}{c}\right)^2 - \left(\frac{m\pi}{h}\right)^2 - \left(\frac{n\pi}{b}\right)^2} \quad (2.39)$$

For k_{mn} to be real, the term under squared root must ≥ 0 . This is true for frequencies f such that:

$$f \geq f_{mn} = \frac{c}{2} \sqrt{\left(\frac{m}{h}\right)^2 + \left(\frac{n}{b}\right)^2} \quad (2.40)$$

where f_{mn} is also known as the *cut-off* frequency of mode (m, n) . In circular ducts, the axial modal wave number becomes:

$$k_{mn} = \sqrt{\left(\frac{\omega}{c}\right)^2 - k_{r_{mn}}^2} \quad (2.41)$$

from which, a mode is propagational if:

$$f \geq f_{mn} = c \frac{\chi_{mn}}{\pi D} \quad (2.42)$$

It is easy to verify that if $m = n = 0$ then the mode is propagational at all frequencies. This is valid in general for all ducts with a constant cross-section and it indicates that plane waves will always propagate with a constant propagational speed c . Expression (2.38) also indicates that the higher-order modes are dispersive, i.e. their propagational speed in the axial direction is dependent on the frequency. This is most readily seen by plotting the relationship $k_{mn} = f(\omega)$ for circular pipes (2.41) as an example, see Figure 2.12. It can be here seen that the relationship is linear for the plane wave and nonlinear for the other modes. A nonlinear variation of the axial wavenumber with frequency indicates that the wavelength is not linearly dependent on the frequency, as is instead the case for a constant propagational speed.

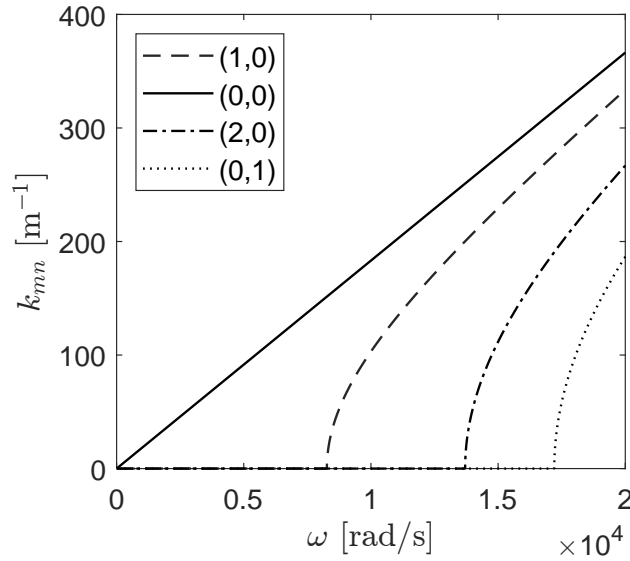


Figure 2.12: Dispersion curve for the first four propagating modes in a pipe of 1 inch diameter.

2.3.4 Influence of uniform flow

The presence of a uniform flow in the duct modifies the frequency ranges for which the higher-order modes are propagational. In fact, due to the Doppler

effect, the cut-on frequencies are shifted by a factor dependent on the flow Mach number M :

$$f'_{mn} = f_{mn} \sqrt{1 - M^2} \quad (2.43)$$

where $M = U/c$ with U the average flow velocity in the duct. It is then evident that for average duct speeds such that $M \ll 1$, the frequency shift can be neglected.

2.3.5 General solution for acoustic source distribution in a duct

For an infinite-length duct (i.e. anechoic terminations) of constant cross section of area A containing an ideal gas at rest except for acoustic disturbances, Doak [8] derived the following expression for the Fourier transform of the acoustic pressure downstream of a generic acoustic source distribution :

$$\hat{p}_a(x_1, x_2, x_3) = \sum_m \sum_n \frac{1}{2A} \rho_0 \hat{c}_{mn} \psi_{mn}(x_1, x_2) e^{-i\hat{k}_{mn}x_3} \hat{Q}_{mn} \quad (2.44)$$

where all quantities dependent on frequency have been reported as $\hat{\cdot}$, ρ_0 is the density of the fluid at rest and \hat{Q}_{mn} is the ‘effective source strength coefficient’. This last quantity takes into account the type of acoustic source (i.e. monopole, dipole, quadrupole) and its distribution over the source region, as will be better discussed in Chapter 3. Due to the orthogonality of the modes (2.33), the spectral density of the acoustic power \hat{W}_a corresponding to the pressure fluctuations in (2.44) is given by the summation of the power carried by each mode in the duct and it has the form:

$$\hat{W}_a = \sum_m \sum_n \hat{W}_a^{(m,n)} = \sum_m \sum_n \frac{\rho_0 \hat{c}_{mn}}{4A} \hat{S}_{mn} \quad (2.45)$$

with \hat{S}_{mn} the power spectral density (PSD) of \hat{Q}_{mn} :

$$\hat{S}_{mn} = \lim_{T \rightarrow \infty} \frac{\pi}{T} |\hat{Q}_{mn}|^2 \quad (2.46)$$

2.4 Coincidence in circular pipes

In the case of steel thin pipes (i.e., so that the ratio of the wall thickness t_{pipe} to the internal diameter D_i is less than 0.1) flanged at both ends, noise is most efficiently radiated from an internal acoustic pressure field to the outside environment by the flexural vibrations of the pipe [7]. The radial displacement w_{pq} (positive if outward) of a given structural vibrational mode

(p, q) for a simply supported thin pipe of length L is in fact proportional to [28]:

$$w_{pq}(x_3, r, \theta) \propto \sin\left(\frac{p\pi x_3}{L}\right) \cos(q\theta) \quad (2.47)$$

Such displacement is hence made up of an axial component along x_3 and a circumferential component along θ . Due to wave continuity, there is a discrete number of wavelengths λ_s along one circumference, see Figure 2.13 while due to the finite length of the pipe, standing waves occur along the axial direction and the axial wave number $k_{x_3} = 2\pi/\lambda_{x_3}$ is finite too.

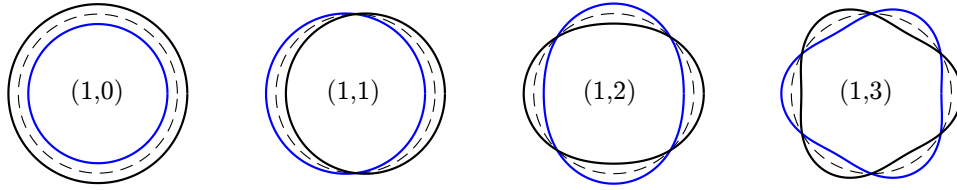


Figure 2.13: Vibrational modal shapes of a pipe. Original pipe section in dotted gray, displacements at two time instants in black and blue. The indices indicate the mode (p, q) as defined in (2.47).

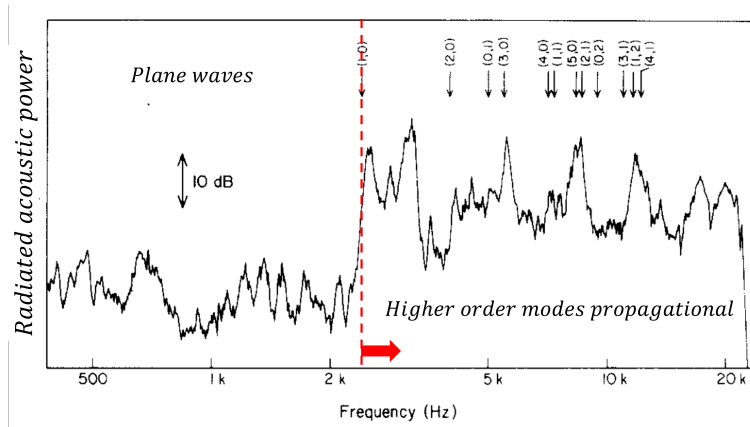


Figure 2.14: Acoustic power radiation from a thin walled pipe section downstream of a 90° mitred bend. Cut-on frequencies are also highlighted. Adapted from Bull & Norton [29].

The particular shape of the vibrational modes of the pipe makes the higher order acoustic modes inside the pipe the greatest contributors to pipe flow noise transmission to the outside environment [29]. This is due to the fact that the forcing inner pressure field at the pipe's wall closely matches the pipe's own vibrational modes, both spatially and in frequency. Such a condition is known as 'coincidence' [7]. Actually, while complete matching is

always true in a cross section, the same is not exactly so axially due to the fact that an acoustic wave is a traveling wave while the structural one is a standing wave (having supposed non-anechoic terminations). For steel pipes however, complete coincidence is usually present in the vicinity of the acoustic cut-on frequencies, when the higher order modes become standing waves (i.e. the system is in a resonant state). This coincidence (either complete or partial) is responsible for a steep increase of the pipe walls' vibrations and consequently for sound radiation (Figure 2.14).

Constriction noise in ducts: available theory and developments

The present chapter presents the available theory on the subject of broadband noise generation from ducted constrictions subject to gas flows. The discussion is limited to the flow ranges investigated in the following of the thesis, i.e. incompressible and subsonic flows, omitting any reference to shock-generated sound or whistling. First, the theory on sound generation in incompressible ducted flows is presented within the context of the dipole noise source acoustic analogy. Particular reference is made to the so-called ‘generalized spectrum’ models developed for constrictions that are perpendicular to the flow direction. Then, the case of subsonic flows is treated. An in-depth literature review on the subject is presented and a few theoretical considerations are made. Noise reduction strategies from the available literature/models are then drawn.

3.1 Incompressible flows

The case of incompressible flows (for which $Ma < 0.1$ globally) has received the greatest amount of attention by researchers dealing with the subject of broadband constriction noise in ducts. This is because of the possible simplifications to the basic theoretical models. In fact in such flows, compressibility can be neglected and the fluctuating Reynolds stresses in Lighthill’s stress tensor T_{ij} (2.23) are much smaller than the contribution of fluctuating forces exchanged with the obstacle and noise generation is predominantly dipolar in nature. In such a case, the ‘effective source strength coefficient’ defined in 2.3.5, takes the form [8]:

$$\hat{Q}_{mn} = -\frac{1}{i\omega} \iiint_V \frac{\partial \hat{f}_i(x'_i)}{\partial x_i} \psi_{mn}(x'_1, x'_2) e^{i\hat{k}_{mn}x'_3} dV \quad (3.1)$$

where \hat{f}_i is the (spectral) force field per unit mass of fluid acting over a finite volume V in the i -th direction within the duct (the prime $'$ symbol denotes the points within such volume V).

3.1.1 Obstacles perpendicular to the flow

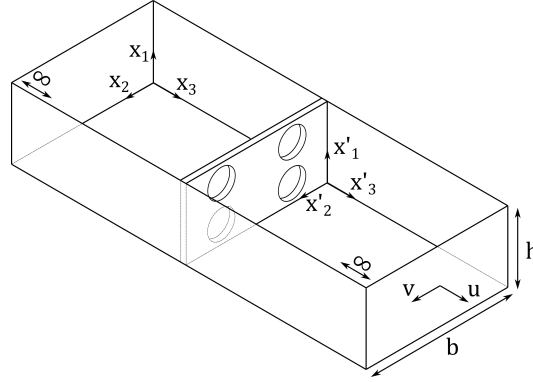


Figure 3.1: Obstacle perpendicular to the flow in an infinite-length rectangular duct, relative coordinate systems and planar velocity components.

While providing a strong starting point for theoretical considerations, (3.1) is still formidably difficult to apply. In their pivotal work on the subject, Nelson & Morfey [30] made the additional hypothesis that the fluctuating force field f_i in (3.1) acts along the axial x_3 direction only. Such an assumption is reasonable in the case of flow control devices, where a blockage of the flow section is effectively a barrier perpendicular to the flow. That is particularly true in the case of flow spoilers and perforated plates, the first being the subject of their investigation and the second of the present thesis (Figure 3.1). In fact, due to the limited extent of the body in the axial direction, the drag force dominates on the lift. In this case, Nelson & Morfey [30] have shown that the ‘effective source strength’ coefficient has the expression:

$$\hat{Q}_{mn} = \frac{1}{\hat{c}_{mn}} \iint_{A_s} \hat{f}_3(x'_1, x'_2) \psi_{mn}(x'_1, x'_2) e^{i\hat{k}_{mn}x_3} dA \quad (3.2)$$

where A_s is the area occupied by the perpendicular solid surface and f_3 is the difference between the fluctuating force per unit mass of fluid and per unit area acting perpendicularly to both sides of the obstacle’s surface. The authors also argued that for ducts of rectangular cross-section, the force fluctuations f_3 acting on the plate are correlated over a distance l_c (also known as correlation length) which is much smaller than the acoustic wavelength and smaller than the distance between the maxima/minima of the chessboard acoustic pressure pattern (see 2.3.2). In such a case, they

derived an expression for \hat{S}_{mn} (2.46) in terms of the cross power spectral density (CPSD) \hat{S}_{ff} of the fluctuating forces between two points (x'_1, x'_2) and (y'_1, y'_2) on the surface of the obstacle:

$$\hat{S}_{mn} = \frac{1}{|\hat{c}_{mn}|^2} \iint_{A_s} |\psi_{mn}(x'_1, x'_2)|^2 \times \\ \times \left\{ \iint_{A_s} \hat{S}_{ff}(x'_1, x'_2, y'_1, y'_2) dA(y'_1, y'_2) \right\} dA(x'_1, x'_2) \quad (3.3)$$

where:

$$\hat{S}_{ff}(x'_1, x'_2, y'_1, y'_2) = \lim_{T \rightarrow +\infty} \left(\frac{\pi}{T} \right) \hat{f}_3(x'_1, x'_2) \cdot \hat{f}_3^*(y'_1, y'_2) \quad (3.4)$$

Expression (3.3) is still in a form far from easy to apply. In fact, it shows a dependence on the CPSD of the fluctuating force distribution on the two sides of the obstacle (a quantity extremely difficult to obtain) and a coupled integration with the shape functions of the duct. As the ultimate engineering quantity to predict is the spectral acoustic power \hat{W}_a emitted by the flow through the obstacle and such quantity is dependent on \hat{S}_{mn} through (2.45), Nelson & Morfey [30] tried to simplify it by making two further assumptions:

- the inner integral in (3.3) is independent of the position (x'_1, x'_2) on the plate;
- the CPSD of the fluctuating force distribution over the surface of the plate is proportional to the total perpendicular fluctuating force F'_3 over the plate.

The first assumption is true if either the fluctuating force f_3 has a uniform PSD distribution over the surface of the plate and is correlated over a large distance or if the product of \hat{S}_{ff} and the area over which it is significantly correlated in is uniform over the cross section. In this case, (2.46) can be simplified by separating the two integrals:

$$\hat{S}_{mn} = \frac{1}{|\hat{c}_{mn}|^2} \left[\iint_{A_s} |\psi_{mn}(x'_1, x'_2)|^2 dA(x'_1, x'_2) \right] \times \\ \times \left[\iint_{A_s} \hat{S}_{ff}(x'_1, x'_2, y'_1, y'_2) dA(y'_1, y'_2) \right] \quad (3.5)$$

The second hypothesis states that, if the first is valid:

$$\hat{S}_F \approx \rho_0^2 A_s \iint_{A_s} \hat{S}_{ff}(x'_1, x'_2, y'_1, y'_2) dA(y'_1, y'_2) \quad (3.6)$$

where \hat{S}_{F_3} is the PSD of the total fluctuating force acting on the plate. Furthermore, Nelson & Morfey [30] observed that the first integral in (3.5) has a ‘most probable value’ of unity over the cross-section. Therefore, the original expression (3.3) becomes:

$$\hat{S}_{mn} = \frac{\hat{S}_{F_3}}{\rho_0^2 |\hat{c}_{mn}|^2} \quad (3.7)$$

and substitution in (2.45) yields the following expression for the PSD of the acoustic power:

$$\hat{W}_a = \sum_m \sum_n \frac{1}{\hat{c}_{mn}} \frac{\hat{S}_{F_3}}{4A\rho_0} \quad (3.8)$$

The modal contributions to \hat{W}_a are therefore only linked to the double summation in m and n of the modal speeds \hat{c}_{mn} . Their expression is dependent on the modal shape functions ψ_{mn} through the total wave number relationship provided in (2.38). For plane waves ($m = 0, n = 0$), the expression is the same independently of the duct cross-section and is:

$$\hat{W}_{a,\Delta f} = \frac{\hat{S}_{F_3}}{4A\rho_0 c} \quad \text{if } f_c < f_{c.o}^I \quad (3.9)$$

where Δf is the frequency bandwidth around the center frequency f_c and $f_{c.o}^I$ is the first cut-on frequency of the first higher order mode. Above such threshold, the propagation is multi-modal and the expression of $\hat{W}_{a,\Delta f}$ depends on the shape of the duct. For rectangular cross-sections of height h and width b [30]:

$$\hat{W}_{a,\Delta f} = \frac{k^2 [1 + (3\pi/4k)(h+b)/A]}{24\pi\rho_0 c} \hat{S}_{F_3} \quad \text{if } f_c > f_{c.o}^I \quad (3.10)$$

For circular cross-sections of radius R [31]:

$$\hat{W}_{a,\Delta f} = \frac{k^2 [1 + (3\pi/4Rk)]}{24\pi\rho_0 c} \hat{S}_{F_3} \quad \text{if } f_c > f_{c.o}^I \quad (3.11)$$

3.1.2 Generalized spectrum models

To be able to use (3.8), the frequency content of the total fluctuating force on the obstacle must be known. Experimental evidence by various authors ([32, 33]) points to the fact that such quantity is proportional to the steady state drag force acting on the plate through a ‘generalized spectrum’ dependent on the frequency. That is:

$$\hat{S}_{F_3} = K^2(\text{St}) \bar{F}_3^2 \quad (3.12)$$

where $K^2(\text{St})$ is the ‘generalized spectrum’, function of the Strouhal number $\text{St} = fL_c/U_c$ and \bar{F}_3 is the total average drag force acting on the plate. The term ‘generalized’ comes from the fact that a universal collapse may be present, at least for similar types of obstacles (e.g. spoilers of varying width, orifice plates) [34]. However, such universality is particularly hard to prove because of the many possible choices for both the characteristic length L_C and velocity U_C as well as for the definition of the average total drag force \bar{F}_3 . In the following, a short overview of the different approaches followed by some authors are provided.

Pressure drop scaling

In their original paper, Nelson & Morfey [30] reasoned that the total drag force is equal to the pressure loss Δp_R across the spoiler multiplied by the cross-sectional area of the duct. That is:

$$\bar{F}_3 = A\Delta p_R \quad (3.13)$$

They proceeded to non-dimensionalize the force through the drag coefficient C_D :

$$C_D = \frac{\bar{F}_3}{\frac{1}{2}\rho_0 U^2 A_s} \quad (3.14)$$

Such relationship can be re-written as a function of the average ‘constriction velocity’ $U_{\text{cnstr.}} = U/\phi$ (taken here as characteristic velocity U_C) and of the porosity ϕ of the spoiler, so that the average drag force \bar{F}_3 becomes:

$$\bar{F}_3 = \frac{1}{2}\rho_0 U_{\text{cnstr.}}^2 C_D \phi^2 (1 - \phi) A \quad (3.15)$$

Employing such average drag force into the definition of the power spectral density \hat{S}_{F_3} and substituting in the expressions provided in (3.9) and (3.10) for $\hat{W}_{a,\Delta f}$, it is possible to obtain, for rectangular ducts [30]:

$$\hat{W}_{a,\Delta f} = \begin{cases} \left(\frac{\rho_0}{16c_0}\right) AK^2(\text{St}) [\phi^2(1 - \phi)]^2 C_D^2 U_{\text{cnstr.}}^4, & \text{if } f_c < f_{c.o}^I \\ \left(\frac{\rho_0\pi}{24c^3}\right) \left[1 + \left(\frac{3\pi}{4k}\right) \left(\frac{h+b}{A}\right)\right] \times \left(\frac{A}{d}\right)^2 \text{St}^2 K^2(\text{St}) [\phi^2(1 - \phi)]^2 C_D^2 U_{\text{cnstr.}}^6, & \text{if } f_c > f_{c.o}^I \end{cases} \quad (3.16)$$

An important remark to be made on the structure of (3.16) is that the power law $\hat{W}_a \propto U_{\text{cnstr.}}^\alpha$ shows now a power exponent $\alpha = 4$ for the plane wave region and $\alpha = 6$ for the higher-order mode frequency range. The presence of the duct is hence responsible for a modification of the power law for the acoustic power emitted by an equivalent dipole source, which passes from

$\hat{W}_a \propto U^6$ in the free-field to a $\hat{W}_a \propto U^4$ in the ducted configuration.

The scaling in (3.16) showed a good collapse (Figure 3.2) for the spoilers tested in the original paper by Nelson & Morfey [30] if the spoiler width d was chosen as the characteristic length L_c in the definition of the Strouhal number St . However, later authors questioned the generality of choosing simply the device's porosity ϕ for computing the constriction velocity $U_{\text{cnstr.}}$. They also discussed of the problems in selecting a representative length L_C to be used in St for more complex devices. Regarding the computation of the constriction velocity, Oldham & Ukpoho [31] suggested an 'open area ratio' σ (such that $U_{\text{cnstr.}} = U/\sigma$) based on the pressure loss coefficient K_L defined in 2.1:

$$\sigma = \frac{\sqrt{K_L} - 1}{K_L - 1} \quad (3.17)$$

When dealing with circular orifice plates, Kårekull et al. [35] also proposed a definition of the 'open area ratio' $\sigma = \Gamma_0 \phi$ based on the *vena contracta ratio* Γ_0 defined in (2.8), so that $U_{\text{cnstr.}} = U_{vc}$. As for the characteristic quantity, the equivalent diameter of the constriction $D_{\text{cnstr.}}$ (defined as the diameter of the circle with the same cross-sectional area of the constriction $A_{\text{cnstr.}} = \sigma A$) can be employed so that St may be expressed as [35]:

$$St = \frac{f D_{\text{cnstr.}}}{U_{\text{cnstr.}}} = \frac{\sigma f_c \sqrt{4 A_{\text{cnstr.}}/\pi}}{U} = \frac{\sigma^{1.5} f_c \sqrt{4 A/\pi}}{U} \quad (3.18)$$

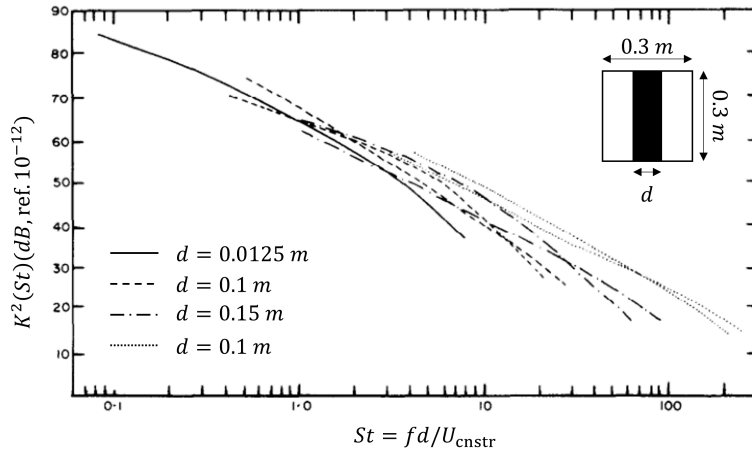


Figure 3.2: Generalized spectrum $K^2(St)$ for different spoiler widths and different constriction velocities, adapted from Nelson & Morfey [30].

Momentum flux scaling

Kårekull et al. [35] proposed an alternative model to the pressure drop scaling by stating that such model loses validity when the characteristic dimension of the constriction L_c is much less than that of the duct. They hence computed the force \bar{F}_3 by applying an integral momentum balance between a section immediately upstream of the constriction and the average velocity at the constriction. The force acting on the plate will in fact balance the momentum fluxes $M_i = \pm \dot{m} U_i$ between the two flow sections. Since the mass is conserved $\dot{m} = \rho_0 A U$, the force \bar{F}_3 can be written as:

$$\bar{F}_3 = \rho_0 U A U_{\text{cnstr.}} - \rho_0 A U^2 = \rho_0 U A (U_{\text{cnstr.}} - U) \quad (3.19)$$

If the velocity $U_{\text{cnstr.}} = U/\sigma \gg U$, the force \bar{F}_3 then takes the form:

$$\bar{F}_3 \approx \rho_0 A \frac{U^2}{\sigma} \quad (3.20)$$

They tested their scaling on a number of thin perforated plates with widely varying values of K_L (from 8 up to 35000) and found a best fit of the ‘generalized spectrum’, given by the equations:

$$10 \log_{10} \left(\frac{K^2}{10^{-12}} \right) = \begin{cases} 65 & \text{if } St < 1 \\ 65 - 28 \log_{10}(St) & \text{if } St \geq 1 \end{cases} \quad (3.21)$$

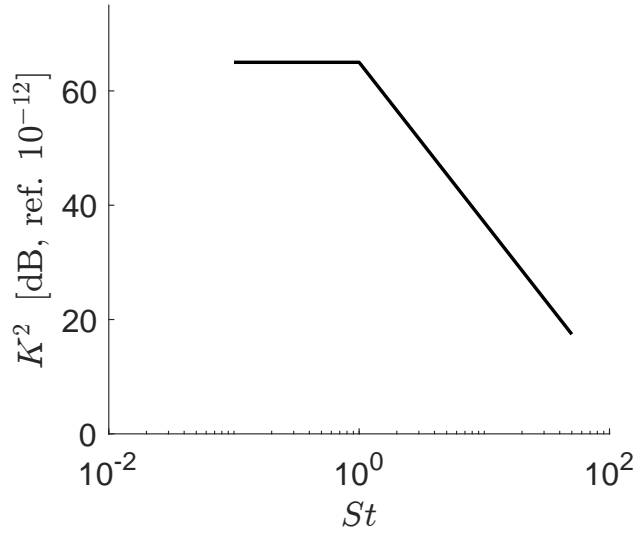


Figure 3.3: Best-fit generalized spectrum for orifice plates as suggested by Kårekull et al. [35]

3.1.3 Pressure fluctuations on the surface of an orifice plate

The discussion in 3.1.1 has highlighted the fact that for low Mach number flows ($M \leq 0.1$ globally), the knowledge of the pressure fluctuations p' acting on the surface of a constriction perpendicular to the flow is sufficient to predict the emitted aerodynamically-produced far-field acoustic power. To prove such findings and shed more light on some of the assumptions, Tao et al. [36, 37] performed an in-depth experimental analysis on the noise generation mechanisms of a thin orifice plate.

In particular, they measured the pressure fluctuations p' on selected points along the radius and the circumference of the plate, both on the upstream and the downstream face. They confirmed that the pressure fluctuations are correlated over a very small area, particularly so for increasing frequencies, as also semi-empirically suggested by Nelson & Morfey [30]. However, the distribution of such pressure fluctuations over the surface, which were mainly turbulent in nature, deviated considerably from the uniform (Figure 3.4).

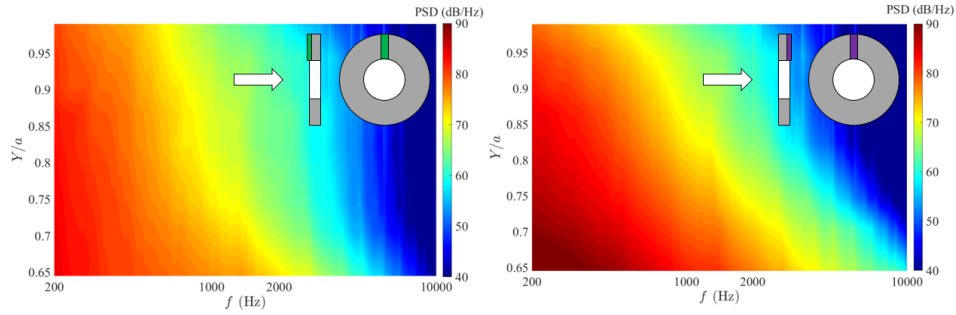


Figure 3.4: Power spectral density of the pressure fluctuations along the non-dimensional radius, adapted from Tao et al. [36]. Upstream side (left), downstream side (right). The position of the measurements are highlighted in green (upstream) and violet (downstream).

It is evident from such results that the pressure fluctuations in this case were concentrated within a small region just outside of the orifice. This may make the hypothesis behind the ‘generalized spectrum’ approach not true for certain cases. However, a more in-depth analysis of its consequences may lead to a potential noise reduction strategy, discussed in 3.3.1. Application of (3.3) knowing \hat{S}_{ff} allowed to predict the far-field acoustic power \hat{W}_a , which was in good agreement with the measured one except at low frequencies. This further confirms that a constriction subject to a perpendicular low Mach number flow acoustically behaves like a distributed dipole source.

3.2 Subsonic flows

For the case of ducted subsonic flows, theoretical investigations are more difficult due to the higher complexity in considering both the effects of the instantaneous Reynolds stresses $\rho_0 u'_i u'_j$, the fluctuating forces exchanged with the solid obstacles and their distribution in space and time. The research on the topic has therefore been more experimental and, recently, numerical, in nature. Some theoretical considerations can be drawn nonetheless if such case is seen as a superposition of the effects of two equivalent acoustic source distributions, i.e. dipoles (fluctuating forces on solid walls) and quadrupoles (fluctuating stresses distributed in finite regions of the flow). The former contribution was already dealt with in the previous section 3.1. In the following subsections, the effect of the additional quadrupole component in the source mechanism is first presented from a theoretical point of view. Then, some experimental results from the literature are summarized.

3.2.1 General solution for a ducted quadrupole distribution

A theoretical insight on the role of a quadrupole-like distributed source in ducted configurations can be found in the work on the solution of fundamental source configurations in ducts by Doak [8]. He provided a definition of the ‘effective source strength coefficient’ \hat{Q}_{mn} for the case of a stress distribution $\sigma_{ij}(x'_1, x'_2, x'_3)$ of harmonic time dependence $e^{i\omega t}$, applied over a finite region of volume V within the duct:

$$\hat{Q}_{mn} = -\frac{1}{i\omega\rho_0} \iiint_V \frac{\partial^2}{\partial x'_i \partial x'_j} \left[\sigma_{ij}(x'_1, x'_2, x'_3) \psi_{mn}(x'_1, x'_2) e^{-i\hat{k}_{mn}x'_3} \right] dV \quad (3.22)$$

where (x'_1, x'_2, x'_3) are points within the volume V . This expression shows that, as far as the acoustic pressure fluctuations p'_a are concerned, the distribution of such source again has an effect on the amplitude of the duct mode (m, n) through the integration of the term $\sigma_{ij}(x'_1, x'_2, x'_3) \psi_{mn}(x'_1, x'_2)$.

The problem in deriving a ‘usable’ solution from (3.22) is that in real flow problems, σ_{ij} must be known over all of the spatial and temporal domain. Furthermore, the random nature of turbulent fluctuations would also add to the problem the fact that the correlation between two given points in the source volume could be very different from the uniform one behind expression (3.22).

Sound power from ducted isotropic turbulence

An indication of the characteristics of the emitted sound power by a ducted subsonic turbulent flow was provided theoretically by Davies & Ffowes-Williams [38]. They considered the presence of a finite volume of fluid

within the duct subject to isotropic turbulence and, by making certain assumptions on its correlation, were able to show that the presence of a confinement deeply modifies the emissions of such a source. In particular, they arrived at the conclusion that the total acoustic power emitted by the flow has a different scaling law with respect to the average flow velocity U which is dependent both on the frequency and on the average flow Mach number. Indicating with:

- Q : the non-dimensional far-field acoustic power;
- β : the ratio between the characteristic frequency of the turbulent eddies and a reference frequency equal to the ratio U/b , with b a dimension of the channel;
- M : the average duct Mach number $M = U/c$ outside of the turbulent region.

They derived an expression of the non-dimensional acoustic power Q as a function of the product βM , reported graphically in Fig.3.5. If such value is sufficiently low, the acoustic power grows with the sixth power of the average velocity in the plane wave region and with the eighth power when many modes are propagational. This result shows that when the frequency is sufficiently low and the wavelength $\lambda = c/f$ is either much larger or comparable to the duct's dimensions and only plane waves are propagational, the quadrupole mechanism of sound generation is equivalent in terms of emitted power to a dipole in the free field. As shown in (2.29), such an aerodynamic source should have a dependence of $W_a \propto U^6$ on the average flow velocity. For higher frequencies instead, the quadrupole nature of the source as predicted by Lighthill in the free-field is again found with a 'classical' $W_a \propto U^8$ power law of the emitted acoustic power.

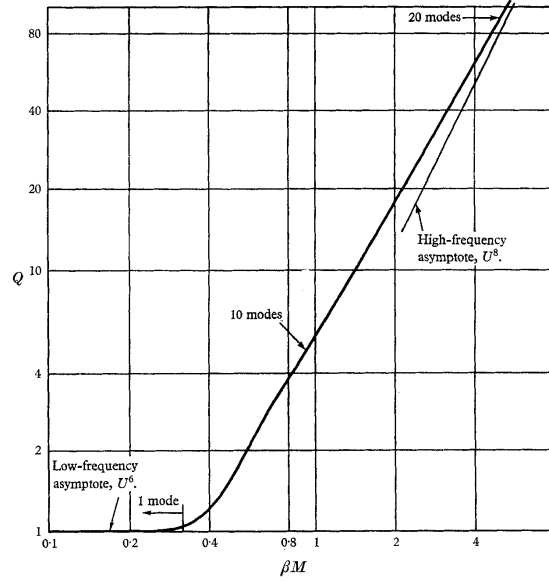


Figure 3.5: Proportionality between the non-dimensional far-field acoustic power Q downstream of a finite volume of isotropic turbulence in a rectangular duct and the product of a non-dimensional frequency β and the flow Mach number, from Davies & Ffowcs-Williams [38].

3.2.2 Experimental works

The first study dealing with noise generation by ducted orifice plates in the subsonic to sonic range is that of Jenvey [39]. He rewrote Lighthill's power law for W_a (2.25) in terms of the isentropic jet velocity U_j of (2.14), thus expressing W_a as a function of the NPR. He then proceeded to test this formulation on a series of orifice plates in a pipe discharging into the atmosphere, measuring the emitted acoustic power in a reverberant chamber outside of the pipe's exit. He found a good agreement with respect to the eighth-power law, suggesting that noise generation was dominated by turbulent mixing. However, Blake [25] contested this result by citing the fact that Jenvey's orifice plates had a too small porosity ($\phi_{\max} = 0.06$) for flow-surface impingement to be significant, therefore favoring the quadrupole-like source of turbulent mixing over the dipole-like one of force fluctuations.

A more fundamental analysis of noise generation mechanisms in ducted subsonic orifice plates and nozzles was carried out by Kerschen & Johnston [40]. They showed that noise generation occurs within the first pipe diameters downstream of the orifice, where the internal pressure fluctuations are dominated by the hydrodynamic component. Further downstream, the fluctuating pressure field is characterized by the presence of a base 'boundary layer noise' with superposed acoustic waves. By developing a technique

for the separation of the sound field inside the pipe in its higher-order modes, they were able to accurately compute the far-field emitted acoustic power. They found that such power was in accordance with the theoretical results found by Davies & Ffowcs-Williams [38] discussed in the previous section 3.2.1, i.e. it displayed the behavior of a quadrupole-like distributed source confined in a duct. Moreover, they also showed that the higher-order modes contributed either equally or more to the overall emitted sound power than the plane wave mode. This was the truer for the azimuthal modes $(m, 0)$. The authors suggested that this was linked to the presence of coherent structures (vortex rings) subject to circumferential instabilities which would be effective source mechanisms for higher-order noise generation. This explanation agrees in principle with the theoretical expression (3.22) by Doak [8], which stressed the importance of the source position on the higher-order modal composition.

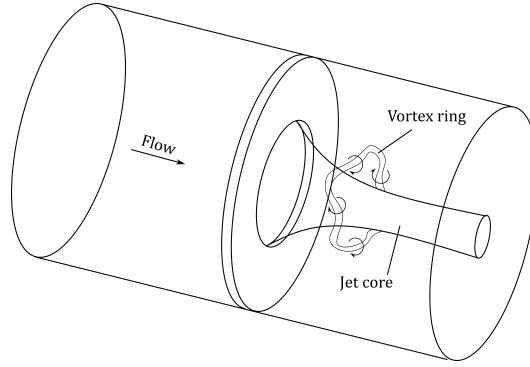


Figure 3.6: Possible visualization of circumferential instabilities of the vortex ring generated downstream of an orifice flow, as supposed by Kerschen & Johnston [40].

Another influential work on the subject was that of Agarwal [41]. He thoroughly studied the distribution of the wall pressure fluctuations along a circular pipe inside of which different orifice plates were installed, with flow ranging from the subsonic to choked conditions. The tested orifice plates were all thin and with sharp-edges, with diameter ratios β ranging from 0.6 to 0.8. Based on the amplitudes and the shapes of the measured wall pressure spectra, he subdivided the flow into five different regions based:

- zone 1 ($x_3/D \leq -0.8$): undisturbed fully developed turbulent pipe flow. The spectrum is a superposition of the undisturbed turbulent pipe spectrum and an acoustic one due to the noise generated at the orifice. Sharp peaks at the cut-off frequencies of the pipe are reported;
- zone 2 ($-0.8 < x_3/D \leq 0$): separation occurs upstream of the plate and small vortices appear;

- zone 3 ($0 \leq x_3/D \leq 1.4$): the flow is separated and after contracting to the *vena contracta* it gradually expands until reattachment. The spectrum is broad-band in character, typical of hydrodynamic turbulence though of much higher amplitude than the case of undisturbed flow.
- zone 4 ($1.4 \leq x_3/D \leq 48$): the hydrodynamic component of the pressure fluctuation is gradually dissipated and the wall pressure spectrum shows the presence of peaks at the cut-off frequencies of the pipe related to the presence of higher-order modes.
- zone 5 ($x_3/D \geq 48$): the flow has recovered its undisturbed configuration, but the wall pressure spectrum shows higher levels than in the case of the undisturbed flow due to the superposed acoustic field. The peaks at the cut-off frequencies are less evident.

Through the same modal separation technique developed by Kerschen & Johnston [40], he was also able to show that the amplitudes of the higher-order modes at cut-off showed a decrease along the pipe, as their energy was partly dissipated by viscosity and partly absorbed by the pipe wall vibrations.

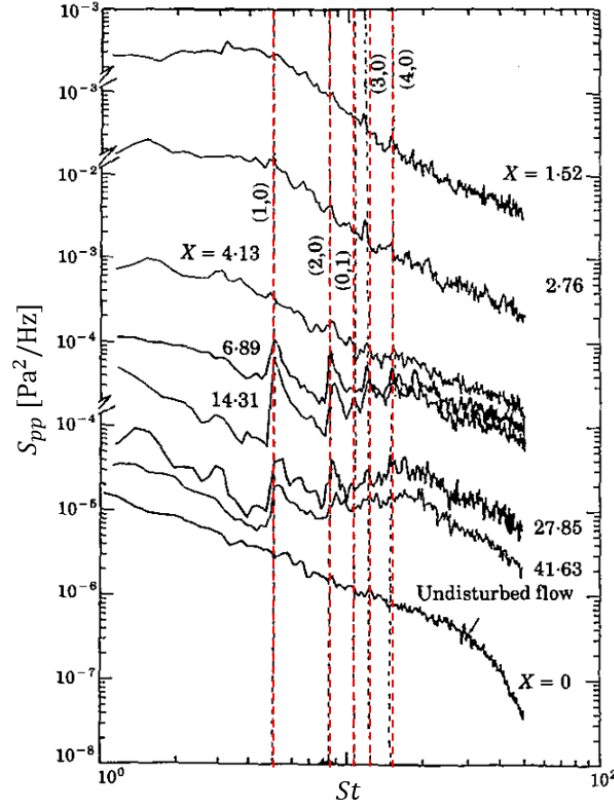


Figure 3.7: Power spectral density of fluctuating pressure at the wall at various non-dimensional distances $X = x_3/D_i$ downstream of an orifice subject to subsonic flow conditions, adapted from Agarwal [41].

A recent addition to the body of knowledge in the field of ducted perforated plate noise for subsonic flows is the work by Laffay et al. [42, 43]. A series of thin perforated plates with varying hole dimensions and arrangements were tested with and without a downstream pipe for flows ranging from the subsonic to the transonic. The acoustic sound pressure level (SPL) in the anechoic room where the orifice discharged was measured through a microphone array to also assess its spatial directivity. They found that the presence of the pipe changed the power law of the SPL for a frequency range comprising only the plane wave, which changes the dependence of the SPL from $\propto U_j^8$ to $\propto U_j^6$. This again may indicate that the dominant source remains the quadripolar one due to turbulent mixing, as shown in 3.2.1. Furthermore, through flow visualization techniques, Laffay linked the presence of strong tonal noise for low NPRs to the shedding of vortical structures of the type shown in Figure 3.6 [42].

3.3 Selective modal excitation

The previous review of the available literature indicates that the modal composition in terms of higher-order duct modes of the generated sound field by a localized disturbance may be dependent on the particular distribution of the source, independently of the actual source mechanism. The important contribution of the higher-order modes to the overall acoustic power transmitted in both directions of the disturbance has also been stressed, as well as their role in the transmission of sound, especially for circular pipes; see 2.4. A possible noise reduction strategy could then be envisaged by which a careful design of the geometry of the flow constriction limits the extent to which a given higher-order mode (m, n) is excited.

This idea of ‘selective modal excitation’ is at the basis of the experimental work of this thesis. While for the subsonic flow range the coexistence of the two mechanisms makes it particularly difficult to obtain further guidance from a theoretical point of view, the case of low Mach number flows with perpendicular obstacles permits some developments. Such developments are the subject of the following subsection 3.3.1.

3.3.1 Further developments for low Mach number flows

The experimental campaign of Tao et al. [36, 37] described in 3.1.3 has shown that, at least for thin orifice plates in pipes, the separation in (3.5) may not be justified, due to the non-homogeneous distribution of p' over the plate’s surface. Since however it was confirmed that p' is indeed correlated over a very small area, the following approximation could be valid for the CPSD of f_3 :

$$\iint_{A_s} \hat{S}_{ff}(x'_1, x'_2, y'_1, y'_2) dA(y'_1, y'_2) \approx \hat{S}_f(x'_1, x'_2) \hat{A}_c(x'_1, x'_2) \quad (3.23)$$

where $\hat{A}_c(x'_1, x'_2)$ is the coherence area, defined as the area centered in (x'_1, x'_2) over which the pressure fluctuations at two points have a correlation greater than 0.1 [37]. What has to be highlighted in (3.23) is that it is the PSD of the pressure fluctuations $\hat{S}_f(x'_1, x'_2)$ that is now considered, instead of the two-point CPSD $\hat{S}_{ff}(x'_1, x'_2, y'_1, y'_2)$. No studies on the spatial distribution of $\hat{A}_c(x'_1, x'_2)$ for similar types of flows are available in the literature. However, it is possible to employ an ‘average coherence area’ $\langle \hat{A}_c \rangle$ over the obstacle’s surface, supposing that this quantity does not deviate too much from it along the surface. In doing so, and substituting (3.23) in (3.3) the following expression is obtained:

$$\hat{S}_{mn} = \frac{\langle \hat{A}_c \rangle}{|\hat{c}_{mn}|^2} \iint_{A_s} |\psi_{mn}(x'_1, x'_2)|^2 \hat{S}_f(x'_1, x'_2) dA \quad (3.24)$$

This expression shows that a given mode (m, n) carries more energy the more \hat{S}_f follows the relative shape function's pattern over the duct's cross section.

Case of circular orifices

The fact that the position of a source within the cross-section of the duct influences differently the amplitudes of the higher order modes was already discussed by Doak [8]. However, the experiment of Tao et al. [36, 37] and the discussion above point to the possibility of influencing both the frequency content and the overall emitted acoustic power through a careful positioning of the perforations. As the distance from the edge of such perforations increases, a rapid decrease in the magnitude of p' is in fact observed. This means that the greatest contribution to the integrals in (2.45) will be given by the relatively small 'ring area' around the edge A_{ring} where $\hat{S}_f(x'_1, x'_2)$ is highest. Such observation well agrees with results for similar flows, where it is seen that the radial extension of the perturbed turbulence-producing region around the jet is very small in the vicinity of the orifice, at least downstream of it [44].

It could then be appropriate to assume that as far as the maximum contribution to (2.45) is concerned, any two jets issuing from two circular holes may be considered as independent from each other as long as their respective distance is not too small. Hence, generalizing to ducts of any (constant) cross-section and to plates with a number ν of circular holes, an easily obtainable indicator of the capacity of a given hole arrangement in exciting the (m, n) mode could be then provided by a 'modal efficiency coefficient' defined as:

$$\Psi_{mn} = \frac{1}{A} \sum_{\nu} \iint_{A_{\text{ring}, \nu}} |\psi_{mn}(x'_1, x'_2)|^2 dA \quad (3.25)$$

where A_{ring} will depend on the choice of the ring's width w . The rough approximate nature of expression (3.25) may be justified if such a coefficient is regarded as an easy-to-implement engineering tool for a qualitative design of orifice plates in low Mach number flows. Once a plate geometry in terms of number and dimensions of the orifices is chosen based on fluid-dynamic considerations (see 2.1.2), their disposition along the plates' surface could in fact be based on a minimisation of Ψ_{mn} for each propagating mode (m, n) within the frequency range of interest.

Noise generation in ducted low Mach number flows through perforated plates

This chapter presents the experimental work performed at the University of Technology of Compiègne (UTC), France, for the characterization of noise emissions by low Mach number flows through ducted perforated plates with circular orifices. The aim of the study was to test the hypothesis of ‘selective modal excitation’ discussed in 3.3 by measuring the modal contributions to the acoustic power spectral density \hat{W}_a produced by the plates within a range of frequencies where up to eight higher-order acoustic modes were propagational. The influence of the circular orifices’ number and arrangement was also investigated by means of a flow visualization technique (Particle Image Velocimetry, PIV) to gather a more complete overview of the phenomenon.

4.1 Experimental setup and measurement techniques

The experimental setup employed in this part of the work is located at the ‘Roberval Laboratory’ of the UTC and is a result of a collaboration between the same university and the automotive company ‘Valeo’. It was developed during the PhD. work of Dr. H. Trabelsi and a thorough description of it can be found for example in [45, 46]. The same experimental test bench has been used for a number of other publications [20, 47]. It allows (for low Mach number flows) the measurement of: fluid-dynamic quantities (mass flow rate and pressure drop caused by insertion of an obstacle), the emitted internal acoustic power \hat{W}_a of ducted obstacles and its modal composition in terms of the power spectral density (PSD) of the modes \hat{W}_a^{mn} through the 2N-port method (4.1.3) and the mean and rms-fluctuations of the velocity field over a selected region through a PIV setup (4.1.4).

4.1.1 General characteristics

A scheme of the test bench is provided in Figure 4.1. It consists of a duct of rectangular cross section of height equal to 100 mm and width equal to 200 mm for a total length of 4.1 m. Two anechoic terminations are connected to the extremities of the duct to avoid acoustic reflections starting from 100 Hz. The air flow is generated by a centrifugal fan, driven by a variable-speed electric motor connected to a frequency handle for a precise regulation of the flow rate. To partly eliminate the noise produced by the fan, flow silencers are placed between the fan and the rectangular duct. In addition, a stabilization tank is utilized to mitigate the velocity fluctuations of the airflow.

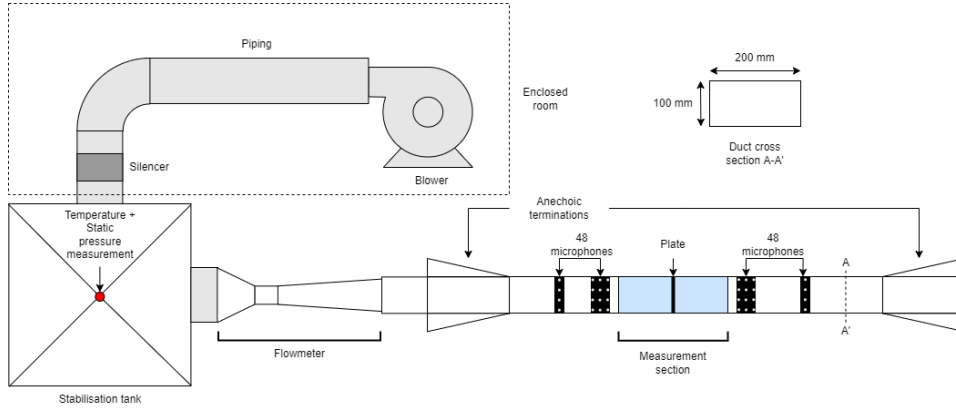


Figure 4.1: Schematic of the low Mach number aeroacoustic test bench at the Roberval Laboratory of the University of Technology of Compiègne (UTC).

The total pressure drop Δp_{tot} between the flow stabilization tank and the duct's outlet is measured through a differential pressure transducer (Testo 0638-1447) connected between the stabilization tank and the external environment. More specifically, one of the inputs of the transducer is connected through Y-junctions to three pressure taps at various positions along the stabilization tank so that the average pressure inside is correctly measured. The pressure drop caused solely by the obstacle Δp_R is measured as described in 4.2.1. The mass flow rate is obtained by means of an integrated Venturi-like flow meter combining readings of static temperature in the tank, static pressure just before the throat and the velocity in the throat through a Pt100 RTD probe, a pressure transducer (WIKA P-30), an hot-film anemometer (TSI 8455), respectively.

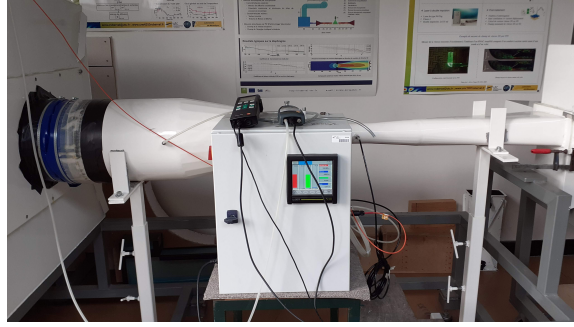


Figure 4.2: View of the Venturi-like flow meter upstream of the measurement section.

The middle section of the rectangular duct (measurement section) has four Plexiglas windows to grant optical access for the PIV measurements. Obstacles can be installed inside the measurement section through side screws. A set of 1/2 in. condenser microphones (GRAS 40AD) with pre-amplifier (GRAS 26CA) are installed in a flush configuration on both upstream and downstream sides of the measurement section for application of the 2N-port method (4.1.3). The signals issuing from the microphones are then sent to an analog-to-digital converter (Siemens LMS SCADAS III) and acquired by a PC through Siemens LMS TestLab software. Also, a compression driver (BMS 4591) can be installed at different locations distributed on both upstream and downstream sides of the measurement section.

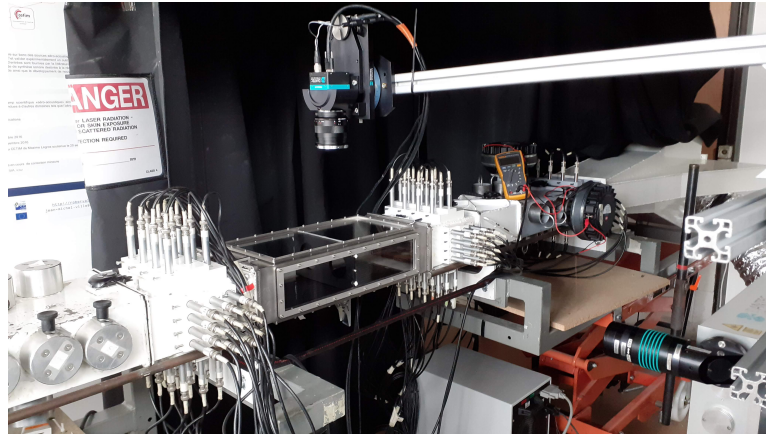


Figure 4.3: Measurement section and PIV setup

4.1.2 Plate geometries tested

Five different sharp-edged orifice plate geometries have been studied. Table 4.1 and Figure 4.4 report the geometry of such plates. A circular shape for the orifice was chosen to both avoid any secondary effects due to the presence

of corners in non-circular geometries (e.g. rectangular) and to facilitate the comparison with the results presented by Tao et al. [37]. The plate porosity ϕ is fixed at 0.25. The thickness t of the plates is also fixed and is set to 8 mm. Even though t^* is not constant, all plates can be considered as ‘thin’ since $t^* \leq 0.2$ in all cases. All plates were fabricated in Plexiglas and fixed by side screws on the walls of the measurement section.

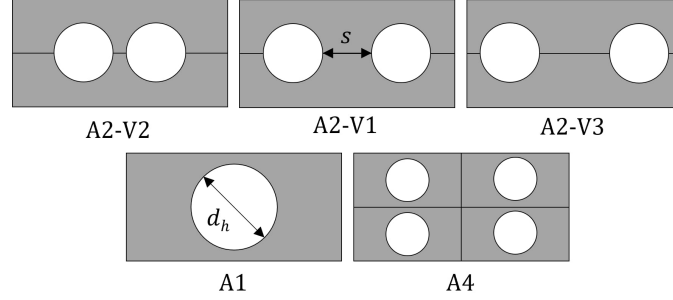


Figure 4.4: Sketch of orifices' positions of tested plate configurations.

Plate ID	A1	A2-V1	A2-V2	A2-V3	A4
d_h [mm]	80	56	56	56	40
s [mm]	-	44	14	70	-
$t^* = t/d_h$ [-]	0.1	0.14	0.14	0.14	2

Table 4.1: Characteristics of the tested perforated plates

The three geometries A1, A2-V1 and A4 (referred to in the following as ‘main geometries’) were designed to selectively enhance or lessen different higher order modes based on the considerations in 3.3. The different positions of the orifices in fact superpose on the surfaces of the main geometries more or less constructively with the specific checkerboard pattern of mode (m, n) , affecting therefore their contribution to the integral in (3.24). An example is the (1,1) mode, where the increasing matching of the orifice(s) to the maxima of $|\psi_{11}(x'_1, x'_2)|^2$ in going from plate A1 to plates A2-V1 and A4 is clear from Figure 4.5. The two additional plate geometries A2-V2 and A2-V3 were instead conceived for investigating the effects involving modes (m, n) with $m \neq 0$ (i.e. with vertical nodal lines). In fact, increasing or decreasing the horizontal spacing s between the orifices translates into an increased or decreased proximity of the ‘rings’ to such nodal lines; see Figure 4.6 for mode (1, 0) for example. Furthermore, their geometry allows to keep to the minimum the number of parameters changed, as the holes’ diameters remain the same, symmetry is maintained and the relative thickness t^* is fixed.

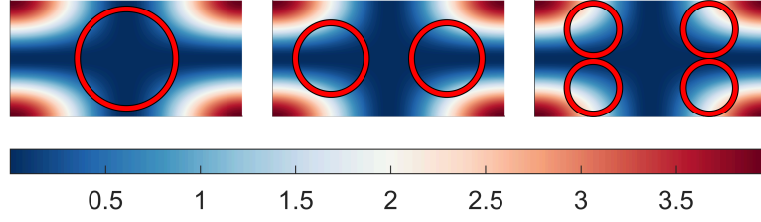


Figure 4.5: Integration area (in red) to be applied in (3.25) (red) over checkerboard pattern of $|\psi_{11}(x'_1, x'_2)|^2$ for plates A1, A2-V1 and A4 from left to right.

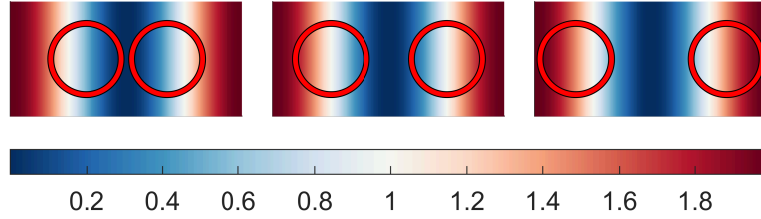


Figure 4.6: Integration area (in red) to be applied in (3.25) over checkerboard pattern of $|\psi_{10}(x'_1, x'_2)|^2$ for plates A2-V2, A2-V1 and A2-V3 from left to right.

4.1.3 2N-port method and setup

The 2N-port method is a generalization to the case of N propagating higher-order modes of the 2-port method first described by Lavrentjev et al. [48]. Its main aim is to calculate the total acoustic power \hat{W}_a generated by an obstacle inserted in an internal flow, as well as to separate the contributions of each propagating higher order mode in a given frequency range; a thorough description of the method can be found in [46].

Its core is to express the forward (\hat{p}^+) and backward (\hat{p}^-) acoustic travelling waves in two cross sections A and B (respectively upstream and downstream of the obstacle, see Figure 4.7) as the sum of a passive and of an active part. The former is due to the effect the obstacle has on the propagation of acoustic waves inside the duct, as it consists of the reflected (\hat{p}_R^\pm) and the transmitted (\hat{p}_T^\pm) components of \hat{p}^\pm . The active part is the actual noise generated by the obstacle's interaction with the flow and it's also known as 'source term' \hat{p}_S^\pm . In the case of N propagating modes, the acoustic waves travelling away from the obstacle are expressed as:

$$\begin{bmatrix} \hat{\mathbf{p}}_{\mathbf{A}}^- \\ \hat{\mathbf{p}}_{\mathbf{B}}^+ \end{bmatrix}_{2N \times 1} = \underbrace{\begin{bmatrix} \hat{\mathbf{R}}^u & \hat{\mathbf{T}}^{d \rightarrow u} \\ \hat{\mathbf{T}}^{u \rightarrow d} & \hat{\mathbf{R}}^d \end{bmatrix}}_{2N \times 2N \text{ scattering matrix } \hat{\mathbf{D}}} \begin{bmatrix} \hat{\mathbf{p}}_{\mathbf{A}}^+ \\ \hat{\mathbf{p}}_{\mathbf{B}}^- \end{bmatrix}_{2N \times 1} + \begin{bmatrix} \hat{\mathbf{p}}_{\mathbf{A},\mathbf{S}}^- \\ \hat{\mathbf{p}}_{\mathbf{B},\mathbf{S}}^+ \end{bmatrix}_{2N \times 1} \quad (4.1)$$

where $\hat{\mathbf{p}}_{\mathbf{A}}^{\pm}$ and $\hat{\mathbf{p}}_{\mathbf{B}}^{\pm}$ are the $N \times 1$ vectors containing the outgoing or incoming (depending on the \pm sign) acoustic modal pressure amplitudes \hat{p}_{A-B}^{mn} , $\hat{\mathbf{R}}^u$ and $\hat{\mathbf{R}}^d$ are $N \times N$ matrices containing the upstream and downstream modal and inter-modal complex reflection coefficients, $\hat{\mathbf{T}}^{u \rightarrow d}$ and $\hat{\mathbf{T}}^{d \rightarrow u}$ are also $N \times N$ matrices for the upstream to downstream and vice-versa modal and inter-modal complex transmission coefficients and finally $\hat{\mathbf{p}}_{\mathbf{A},\mathbf{S}}$ and $\hat{\mathbf{p}}_{\mathbf{B},\mathbf{S}}$ are the outgoing modal source terms.

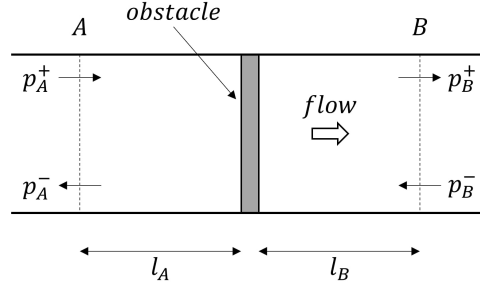


Figure 4.7: Scheme of measurement sections for the 2N-port method in a duct.

The transmission and reflection coefficients are grouped into a $2N \times 2N$ ‘scattering’ matrix $\hat{\mathbf{D}}$ and represent the unknowns of the problem together with the source term. The scattering matrix can be determined through excitation of $2N$ independent acoustic states by displacing a loudspeaker to $2N$ positions (N upstream and N downstream of the obstacle) along the duct.

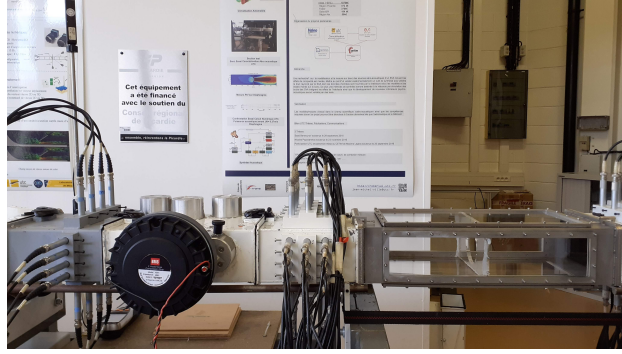


Figure 4.8: Upstream part of the measurement section with movable loudspeaker mounted in one of the $N = 10$ positions on the upstream of the obstacle.

By feeding for each position a known signal $e(t)$ (white noise in the current work) to the loudspeaker and measuring the frequency response function (FRF) between each microphone and such signal, the source term $\hat{\mathbf{p}}_{\mathbf{A}-\mathbf{B},\mathbf{S}}$ is removed since it is independent from the loudspeaker's excitation. A modal decomposition is then performed at each measurement section and the FRFs of the forward and backward traveling components $\hat{\mathbf{p}}_{\mathbf{A}-\mathbf{B}}^{\pm}$ are obtained through the extension to N propagating modes of the two-microphone method [49]. It has to be noted that such a technique can be applied if the expressions of the modal shape functions are known and if the hypothesis of uniform mean axial flow (i.e. 'plug flow') can be accepted. The coefficients of the scattering matrix $\hat{\mathbf{D}}$ can therefore be computed from the FRF form of (4.1). The active part may also be obtained from (4.1) once $\hat{\mathbf{D}}$ is known and the additional source of the loudspeaker is switched off.

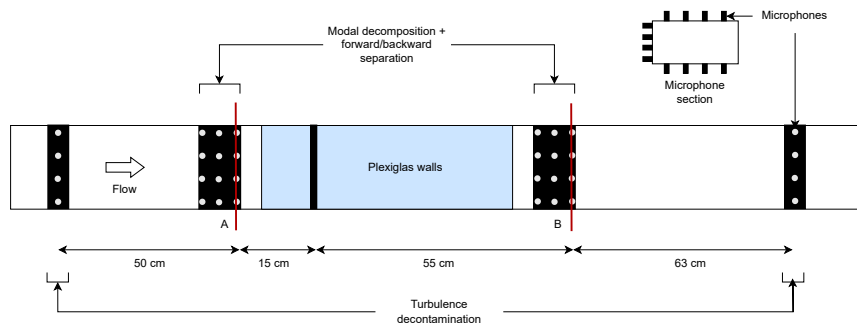


Figure 4.9: Scheme of the measurement section and the position of the microphones.

The present experimental plant was designed to separate and measure the first $N = 10$ higher-order acoustic modes, hence $2N = 20$ lodgements for the loudspeaker are present along the duct's length. Twelve microphones per

section are installed at six different axial positions (three upstream and three downstream of the obstacle) for the modal decomposition and the separation of forward and backward traveling components. Their positions along the duct cross-section were chosen to maximize the superposition with the anti-nodes of the studied higher-order modes [46]. Another two further sections of twelve microphones are added upstream and downstream to limit the effect of turbulent pseudo-sound through the coherent output power method (COP) [50]. In fact, as turbulence is only coherent over relatively short distances, taking the cross-power between two sections sufficiently far apart allows removal of the non-coherent turbulent pseudo-sound while keeping the coherent acoustic part [51]. Preliminary CFD simulations showed that the A1 plate has the longest downstream jet when compared to the other geometries for equivalent conditions, in line with experimental evidence on the influence of the number of orifices [52]. Hence, the A1 plate was tested both at a standard ‘halfway’ position between the upstream A and downstream B measurement sections and in a ‘non-standard’ position closer to the upstream A section for the 2N-port method application at the maximum mass flow rate (Figure 4.9). A comparison between the two configurations showed no differences regarding the upstream measured acoustic power while a less noisy result for the downstream one. This permits to assume that the recovered ‘plug-flow’ hypothesis can be accepted for all geometries, as the other plates produce shorter downstream jets. Once the amplitude of the acoustic pressure of the higher-order propagating modes is known, the acoustic power can be computed [8]. In the current setup, the frequency range of study is set between 200 Hz and 3200 Hz, where the number of propagating modes is eight (4.2).

m	n	f_{mn} [Hz]
0	0	0
1	0	850
2	0	1700
0	1	1700
1	1	1901
2	1	2404
3	0	2550
3	1	3065

Table 4.2: Cut-on frequencies for all propagating modes within the range 200 Hz to 3200 Hz for the rectangular duct under consideration.

4.1.4 PIV setup and procedure

The PIV technique is widely used in the field of fluid mechanics for a quantitative visualization of the flow under study. Its basic principle is to take two images closely spaced in time of a flow region where small particles are present. Through correlation techniques, the instantaneous velocity field in the selected region can then be obtained. Averaging over a suitable number of realizations allows to obtain the average component of the ensemble. A detailed review of the PIV technique can be found in [53].

The system employed in this analysis allows for the estimation of the mean and the rms of the fluctuations of a 2D velocity field in a squared region of interest. The instantaneous velocity field for the n th image couple $\vec{U}_n(\vec{x}) = (u_n, v_n)$ out of N couples is separated through Reynolds' decomposition into an average component (\bar{u}, \bar{v}) and a fluctuating one (u'_n, v'_n) with zero mean (the dependence on the position has been dropped for ease of notation). From the average flow field, the average vorticity field can be computed as $\omega_{xy} = (\partial \bar{v} / \partial x - \partial \bar{u} / \partial y)$. From the rms of the square of the fluctuating components instead, the turbulence kinetic energy $k = 0.5(\bar{u'^2} + \bar{v'^2})$ is obtained.

Detailed setup

The image acquisition unit is the CCD camera FlowSense 4M 2048×2048 pixels by Dantec. The camera mounts a ZEISS Makro-Planar T* lens of 50 mm of focal length with a fully-opened aperture at f#2. The laser unit is composed of the dual-cavity flash-pumped Nd:YAG laser DualPower 135-15 by Dantec and of the light sheet module. Such a device produces a 425 mJ double pulsed laser of wavelength equal to 532 nm for a duration of 9 ns. The thickness of the light sheet is in the order of 2 mm in the region of interest and its repetition rate is set to 10 Hz. The camera is positioned at such a distance so as to have a measurement area of 85 mm × 85 mm, centered on the laser sheet optics unit (Figure 4.11). Camera and laser are jointly fixed to an electronically-controlled traverse system which enables movements of the ensemble in the three directions with a precision of 0.5 mm (Figure 4.3). The camera works in double exposure-mode and the time between two successive pulses is set to 32 μ s so that seeding particles move a distance ranging between 1/4 to 1/2 the size of the interrogation area, as suggested in [54]. The total number of image pairs recorded is 1000. Glycerin is seeded to the flow through a heated fog generator (F2010 Plus by Safex) releasing directly into the fan (Figure 4.10).



Figure 4.10: Fog generator discharging glycerine directly into the blower for PIV acquisitions.

The mean particle size is $1\ \mu\text{m}$. The acquired images are analyzed using the Adaptive Correlation method available in Dantec's software DynamicStudio. Such an algorithm iteratively applies a cross-correlation analysis over increasingly smaller interrogation areas down to the desired dimension. The sizes of the initial and final interrogations areas are set to 128×128 pixels and 32×32 pixels, respectively. The interrogation area overlap is set to 50%, resulting in a spatial resolution of roughly 0.65 mm.

The aim of the PIV measurement was to study the flow in the near-field of the orifice plate, both upstream and downstream. In particular, the main interest is in the distribution of the rms of the turbulent velocity fluctuations in the vicinity of the orifices' edges (see 3.3). Hence, the measurement area was chosen so as to maximize the visibility of the region of interest. In order to reduce to the minimum light reflection effects from the obstacle itself, all tested plates were painted in matte black. A scheme of the PIV measurement area and the relative reference systems for the three main plate geometries tested is reported in Figure 4.11.

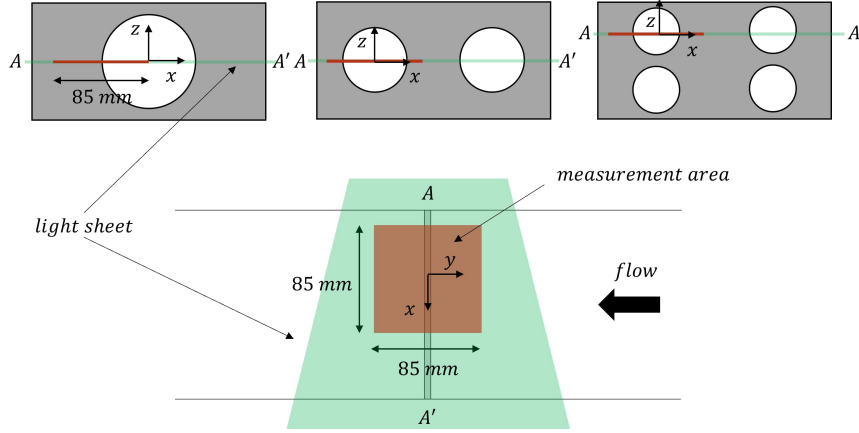


Figure 4.11: Schematic showing the size and the position of the PIV measurement area with respect to orifice plate configuration.

4.2 Preliminary work

4.2.1 Pressure losses

The static pressure loss Δp_{tot} measured between the stabilization tank and the duct's end is the summation of the pressure losses due to the test line Δp_{tl} (distributed losses and concentrated losses caused by Venturimeter, non perfectly-aligned joints, etc.) and the localised pressure drop Δp_R caused by the installation of the obstacle. The models of in-duct aerodynamic noise generation by obstacles discussed in Chapter 3 only take into account the pressure drop Δp_R caused by the obstacle. Therefore, if a comparison of the experimental results with such models is to be performed, it's necessary to separate the two contributions. To obtain an expression for the pressure losses Δp_{tl} , an 'equivalent-length' approach is followed. In particular, such pressure losses are computed by selecting an equivalent length of the rectangular part of the line L_{eq} which would lead, through distributed-losses only, to the same pressure loss $\Delta p_{tot} = \Delta p_{tl}$ measured on the actual configuration when no obstacle is inserted. Such an assumption can be verified by considering that the distributed pressure loss Δp_d is proportional to the dynamic pressure through the Darcy factor f_{Darcy} :

$$\Delta p_d = f_{Darcy} \frac{L}{D_h} \frac{\rho U^2}{2} \quad (4.2)$$

where ρ is the fluid's density, L and D_h are respectively the duct's length and the duct's hydraulic diameter and U the mean velocity in the duct. The density and the mean velocity can be computed from the knowledge of the temperature T , the static pressure, the mass flowrate \dot{m} and the geometry

of the duct. For the case of fully developed turbulent flow in rectangular ducts, the Darcy friction factor can be estimated through the formula [55]:

$$f_{Darcy} = \frac{0.178}{Re_{D_h}^{\frac{1}{5}}} \quad (4.3)$$

where Re_{D_h} is the Reynolds number with respect to the hydraulic diameter of the duct. Setting a constant viscosity $\mu_{air} = 1.87 \cdot 10^{-5} \text{ Pa} \cdot \text{s}$, minimizing the squared difference between the measured Δp_{tot} and the theoretical Δp_d by changing the value of L an equivalent length L_{eq} of 71 m is found. It can be noticed that from (4.2), the relationship between U (and hence \dot{m}) and Δp_d is quadratic. The pressure drop caused by the insertion of the obstacle can then be retrieved by simple subtraction:

$$\Delta p_R(U) = \Delta p_{tot}(U) - \Delta p_{tl}(U) \quad (4.4)$$

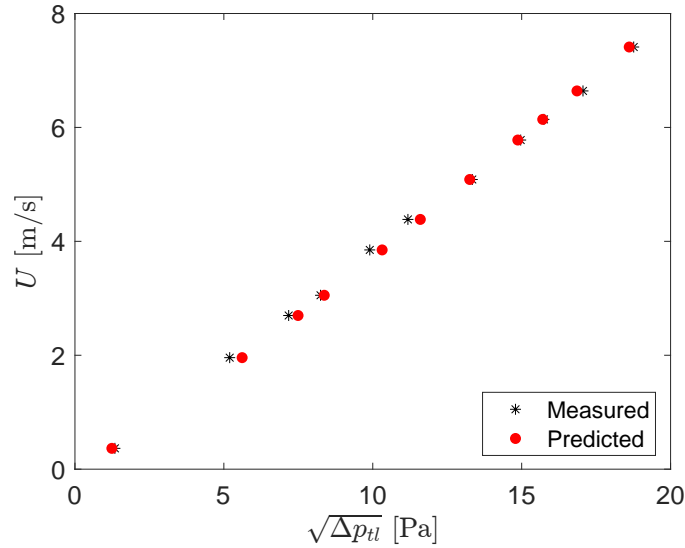


Figure 4.12: Average duct velocity v.s. squared root of measured and predicted test line pressure loss by employing ‘an equivalent length’ L_{eq} of 71 m of rectangular duct.

4.2.2 Microphones calibration

All microphones employed in the application of the 2N-port method described in 4.1.3 are calibrated in amplitude and phase with respect to a reference to allow for simultaneous acoustic pressure measurements. The calibration is performed in two steps. First, the reference microphone is calibrated in amplitude through a sound calibrator (Rion NC-74) which

generates a constant sound pressure of 94 dB (ref. $2 \cdot 10^{-5}$ Pa) at a frequency of 1 kHz. Supposing a flat-type of response, the transfer function of the reference microphone \hat{H}_{ref} is obtained. Such function transforms the signal from Volts to Pa through the measured sensitivity (46.7 mV/Pa). Then, each microphone is calibrated in amplitude and phase with respect to the reference through a phase calibrator (GRAS 51AB). Supplying white noise in the frequency range 100 Hz to 6700 Hz simultaneously to the two microphones, the frequency response function (FRF) of the microphone M_n to be calibrated with respect to the reference is obtained as:

$$\hat{H}_{ref,M_n} = \frac{\hat{S}_{ref,M_n}}{\hat{S}_{ref,ref}} \quad (4.5)$$

where $\hat{S}_{ref,ref}$ is the auto-spectrum of the signal (in Volts) produced by the reference microphone and \hat{S}_{ref,M_n} is the cross-spectrum between such signal and the one produced by the microphone M_n . The FRF defined in (4.5) is a complex quantity, whose real and complex parts correspond to the amplitude ratio and phase shift between the two microphones respectively. Finally, the transfer function (in mV/Pa) of the M_n microphone can be retrieved as:

$$\hat{H}_{M_n} = \hat{H}_{ref,M_n} \cdot \hat{H}_{ref} \quad (4.6)$$

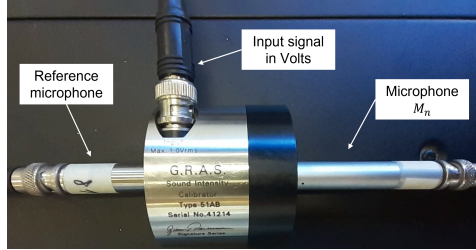


Figure 4.13: Phase calibration with respect to reference microphone with GRAS 51AB.

4.2.3 Acoustic behavior of empty duct

Before proceeding with the acoustic characterization of the perforated plates by means of the 2N-Port method, the characteristics of the ‘empty duct’ (i.e. no obstacle inserted) are reported. On the one hand, this permitted to test that all components were working properly. On the other, it allowed to obtain a ‘reference’ solution for comparison with the perforated plates configuration.

The scattering matrix $\hat{\mathbf{D}}$ of a perfectly-rigid duct without any internal obstacle and with perfect anechoic terminations should have elements with zero-

amplitude for each diagonal element of the reflection coefficient $\hat{\mathbf{R}}^{\mathbf{u}-\mathbf{d}}$ and with unitary amplitude for each diagonal transmission one, as each mode is perfectly transmitted [45]. However, due to the flexible nature of the duct's walls, the non-perfect anechoic terminations and possible manufacture imperfections this theoretical result will partly differ from the measured one.

No flow The reflection and transmission coefficients' amplitude of the plane wave $(0,0)$ mode in case of no flow are reported in Figure 4.14 for both the upstream to downstream case and vice versa. It can be seen that the values of the coefficients approach those expected from the theory starting from frequencies higher than roughly 800 Hz. The peaks for the reflection coefficients (and of the troughs for the transmission ones) occur at the natural frequencies of vibration of the duct walls, a fact that was confirmed through vibration measurements.

With flow The effect of a uniform (low Mach number) flow should be limited to adding a shift to the phase of the complex reflection/transmission coefficients. The change of phase of a signal propagating one-dimensionally between two sections separated by a distance Δ can be computed theoretically as [56]:

$$\hat{\theta} = 2\pi f \frac{\Delta}{c + U} \quad (4.7)$$

The modules of the complex coefficients $\hat{R}_{00,00}^u$ and $\hat{T}_{00,00}^{u-d}$ are reported in Figure 4.15 for two different average duct velocities. The phase of $\hat{T}_{00,00}^{u-d}$ for the same velocities and for the no-flow case is reported in Figure 4.16. The superposition of the modules (and the addition of noise from the flow) and the shift in the phase are both evident.

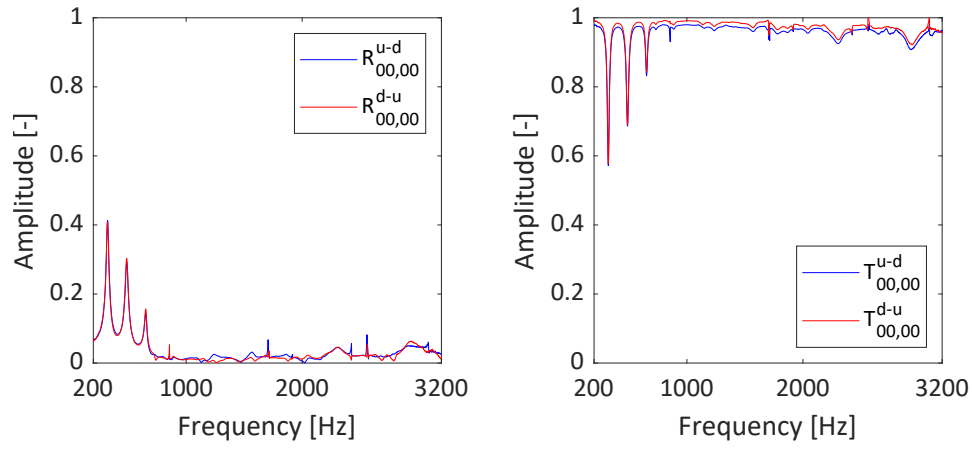


Figure 4.14: Amplitudes of the complex reflection coefficients (left) and transmission coefficient (right) for the plane wave (0,0) mode in both upstream to downstream and downstream to upstream directions.

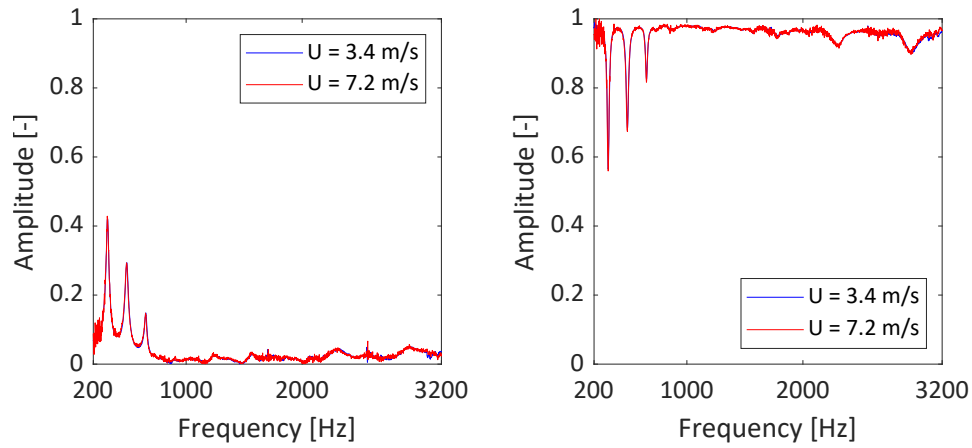


Figure 4.15: Amplitudes of the complex upstream reflection coefficients (left) and upstream to downstream transmission coefficient (right) for the plane wave (0,0) mode for two average duct velocities.

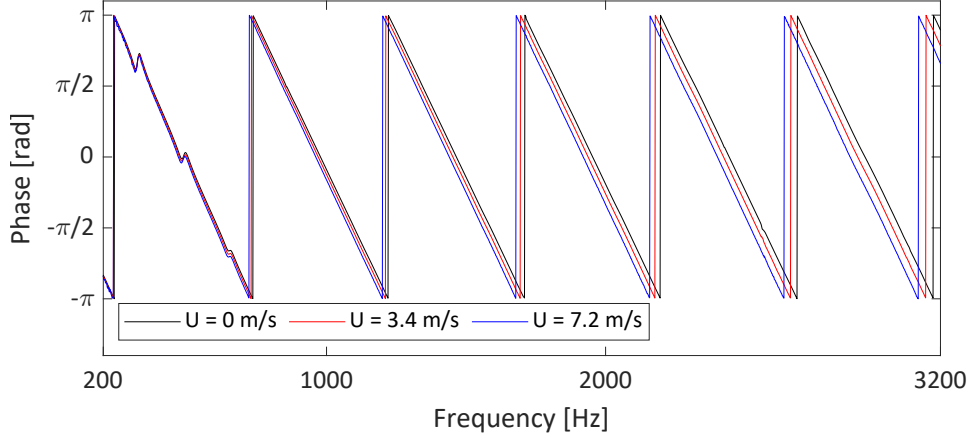


Figure 4.16: Phase of the upstream to downstream transmission coefficient for the plane wave (0,0) mode for two different average duct velocities and for the no-flow case.

4.2.4 PIV validation on empty duct

As the PIV setup was mounted in a different configuration with respect to previous works, a preliminary campaign on the empty duct was performed for validation. An average duct velocity of 7.2 m/s (based on the measured mass flow rate) was imposed, so as to obtain the same average duct velocity which would correspond to a jet Mach number of 0.13 when the obstacles were inserted. The visualization area was centered on the ducts' longitudinal axis and the camera was placed at a distance such that the area measured 185 mm x 185 mm.

The results for 200 averages are reported in Figure 4.17. At the top left, the mean flow velocity magnitude $|\vec{U}|$ shows a near-uniform distribution over the measurement area, with values consistent with the imposed flow rate. A slight decrease for increasing values of x can be noticed. This is due to the fact that as the light sheet expands, the available energy decreases and less light scattering occurs. At the top right, the average turbulence kinetic energy shows very small fluctuations evenly distributed in space. At the bottom of the figures, the relative error e_{rel} for both the velocity amplitude and the turbulence kinetic energy at the center point (100 mm, 100mm) is shown. Such relative error is defined as:

$$e_{rel} = 100 \times \left(\frac{\bar{\xi}_{final} - \bar{\xi}_i}{\bar{\xi}_{final}} \right) \quad [\%] \quad (4.8)$$

where $\bar{\xi}_{final}$ is the final average value of a given quantity ξ at the end of a time series and $\bar{\xi}_i$ is the cumulative average up to the i -th image couple. It can be

seen that while the average velocity amplitude quickly goes to convergence, the turbulence kinetic energy requires a higher number of averages.

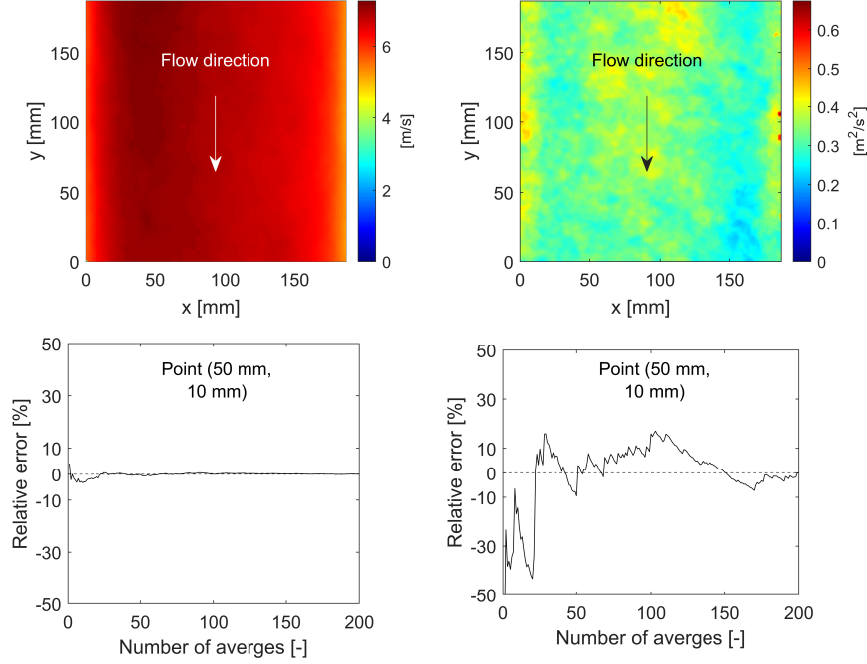


Figure 4.17: Average velocity amplitude (up, left) and average turbulence kinetic energy (up, right) on a visualization area of 185 x 185 mm as obtained through a 2D PIV setup. Convergence of average velocity amplitude (bottom, left) and turbulence kinetic energy (bottom, right) at a point in the flow visualization area.

4.3 Results

4.3.1 Added resistance of tested perforated plates

The dimensional and the non-dimensional relationship between the pressure drop Δp_R (calculated as described in 4.2.1) caused by the different obstacles and the mass flow rate are reported in Figure 4.18. The linearity of the relationship between U and $\sqrt{\Delta p_R}$ is clear. After an initial dependence on Re , the non-dimensional pressure drop K_L stabilizes and shows a constant value for all geometries, as expected (see 2.1.2). It is worthwhile to notice that values of the pressure loss coefficient K_L in such self-similarity region are very close between the different plate geometries. This suggests a limited

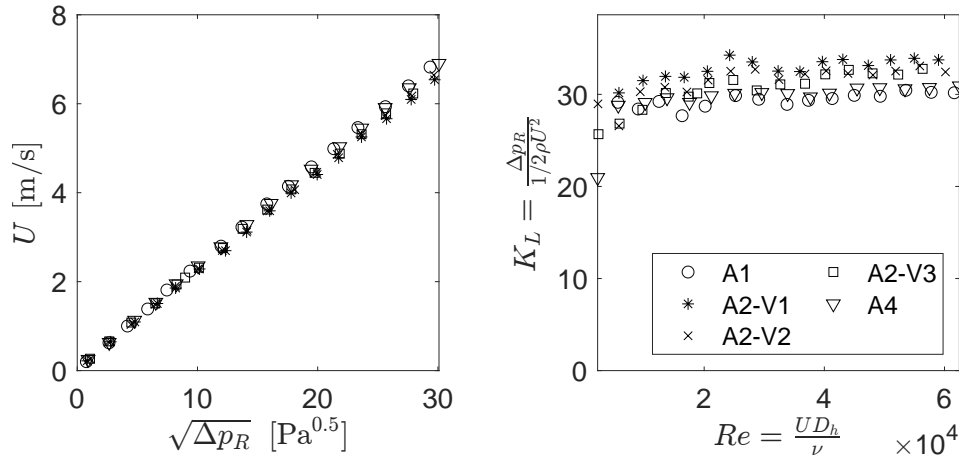


Figure 4.18: Dimensional (left) and non-dimensional (right) relationship between pressure drop and averaged duct velocity for all plates tested.

dependence of the obstacles' pressure drop on the holes' number and distribution compared to the flow to total area ratio of the plates. Such a feature must be particularly highlighted in view of the results presented in 4.3.2. In fact, the theory presented in 3.1.2 makes the hypothesis that the emitted acoustic power is proportional to the drag force acting on the plate. The non-negligible acoustic power difference between the various plates observed might hence be explained by the enhanced (or lessened) acoustic coupling between orifices' number and position and the higher order modes discussed in 3.3 of Chapter 3.

4.3.2 Noise generation

The noise generation characteristics of the tested plates are now dealt with. In particular, some remarks on the acoustic source type are first made to show that the subsequent analyses can be performed only on the acoustic power measured in the section upstream of the tested device without any loss of generality. Then, the emitted acoustic power spectral characteristics of the three 'main' plate geometries are presented. A comparison of the obtained results with the available theory on the 'generalized source spectrum' discussed in 3.1.2 is then provided. Finally, the modal content of the internal acoustic field is analyzed for a fixed average duct velocity for all the plates tested. The role of the 'modal efficiency coefficient' of 3.3.1 in explaining the results is also discussed.

Equivalent acoustic source type

The models described in section 3.1 make the assumption that local Mach numbers be sufficiently small ($Ma < 0.3$) and that the source can be consid-

ered as dipolar. The maximum jet Mach number $M_j = U_j/c$ (where U_j is computed as in (2.14)) for the case of the maximum mass flow rate acoustically tested results in $M_j \approx 0.13$.

To investigate the validity of the second hypothesis (dipolar source), the internal acoustic power spectral density \hat{W}_a for the three main plate geometries was measured for various jet Mach numbers in both the upstream and the downstream test sections. In fact, any source behaving like a dipole distribution should radiate acoustic energy equally on both sides when flow convection effects are negligible [57]. In Figure 4.19 the absolute difference between the upstream and the downstream sound power level (SWL) in fine bands for the three plate geometries at the maximum jet Mach number tested is shown. The agreement is generally good, with differences mostly contained in a ± 2 dB band for all of the three geometries. The broadband peaks observed in the plane wave range show no dependence on the geometry and on the mass flow rates tested. Their frequencies correspond to those found for the scattering coefficients of the empty duct (see 4.2.3) and a disturbance linked to the experimental setup might be the reason. The small difference between the upstream and the downstream may be also explained by the weaker signal-to-noise ratio in the downstream measurements, as the intense turbulence from the jets' breakdown decreases the coherence between microphone pairs (see 4.1.3).

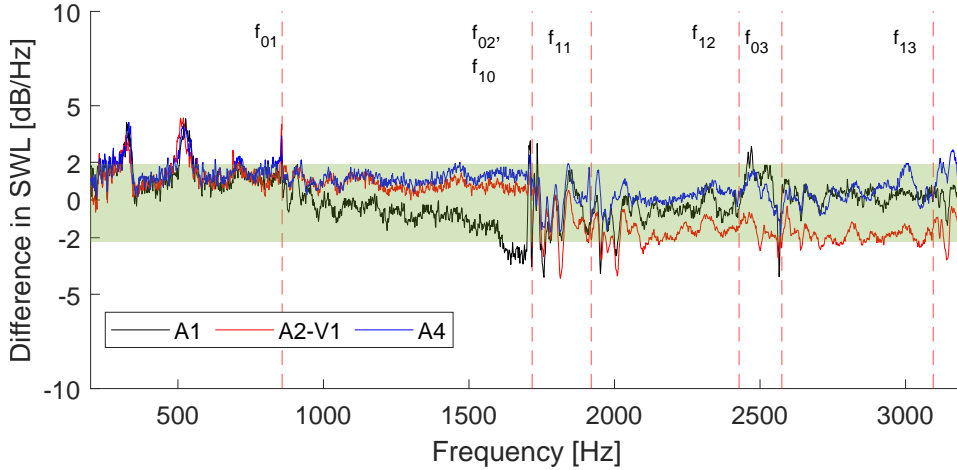


Figure 4.19: Spectra of the absolute difference between upstream and downstream Sound Power Level (SWL) for the A1, A2-V1 and A4 plates at $M_j = 0.13$. Cut-on frequencies of higher order modes are also reported as dashed red lines; ± 2 dB band is highlighted in green.

In Figure 4.20 the non-dimensional power law $\hat{W}_a^* \propto M_j^\alpha$ for the three plate geometries tested using one-third octave bands spectra of the upstream

acoustic power for different constant frequency scalings is reported. The non-dimensional acoustic power \hat{W}_a^* is obtained through subdivision by the kinetic energy flux $\phi_{kin} = 0.5\rho U^3$. The frequency is scaled both through the Helmholtz number $He = fD/c$ and through the Strouhal number as defined in (3.18). The scaling based on the Helmholtz number isn't sensitive by definition to flow effects, while the scaling based on the Strouhal number is used whenever a flow effect on the frequency is relevant, such as in whistling phenomena [22]. At the top, the power law relative to a constant Helmholtz number corresponding to center frequencies 500 Hz (plane-wave region) and 3162 Hz (eight propagating modes) is shown. At the bottom, the same quantity at two constant Strouhal numbers is reported. Good linearity is achieved if the non-dimensional total acoustic power is plotted against M_j in a logarithmic scale, especially so at constant Helmholtz numbers. In this case, for the A2-V1 and A4 plates the power law exponents tend to ≈ 5 below cut-on and to ≈ 7 above; for the A1 case the exponents are 6.2 below cut-on and 7.6 above. Similar results are found downstream. At constant Strouhal numbers on the other hand, the power laws do not approach the results theoretically predicted by Nelson & Morfey [30] ($\alpha \propto 4$ below cut-on and $\alpha \propto 6$ above, see 3.1.2).

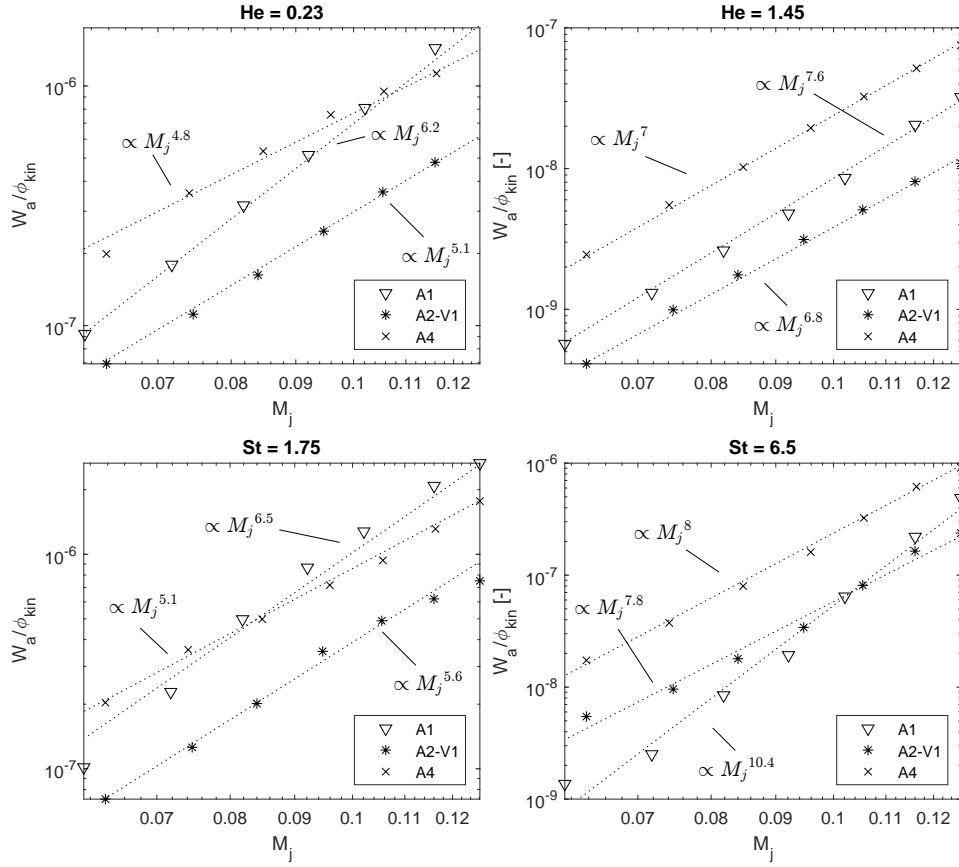


Figure 4.20: Non-dimensional upstream acoustic power versus the jet Mach number M_j (log-scale) for constant Helmholtz numbers (top) and constant Strouhal numbers (bottom).

The power law exponents computed for different constant Helmholtz and Strouhal numbers for the three main plate geometries are shown in Tab. 4.3. The shift occurring as more higher-order modes become propagational is evident in both cases; as well as the peculiar behavior of the A1 plate when compared to the other two geometries. It is also worth noticing that the power law exponent for a given plate shows similar values between low St and He numbers; an observation which is not true for higher $St-He$ values. Combining all of the results, the A2-V1 and A4 plates seem to confirm at least in part a dipole-like behavior if a constant Helmholtz approach is considered. The A1 plate's equivalent source mechanism is instead more uncertain, showing elements of both dipolar and quadripolar sources. In order to factor out the possible effects of turbulence pseudo-sound, it is chosen in the following to analyze the upstream results only, without any loss of generality as the substantial equivalence between the upstream and the downstream sides has been demonstrated.

Constant He				Constant St			
He	α			St	α		
	A1	A2-V1	A4		A1	A2-V1	A4
0.23	6.1	5.1	4.8	1.75	6.5	5.6	5.1
0.47	6.4	5.6	6.1	2.7	8.1	6.8	6.1
0.72	6.7	5.3	6	3.65	9	7	6.8
0.96	7.5	5.8	6.8	4.6	9.6	6.9	7
1.2	7.6	6.7	7.1	5.55	10.4	7.4	7.6
1.45	7.6	6.8	7.1	6.5	10.4	7.8	8

Table 4.3: Power law exponents at different constant Helmholtz and Strouhal numbers for the main plate geometries tested.

Emitted internal acoustic power

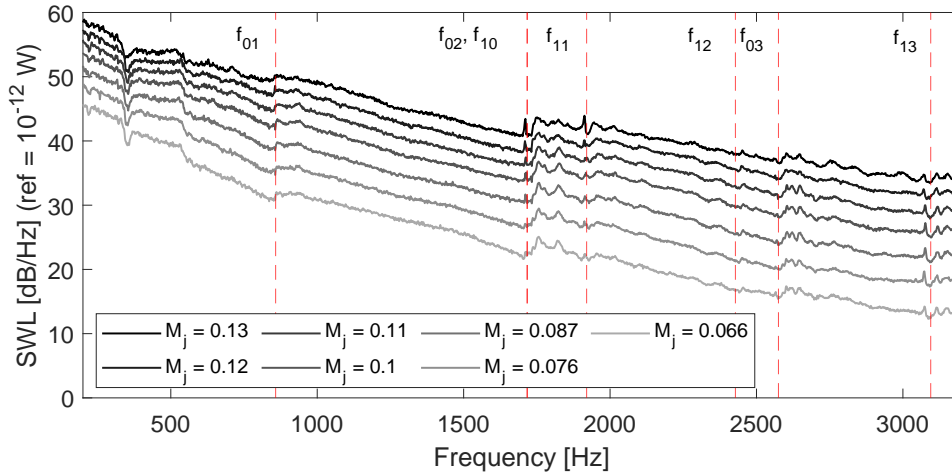


Figure 4.21: Upstream SWL spectrum at different mass flow rates for plate A4. Cut-on frequencies are highlighted in red.

The results in terms of the produced upstream SWL for different jet Mach numbers for the A4 plate are reported in Figure 4.21. The remarkable vertical alignment between the curves, which are just shifted upwards with increasing mass flow rates, proves that in the range of Mach numbers tested the acoustic behavior of the duct (shift in cut-on frequencies) is not influenced by the flow except for the amplitude of the generated sound. A similar trend was obtained for the other two ‘main plates’. A comparison between the SWL generated by the three main plates for $M_j = 0.13$ is reported in the Figure 4.22. The A4 plate results in a stronger noise generation over almost the whole frequency range tested. The A1 and the A2-V1 configurations show a more similar behavior except for the plane wave range.

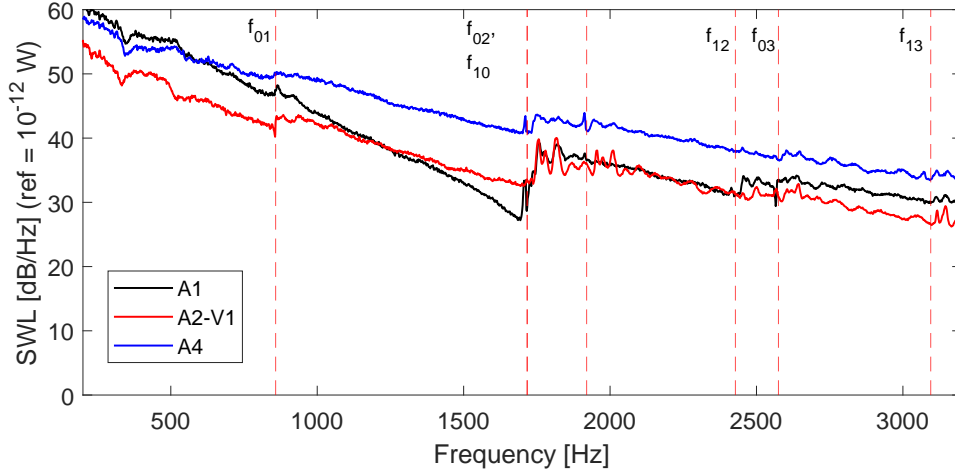


Figure 4.22: Upstream SWL spectrum at $M_j = 0.13$ for plates A1, A2-V1 and A4. Cut-on frequencies are highlighted in red.

Generalized spectrum

The generalized spectrum $K^2(St)$ was computed by:

- making use of the ‘momentum flux’ theory for the computation of the average total force \bar{F}_3 acting on the plate as proposed by Kårekull et al. [35] and discussed in 3.1.2;
- employing (3.12) for expressing the frequency content of the total force F_3 ;
- retrieving $K^2(St)$ from (3.9) and (3.11) as the acoustic power \hat{W}_a was known from measurement.

The result is reported in the left graph of Figure 4.24 for varying jet Mach numbers of the A4 configuration. The same quantity computed for $M_j = 0.13$ for plates A1, A2-V1 and A4 is reported in the right graph of the same Figure 4.24. A remarkably good overlap is observed at lower Strouhal numbers if the geometry is kept constant and the mass flow rate is varied. A relatively good overlap is also seen between the different plates at low Strouhal numbers, where the maximum absolute difference is ≈ 5 dB. At higher Strouhal numbers, the curve relative to the A1 plate tends to that of the A2-V1 plate and the overall maximum difference between the plates is higher, in the order of 10 dB. These results confirm that in the plane wave region (i.e. for low Strouhal numbers) a ‘generalized spectrum’ for a given family of obstacles may be present. However, as higher order acoustic modes become propagational, the more geometry-specific coupling between

the modal shape function $|\psi_{mn}(x'_1, x'_2)|^2$ and the PSD of the force distribution $S_f(x'_1, x'_2)$ discussed in 3.3 of Chapter 3 may play a role in the deviation from the theoretical trend observed.

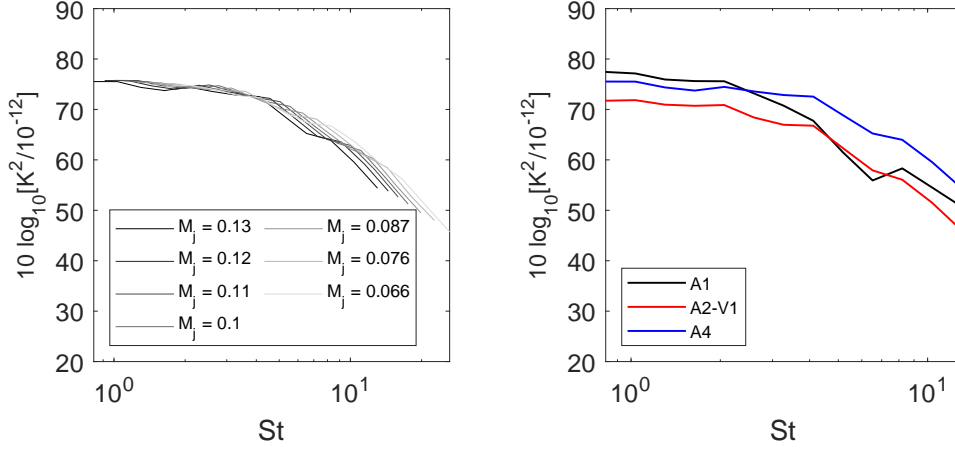


Figure 4.23: Generalized source spectra K^2 for (left) A4 plate at various jet Mach numbers and for plates A1, A2-V1 and (right) A4 at $M_j = 0.13$.

A best fit line for the spectra obtained is given by the equations:

$$10 \log_{10} \left(\frac{K^2}{10^{-12}} \right) = \begin{cases} 74 & \text{if } St < 2.5 \\ 85 - 28 \log_{10}(St) & \text{if } St \geq 2.5 \end{cases} \quad (4.9)$$

Compared to the expression (3.21) suggested by Kårekull et al. [35], it can be seen that the -28 multiplication factor is retained while the amplitude for the constant part of the spectrum and the threshold St for the slope change are modified.

Modal content of internal acoustic field

The ‘modal efficiency coefficient’ Ψ_{mn} defined in (3.25) is reported in the left plot of Figure 4.25 for the three main geometry types and for the measurable higher-order modes. From a first inspection of the result, it is evident that the plate A4 seems to be more efficient than the other two geometries in exciting the highest number of higher order acoustic modes. Referring to the right plot of Figure 4.25, the changes of Ψ_{mn} between the variations of the A2 geometries are less pronounced when compared to the A1 and A4 plates. This had to be expected because the integration area A_{ring} remains the same in the former case, while it increases in the latter in going from plate A1 to plate A4, having kept the ring’s width constant. The biggest variations are for the cases of the (1,0), (1,1) and (3,0) modes. On the contrary, the only mode symmetrical about the horizontal (0,1) correctly does not change its value between the three geometries.

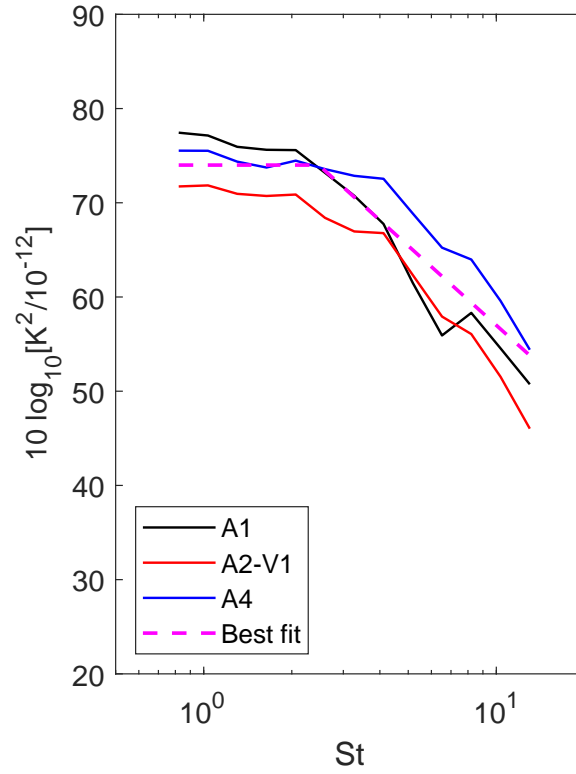


Figure 4.24: Generalized source spectra K^2 for plates A1, A2-V1 and A4 at $M_j = 0.13$ v.s. the best fit.

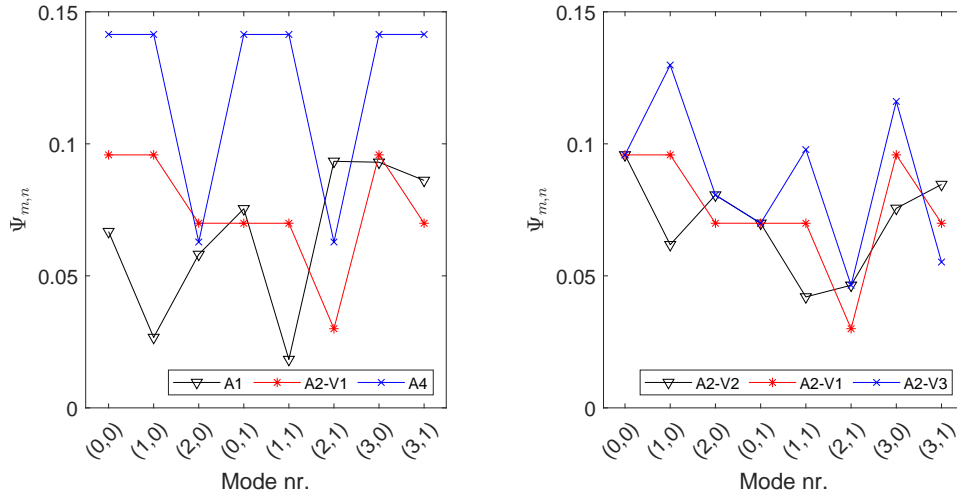


Figure 4.25: Comparison of modal efficiency coefficient Ψ_{mn} between (left) plates A1, A2-V1 and A4 and (right) between plates A2-V1, A2-V2 and A2-V3 for the eight propagating acoustic modes in the duct in the frequency range 200 Hz to 3200 Hz.

The upstream modal SWL of plates A1, A2-V1 and A4 is reported in Figure 4.26 for all propagating modes in the frequency range of study and for the maximum mass flow rate ($M_j = 0.13$). Differences of up to 10 dB are observed in the amplitudes of the spectra, highlighting the important role played by the perforations' positions. The tendency to enhance or lessen specific higher-order modes by the different geometries is found to be in good qualitative agreement with the trend of the modal efficiency coefficient Ψ_{mn} shown in Figure 4.25. In fact, except for the case of the $(2, 0)$ mode, all the higher order modes reflect the qualitative behavior predicted by Ψ_{mn} . As an example, the SWL of the A1 plate varies from the lowest level between the three plates for the $(1, 1)$ mode to the maximum for the $(2, 1)$ mode, as also indicated by the tendency of Ψ_{11} and Ψ_{21} .

The exception concerning mode $(2, 0)$ corresponds to a low relative difference between the values of $\Psi_{2,0}$ for the main plate geometries, suggesting that such difference may be due to a distinct mechanism other than modal coupling. A comparison of the upstream modal SWL of plates A2-V1, A2-V2 and A2-V3 for the same conditions as the previous case is also reported in Figure 4.27. As expected, differences are less evident than for the three main plate geometries. However, the degree of efficiency of a given geometry in exciting specific modes is once again qualitatively well predicted by the trend of the modal efficiency coefficient Ψ_{mn} in Figure 4.25.

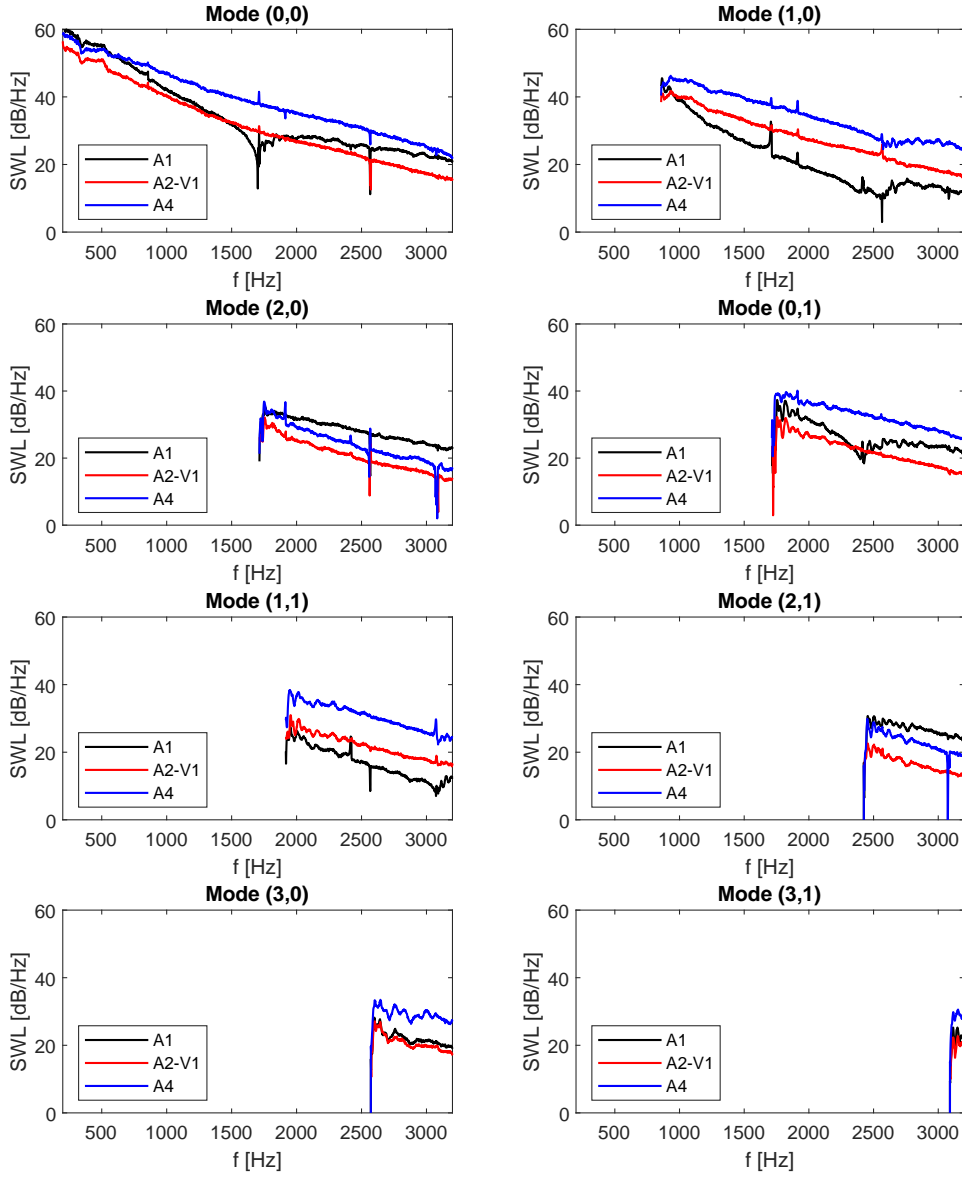


Figure 4.26: Upstream modal SWL of all propagating modes in the frequency range [200 Hz, 3200 Hz] for the three main plate geometries A1, A2-V1 and A4 at the maximum mass flow rate tested ($M_j = 0.13$). (colors online)

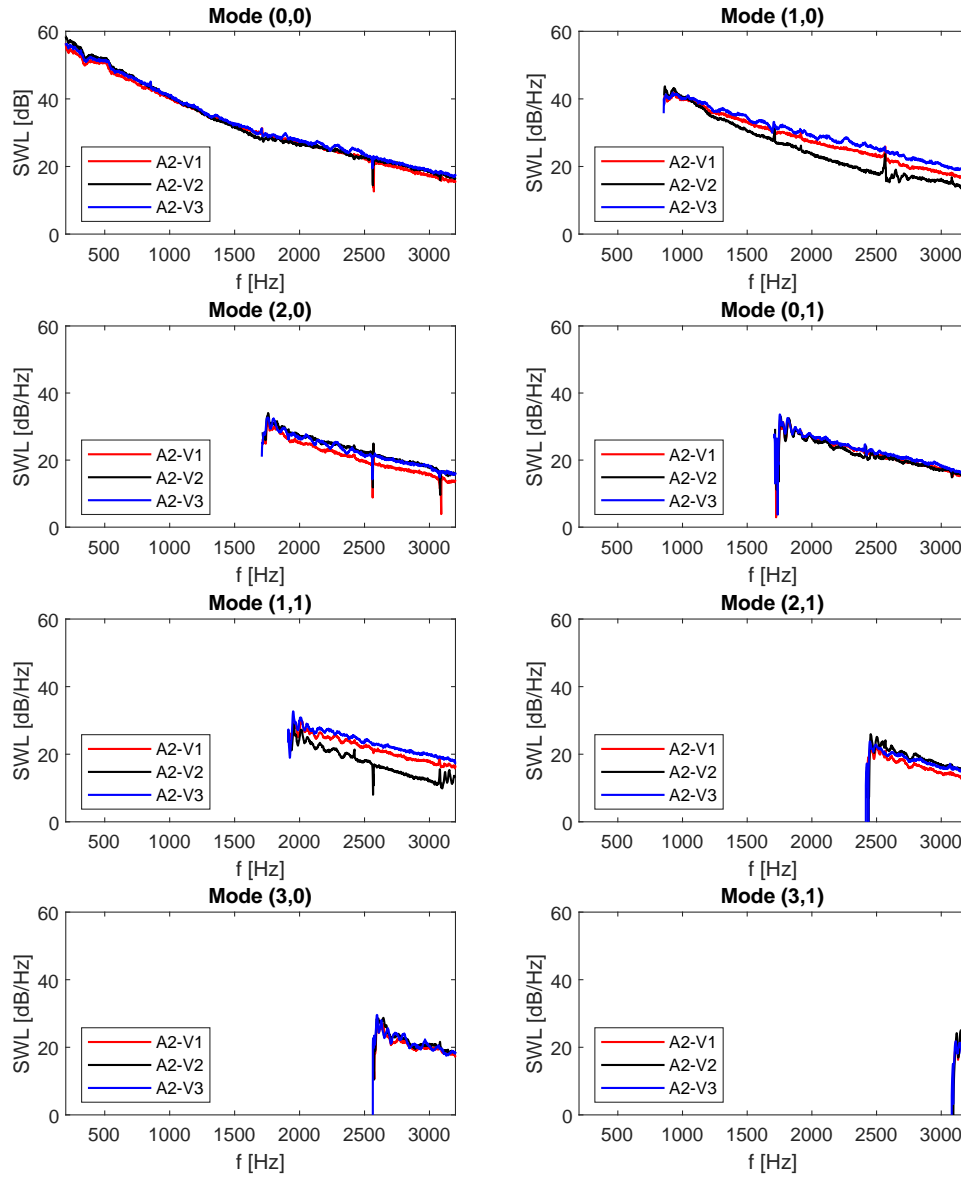


Figure 4.27: Upstream modal SWL of all propagating modes in the frequency range [200 Hz, 3200 Hz] for the three two-orifice plate geometries A2-V1, A2-V2 and A2-V3 for the maximum mass flow rate tested ($M_j = 0.13$). (colors online)

4.3.3 PIV Results

The PIV measurements were performed for each plate at the maximum jet Mach number for which the acoustic measurements were taken ($M_j = 0.13$). In the following, the mean velocity field, the mean turbulence kinetic energy and vorticity distributions are reported for the three main plate configurations (A1, A2-V1, A4) for the positions indicated in 4.11. An image couple before post-processing for the plate A2-V1 is reported in Figure 4.28. Spatial coordinates are normalized with respect to the hole's diameter d_h of the relative plate. Reported quantities (velocity magnitude, turbulence kinetic energy, vorticity) are all normalized with respect to the absolute maximum between the three configurations to better highlight the relative differences. The normalizing factors are 37 m/s for the velocity, $140 \text{ m}^2/\text{s}^2$ for the turbulence kinetic energy and 9.8 s^{-1} for the vorticity.

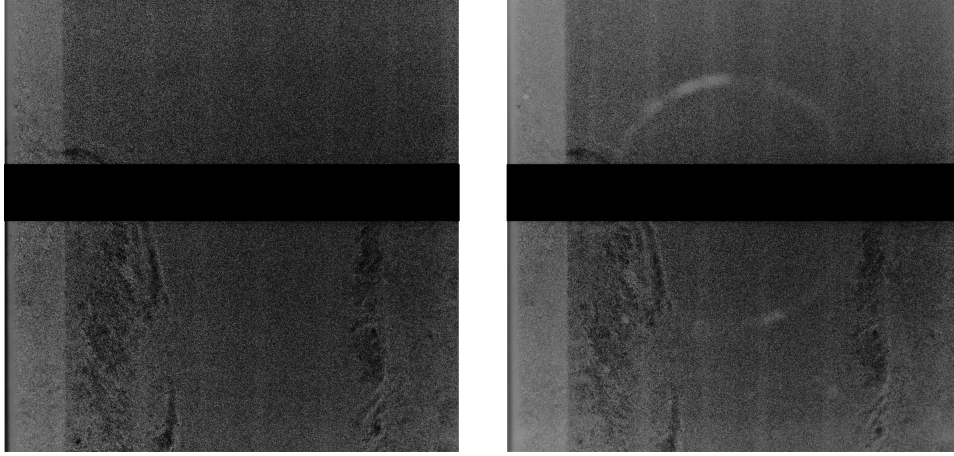


Figure 4.28: Frame couple for PIV ‘instantaneous’ velocity field over the A2-V1 left orifice. Notice that the image on the right is brighter for the higher exposure time. The reflection of the lens’ ring is also visible on the same picture for the same reason.

Mean flow field

The mean flow velocity magnitude $|\vec{U}|$, the mean turbulence kinetic energy $k(\vec{x})$ and the mean vorticity $\bar{\omega}_{xy}(\vec{x})$ for the three plate geometries at the positions indicated in Figure 4.11 are reported respectively in Figure 4.30, 4.31 and 4.32. A convergence study (with the same methodology as described in 4.2.4) was performed to check the stationarity of the studied parameters using a 1000 velocity field measurement for the case of the A1 plate. It was found that all parameters converge starting from a total number of velocity fields of 600, see Figure 4.29. Hence, in the current work, 1000 velocity fields are acquired for each case.

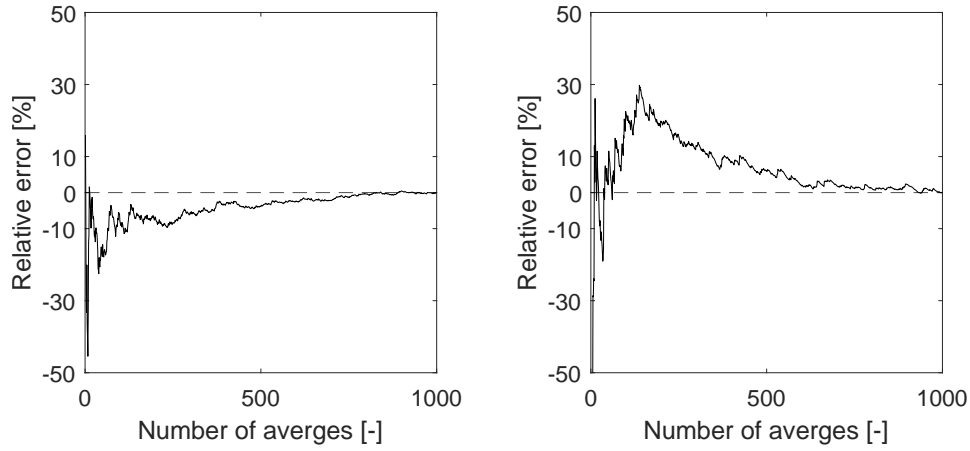


Figure 4.29: Relative error between cumulative average at i -th image couple and final average value of: the mean flow velocity magnitude (left) and the turbulence kinetic energy (right) at a point located (49 mm, 30 mm).

The velocity magnitude displays the characteristic phenomenon of the *vena contracta* detaching from the upstream edge of the perforation and reaching the highest values at a distance of about half an orifice diameter downstream of the orifice. This confirms that the selected thickness t allows for a ‘thin’ plate behavior (see 2.1.2). Furthermore, the asymmetry due to the multiple jets’ interaction is clear both in the case of the A2-V1 and the A4 plates, where the mean flow downstream of the plate seems ‘attracted’ to the neighboring jet in the former and ‘repulsed’ by it in the latter. As expected from the incompressibility of the flow and from having the same flow area A_f in all cases, no difference in the maximum values of the velocity are observed. The greatest relative differences between the three configurations are instead observed with respect to the turbulence kinetic energy distribution (Figure 4.31). In the measurement area, the highest values are reached in the A4 plate at the inner edge downstream of the orifice. Such a result may be explained by the increased jet interactions in the central area of such plate, a consideration which also justifies the presence of the same phenomenon in the A2-V1 configuration. In addition, it is important to highlight the fact that localized increases of turbulence kinetic energy are visible in the immediate vicinity of the orifice in the upstream face of the obstacles, especially in the A2-V1 and A4 plates (see following 4.3.3). Finally, the mean vorticity field $\bar{\omega}_{xy}(\vec{x})$ (Figure 4.32) clearly shows the presence of clockwise ($\bar{\omega}_{xy} > 0$) and counterclockwise ($\bar{\omega}_{xy} < 0$) rotating regions in the shear layer of the downstream jet and in the separation region on the edge of the orifice upstream.

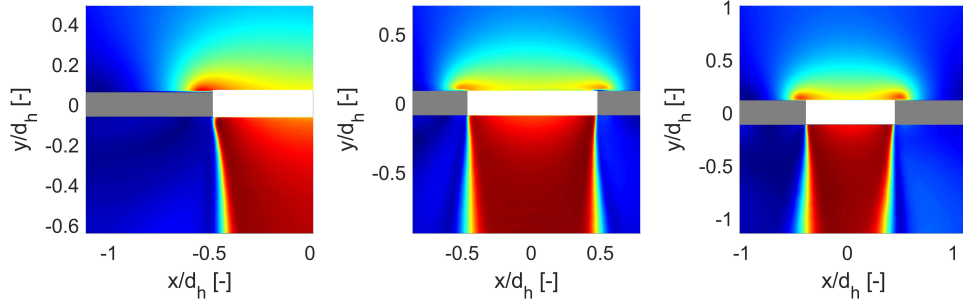


Figure 4.30: Normalized mean flow velocity magnitude for plates A1 to A4 from left to right for $M_j = 0.13$ Values range from 1 (dark red) to 0 (dark blue). Solid surface is represented in gray and orifice's position in white.

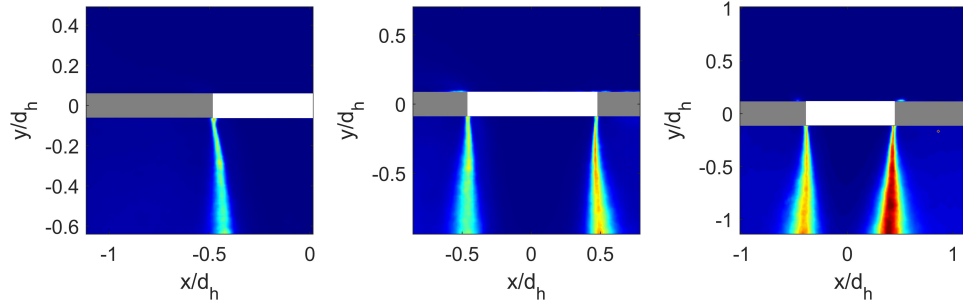


Figure 4.31: Normalized mean turbulence kinetic energy field for plates A1 to A4 from left to right for $M_j = 0.13$ Values range from 1 (dark red) to 0 (dark blue). Solid surface is represented in gray and orifice's position in white.

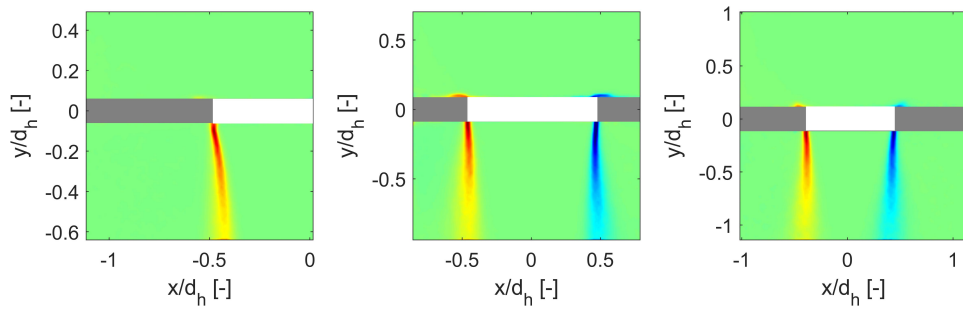


Figure 4.32: Normalized mean vorticity field for plates A1 to A4 from left to right for $M_j = 0.13$ Values range from 1 (dark red) to -1 (dark blue). Solid surface is represented in gray and orifice's position in white.

Fluctuating normal velocity distribution on solid surface

As hinted at in 3.3.1 and as possibly confirmed by the findings in the previous paragraphs, the distribution of the fluctuating force on the surface of the perforated plate might be responsible for a ‘selective modal excitation’. However, a direct measurement of the fluctuating force distribution in magnitude over the obstacle’s surface requires modifications of the obstacle itself, e.g. insertion of pressure taps over its surface [36]. An indirect approach to estimating such distribution may be however obtained from the PIV technique through the work of Mak et al. ([58, 59]). Considering a small fluid element adjacent to a solid spoiler perpendicular to the flow and assuming its mass concentrated in its center of gravity, the authors applied a momentum balance and obtained a proportionality for the root mean square (rms) of the point fluctuating drag force $f'_{3,rms} \propto dA_s (u'_{rms})^2$, with dA_s the small element’s area adjacent to the surface and u'_{rms} the rms of the fluctuating velocity component perpendicular to the surface referenced to the center of mass. This latter quantity can be retrieved through PIV analysis, therefore allowing an indirect qualitative estimation of the distribution of the fluctuating force magnitude over the obstacle’s surface.

The measured rms distribution of the velocity component perpendicular to the plate is now discussed. Due to light scattering effects as well as shadowing from the obstacle itself, measurements too close to the plates’ surfaces displayed non-physical results and were therefore discarded. Instead, a distance of about 2 mm (both upstream and downstream) was judged sufficiently far from the surface to not be influenced by such effects while remaining close enough for capturing near-field relevant flow characteristics. Also, it was chosen to report the results only for the range $[-1 \leq x/d_h \leq -0.5]$; such range permitting to exclude the region most affected by the shadowing due to the orifice’s edge and the position of the laser. The dimensional squared rms value of the velocity fluctuations perpendicular to the plate’s surface, upstream and downstream of the relative plate, are reported in Figure 4.33 for all the geometries tested.

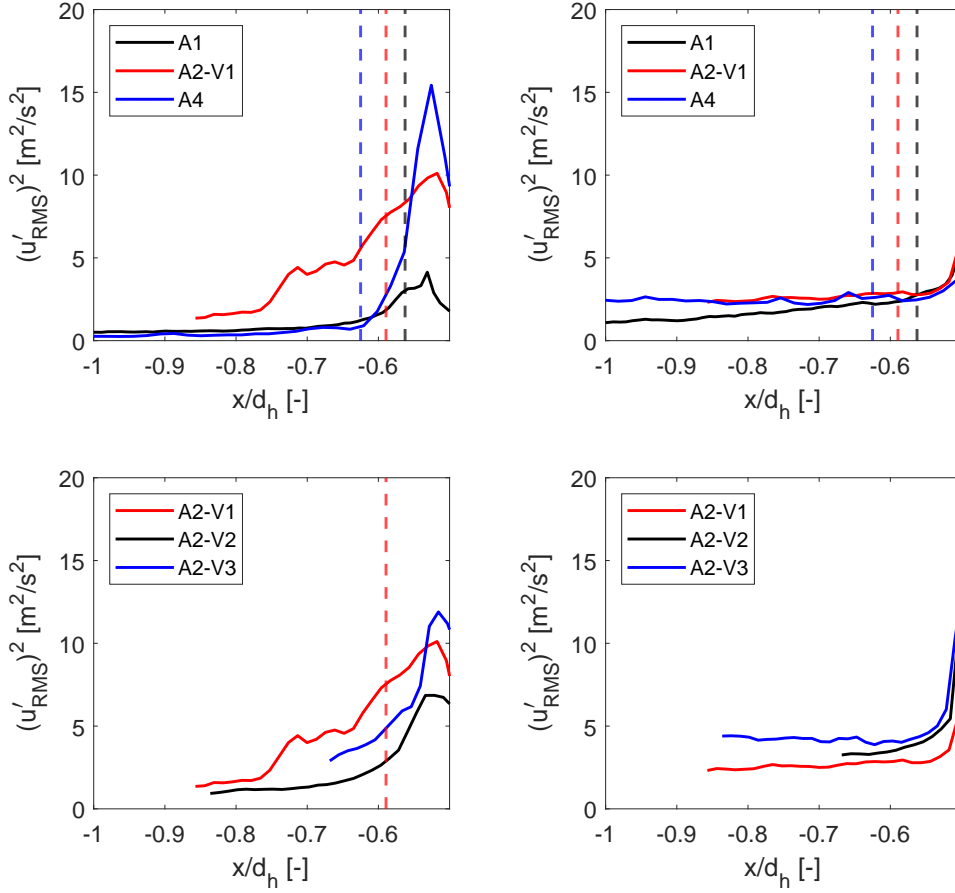


Figure 4.33: Squared-RMS of the normal velocity fluctuations at (top left)-(bottom left) 2 mm upstream, and (top right)-(bottom right) downstream for the tested orifice plates and a mass flow rate of 610 kg/h at the positions indicated in Figure 4.11. Vertical dashed lines correspond to the nondimensionalized ring's width.

A sharp exponential decrease is observed in the vicinity of the orifice's edge in all cases, confirming what was already experimentally observed by regarding the pressure fluctuations on the rim of the orifice [37]. At greater distances, the rms values decrease at a much slower pace and in a linear fashion. A difference between upstream and downstream behavior is that the maximum value upstream is attained somewhat after the orifice's edge, above the solid surface. This might be due to the presence of a vortex over the solid surface on the upstream side, as it can also be inferred from the vorticity field reported in Figure 4.32. The contrary is instead true downstream, where the maximum value seems to be located above the flow area of the orifice. Focusing on the differences between the plates, it can be appreciated how upstream the fluctuating velocity rms is sensitive both to the number of

holes and to their positions. In passing from the A1 to the A4 configuration and from the A2-V2 to the A2-V3 configuration, an increase in the peak rms value is observed; even though less dramatically so for the A2 plates. Also, both the A1 and the A4 plates here attain a linear decrease starting from distances from the orifice edge in the order of one tenth of the hole diameter d_h . The A2 plates instead attain a more or less linear decrease at larger distances, especially for the A2-V1 case (about 30% of the relative orifice's diameter). Downstream, results tend to better overlap once plotted against the non-dimensional distance from the orifice's edge. Focusing upstream, some considerations regarding the choice of the ring's width w in the 'modal efficiency coefficient' Ψ_{mn} defined in 3.3 can also be made. In fact, one could suggest that the area contributing the most to the integral in (3.24) for each orifice could be chosen by imposing the width over which the velocity fluctuation squared rms value is higher than a fixed ratio of the maximum reached. However, in doing so, the influence of the orifice's diameter d_h on the peak rms value would be lost (notice that for the same flow conditions the A4 plate shows a peak value three times that of the A1). In taking a constant width w , the two effects (larger widths for smaller peak values) might balance each other out, providing a good approximate tool for a first analysis of the plate geometry. For the sake of the present study, it was therefore chosen to employ a constant non-dimensional width ratio $w^* = w/t_p$ equal to 0.625 corresponding roughly to the width for which the squared velocity fluctuation rms of the A2-V1 plate attains a value of 60 % its maximum. A sensitivity analysis of such ring's width showed however that as long as it remained constant for all geometries, its value did not influence the overall qualitative agreement discussed.

4.4 Summary

This chapter dealt with the effect of the number/disposition of the orifices in a perforated plate on the excitation of higher-order acoustic modes in a rectangular duct subject to an incompressible air flow. A total of five different geometries were tested. The porosity ϕ of these plates was kept constant ($\phi = 0.25$) whereas the number, the position and the relative thicknesses of the orifices were changed. All plates can however be considered as 'thin', having a maximum $t^* = 0.2$.

A 2N-port analysis allowed the measurement of the emitted acoustic power as well as its modal composition in terms of the propagating higher-order acoustic modes in the frequency range $200 \text{ Hz} \leq f \leq 3200 \text{ Hz}$. An easily computable coefficient was proposed for a preliminary qualitative acoustic design of in-duct orifice plate geometries. Finally, a flow-visualization campaign through PIV was performed to study the flow structure in the

immediate vicinity of the obstacles.

It was found that the position and the number of orifices inside a rectangular orifice plate, maintaining a constant flow area and thickness, do not seem to influence to a great extent the caused pressure drop Δp_R . On the contrary, the emitted acoustic power and its modal composition resulted to be very sensitive to such parameters, particularly so for multi-modal propagation, highlighting their role in confined aerodynamic noise generation.

The capacity for a given orifice geometry to favor certain higher-order modes over others seems to be well captured by the proposed coefficient. This indirectly confirms previous literature regarding the concentration of the acoustic source in the immediate vicinity of the orifices' edges, as such coefficient is defined starting from such consideration. Furthermore, the velocity fluctuations normal to the plate's surfaces at 2 mm from it showed an exponential-like decrease in moving away from the orifice's edge, both upstream and downstream of it, confirming previous results by Tao et al. [37]. Upstream, the distribution of such velocity fluctuations is more dependent on the orifice configuration and its peak is somehow shifted outwards from the orifice's edge. Downstream, the distribution of the rms of the velocity fluctuation does not seem to be as influenced by the orifice's geometry as upstream and the peak is reached at the edge.

In the following Chapter 5, an attempt is made to observe the influence of the orifices' number and disposition on the broadband noise generated by a subsonic flow in a pipe.

Noise generation by subsonic flow through perforated plates in a pipe

This chapter deals with an investigation of broadband noise generation in pipes by subsonic flows through perforated plates performed at the Polytechnic University of Milan, Italy. The new experimental bench for fluid-dynamic and acoustic characterization of valves employed in the study is first described, together with its validation. Then, an in-depth analysis of the pressure fluctuations downstream of a thick multi-orifice plate ($t^* = 2$) is presented. Finally, the influence of the orifice disposition is investigated on plates with $t^* = 0.4$ and $t^* = 1$.

5.1 Experimental setup and methods

The experimental setup is a result of a collaboration between the valve manufacturing company Pibiviesse S.r.l. based in Nerviano (Italy) and the Polytechnic University of Milan and is currently located at the ‘G. Fantoli’ Hydraulics’ laboratory of the same university. It was partly designed during the Ph.D. thesis of Fenini [60] and it was set up during the present work. Its aim is twofold. First, to test noise emissions by industrial control valves subject to air flows according to the procedures and methods described in the international standard IEC-60534-8-1 [61]. Secondly, to obtain a more in-depth understanding of the underlying mechanisms of noise generation in a configuration which is closer to real-world applications (O&G sector). The work presented in the following paragraphs is related to the latter objective.

5.1.1 General characteristics

The experimental plant consists of an air treatment unit (compressor, particulate filter, dryer and storage tank), air-conveying piping, the test section, a globe control valve for mass flow-rate regulation and two external silencers

(Fig. 5.1). Air can be stored at up to 11 barA (absolute pressure) and a pilot-operated pressure regulator is installed at the tank's exit for obtaining steady-state inlet conditions. The mass flow-rate is measured through an in-line Coriolis mass flow-meter (Endress+Hauser Proline Promass F 300).

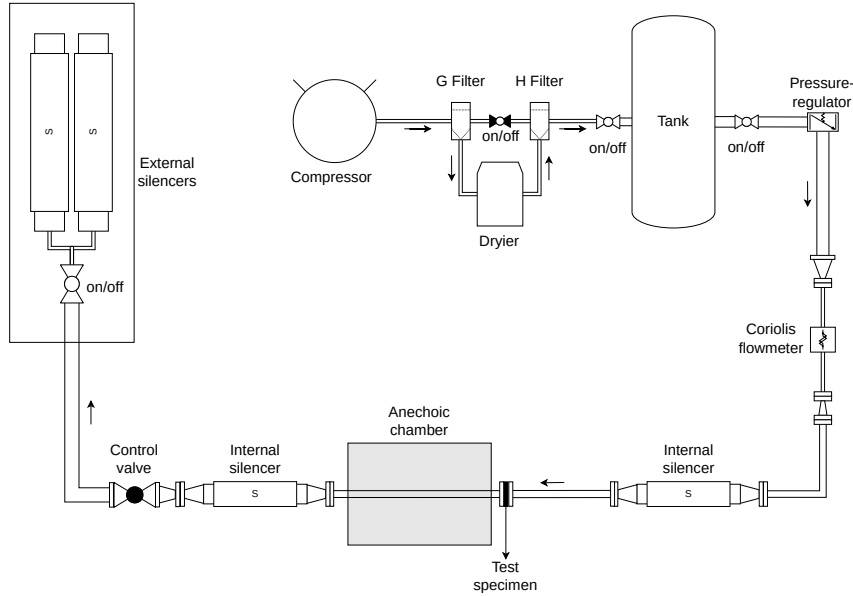


Figure 5.1: Schematic of the experimental test bench for subsonic airflows at the Polytechnic University of Milan.

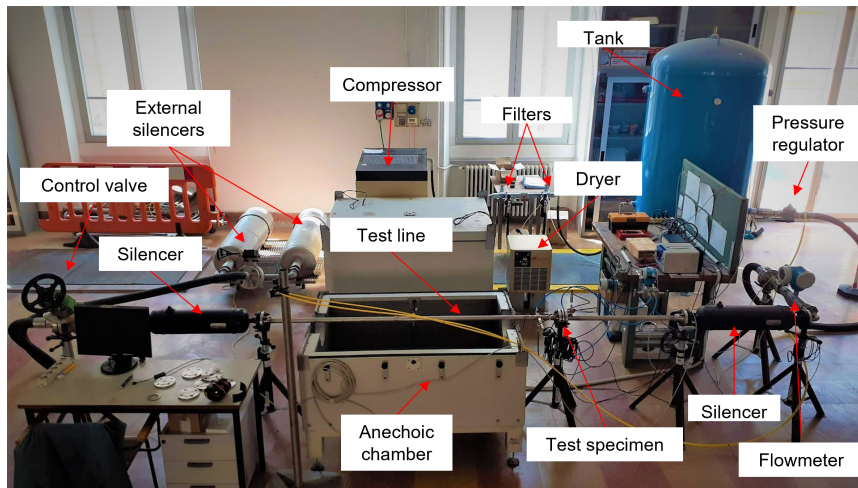


Figure 5.2: Overview of the experimental test bench for subsonic airflows at the Polytechnic University of Milan.

The test line (Figure 5.3) is composed of two W3 steel pipes of 25.4 mm

nominal diameter D_n pipes with thickness t_{pipe} of 9 mm (and an internal diameter $D_i = 24.3$ mm), flanged at both ends and simply supported. The upstream pipe has a length of 700 mm while the downstream one of 2000 mm. A flanged connection allows for the installation of the test specimens between the two pipes. Two in-line silencers (Maxim ILL-30) are placed at both ends of the test line to attenuate the effect of spurious noise coming from the upstream piping and the downstream control valve from frequencies $500 \text{ Hz} \leq f \leq 8 \text{ kHz}$. The static absolute pressure and the static temperature are measured through a pressure transducer (Endress + Hauser Cerabar M PMP51) and an RTD 100Ω probe respectively, at a section $2D_n$ upstream of the obstacle (section A-A' in Fig. 5.3) and at a section $6D_n$ downstream of it (section C-C' in Fig. 5.3) as specified by the standard IEC 60534-8-3 [61]. A differential pressure transducer (Endress + Hauser Deltabar S PMD75) is also installed between the same two sections. A summary of the main characteristics of the instruments used is reported in Table 5.1.

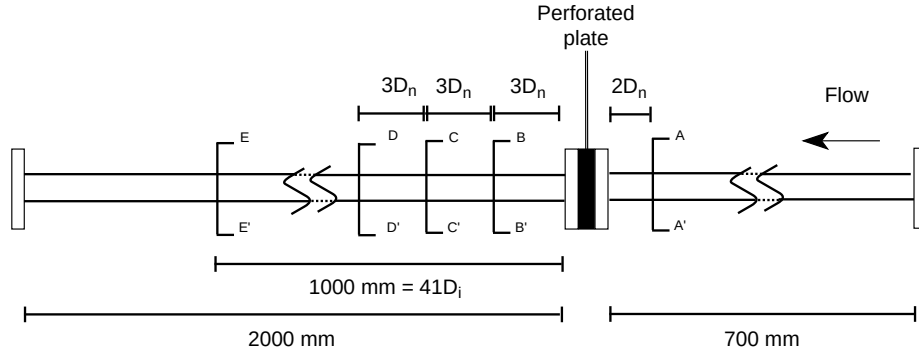


Figure 5.3: Schematic of the experimental test bench for subsonic airflows at the Polytechnic University of Milan.

Two 1/8 inches microphones (GRAS 47DX) can be installed flush with the inner pipe's wall for measuring the internal pressure fluctuations at sections B-B', C-C' and D-D'. In the present configuration, one microphone (GRAS1) is installed at section C-C' and another one (GRAS2) at section D-D', while the microphone's seat at section B-B' is sealed through a custom made plug. Three 1/4 inches piezo-electric pressure sensors (PCB Piezotronics 113B28) are installed in a recessed configuration 90° apart from each other at the same cross section E-E' (Figure 5.4). This last configuration is intended for a more in-depth analysis of the higher-order acoustic modes' pressure distribution along the pipe's cross-section.

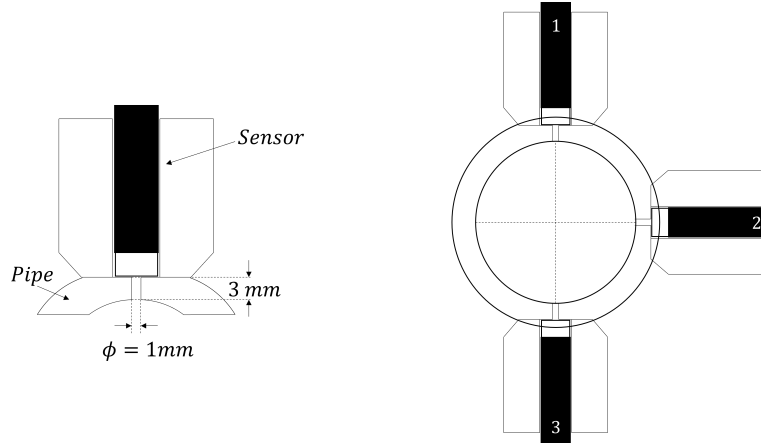


Figure 5.4: Schematic of installation for the piezoelectric pressure sensors at section E-E' and disposition along the cross section.

Finally, a ceramic shear accelerometer (PCB 352A60) is installed on an aluminum support which is glued at 1.1 m downstream of the test specimen. All vibro-acoustic sensors are connected to a signal conditioner (PCB 482C15) and acquired by two modules (National Instruments NI-9234) at 51.2 kHz. All fluid-dynamic quantities are instead acquired at 70 Hz by a different module (National Instruments NI-9208). An in-house developed LabView code is used to acquire the data collected by a chassis (National Instruments cDAQ 9184).

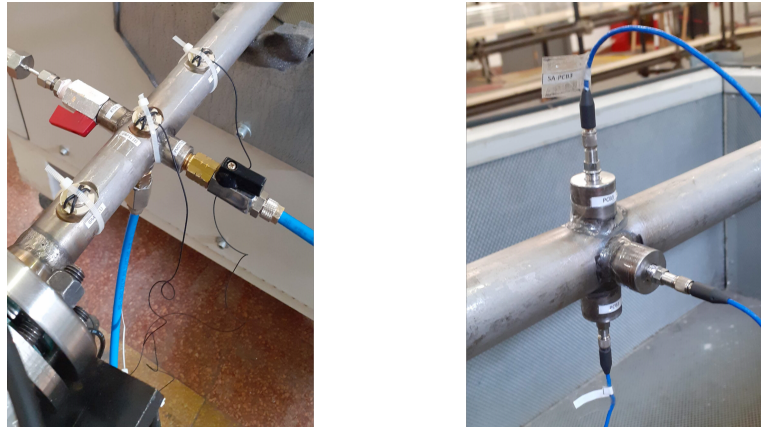


Figure 5.5: Sections B-B', C-C' and D-D' (left) and section E-E' (right).

Quantity	Instrument	Accuracy	Range
Mass flow rate	Endress+Hauser Proline Promass F 300	± 0.1 % of instantaneous value	0.004 kg/s to 0.15 kg/s
Absolute pressure at sec. A-A'	Endress + Hauser Cerabar M PMP51	± 0.01 bar	0 bar to 10 bar
Differential pressure sec. A-A' and C-C'	Endress + Hauser Deltabar S PMD75	± 0.0015 bar	-3 bar to + 3 bar
Static temperature sec. A-A' and C-C'	Metron RTD Pt100 (Class A)	± 0.12 °C	-10°C to 60°C

Table 5.1: Characteristics of the instruments employed for the measurement of fluid-dynamic quantities at the experimental plant in the Polytechnic University of Milan.

The frequency range of interest is set from 500 Hz to 20 kHz, the lower limit being imposed by the characteristics of the two internal silencers. Within this range, four higher-order acoustic modes are propagational. Their cut-on frequencies for the no-flow case and at ambient conditions can be computed through the non-dimensional values in Table 2.1 and are reported in Table 5.2.

Mode (m,n)	f_{co} [Hz]
(1,0)	8150
(2,0)	13720
(0,1)	17215
(3,0)	18880

Table 5.2: Cut-on frequencies of the higher-order modes in the frequency range $500 \text{ Hz} \leq f \leq 20 \text{ kHz}$ for test-line pipe ($D_i = 24.3 \text{ mm}$) and no flow at ambient conditions.

5.1.2 Plate geometries tested

A total of fifteen sharp-edged perforated plates with round orifices have been the subject of the investigation in this part of the work. The porosity ϕ of the plates was fixed at 0.16, while three relative thicknesses ($t^* = 0.4, 1, 2$) have been employed. Seven configurations of number/disposition of orifices for the relative thicknesses $t^* = 0.4$ and 1 were studied, while only one plate

with $t^* = 2$ was tested. Figure 5.6 together with Table 5.3 and Table 5.4 summarize the characteristics of the perforated plates object of this study.

The C4 plate is representative of the class of ‘thick’ perforated plates, for which the *vena contracta* is entirely contained within the bore of the perforation and no fluid-dynamic instabilities are known to occur (see 2.1.2). The plates with $t^* = 1$ (or ‘B’ plates), should also be considered as ‘thick’, even though close to the lower limit for such definition ($t^* = 0.75/0.8$). Plates with $t^* = 0.4$ (or ‘A’ plates) instead fall in the category of ‘transitional’ plates, for which the flow may reattach after the *vena contracta* and fluid-dynamic instabilities have been observed.

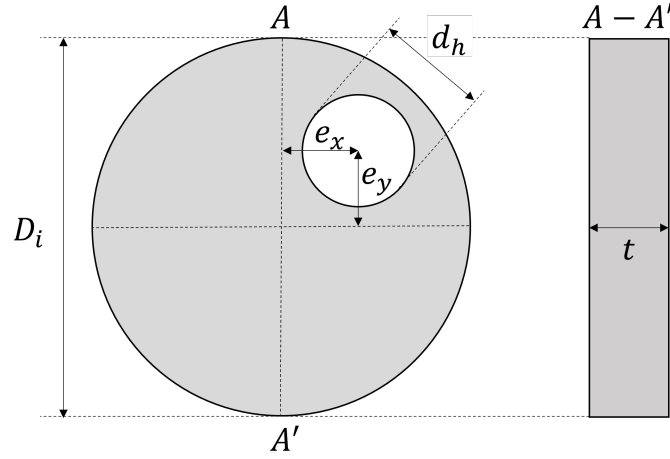


Figure 5.6: Scheme for identification of the characteristics of the perforated plate geometries in Table 5.3 and Table 5.4.

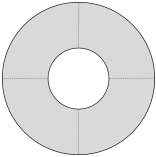
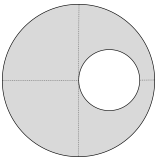
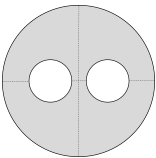
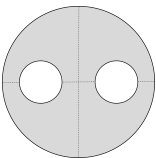
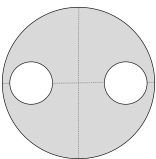
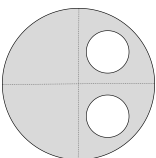
Geometry	Plate ID	e_x [mm]	e_y [mm]	t/d_h
	A1-V1	0	0	0.4
	B1-V1	0	0	1
	A1-V2	4.86	0	0.4
	B1-V2	4.86	0	1
	A2-V1	4.5	0	0.4
	B2-V1	4.5	0	1
	A2-V2	6	0	0.4
	B2-V2	6	0	1
	A2-V3	7.5	0	0.4
	B2-V3	7.5	0	1
	A2-V4	4.85	5	0.4
	B2-V4	4.85	5	1

Table 5.3: Geometry, plate ID, position of the first orifice starting clockwise from point A to point A' of Figure 5.6 and relative thickness of the one-holed and two-holed plates. Symmetry for the other perforations as indicated in the relative schemes.

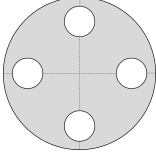
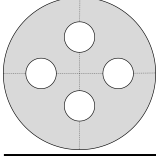
Geometry	Plate ID	e_x [mm]	e_y [mm]	t/d_h
	A4	0	8.15	0.4
	B4	0	8.15	1
	C4	0	5.15	2

Table 5.4: Geometry, plate ID, position of the first orifice starting clockwise from point A to point A' of Figure 5.6 and relative thickness of the four-holed plates. Symmetry for the other perforations as indicated in the relative figures.

5.2 Validation of the experimental setup

A preliminary characterization of the newly-mounted experimental setup was performed. The aim was to obtain a reference condition for the effects of the perforated plates as well as to check the correct functioning of the overall installation.

5.2.1 Background noise

Due to the sensitive nature of the vibro-acoustic measurements, it is important to quantify the background noise present in all recordings. Such noise may be due to installation effects of the sensors or to their faulty functioning. The PSD of the background noise of the fluctuating pressure sensors (GRAS1-2 and PCB1-2-3) and of the accelerometer (A60) averaged over 400 iterations with a 100 Hz frequency resolution are reported in Figure 5.7. Regarding the pressure sensors, it is clear that the piezoelectric ones (PCB1-2-3) show a higher impact of the background noise when compared to the condenser ones (GRAS1-2) due to the lower nominal sensitivity (0.0145 mV/Pa) compared to the latter (0.8 mV/Pa). A general increase of the noise with increasing frequencies is also seen. As the shape of the spectra is the same for all sensors, it is reasonable to assume that such noise is electrical in nature.

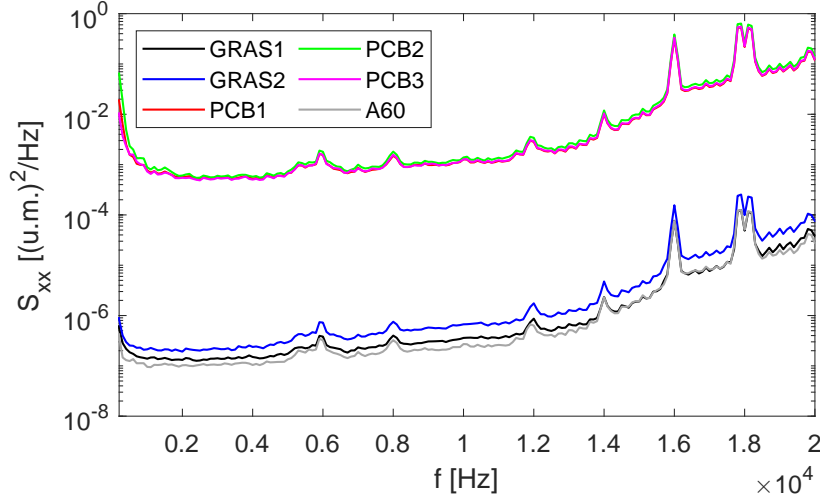


Figure 5.7: Background noise PSD of vibro-acoustic sensors in the relative dimensional units in the range 500 Hz to 20 kHz with a frequency resolution of 100 Hz.

A useful indication of the quality of a vibro-acoustic measurement is the ‘signal to noise ratio’ (SNR), defined as the ratio of the PSD of a measured quantity \hat{S}_{xx} and that of the background noise \hat{N}_{xx} . Usually, the SNR is reported in logarithmic form:

$$\text{SNR} = 10 \log_{10} \left(\hat{S}_{xx} \right) - 10 \log_{10} \left(\hat{N}_{xx} \right) \quad (5.1)$$

A value of SNR of 20 dB/Hz or more is considered good, as it corresponds to an absolute ratio between the amplitude of the signal and the background noise of at least 100. On the contrary, values of SNR under 10 dB/Hz indicate that the amplitude of the measured quantity is of the same order of magnitude of the background noise and hence cannot be considered for analysis.

5.2.2 Wall pressure fluctuations in empty pipe

By removing the perforated plates, a condition close to that of a simple straight pipe of constant cross section is obtained. For such condition and for fully turbulent flow (as is always the case in the present work), interpolating formulas for the wall pressure fluctuations spectra \hat{S}_{pp} are available in the literature [62]. Such spectra are usually scaled through the non-dimensional formulation [7]:

$$\hat{S}_{pp}^* = \frac{\hat{S}_{pp} U}{q^2 R_i} \quad (5.2)$$

with $q = 1/2\rho U^2$ the dynamic pressure of the average flow and $R_i = D_i/2$. On his study on the pipe wall vibrations caused by turbulent boundary layers in pipes, Durant [63] proposed an expression for \hat{S}_{pp}^* as a function of global quantities of the flow (inner radius of the pipe R_i and average pipe velocity U):

$$\log_{10}(\hat{S}_{pp}^*) = -5.1 - 0.9 \log_{10}\left(\frac{f R_i}{U}\right) - 0.34 \left[\log_{10}\left(\frac{f R_i}{U}\right) \right]^2 - 0.04 \left[0.9 \log_{10}\left(\frac{f R_i}{U}\right) \right]^3 \quad (5.3)$$

To compare the spectra obtained experimentally with that of (5.3) it is however necessary to consider two factors:

- the acoustic component of the measured \hat{S}_{pp} ;
- the spatial averaging caused by the finite size of the pressure transducer.

The first issue can be tackled through the Coherent Output Power (COP) method described in [50] and applied in [63]. Defining the magnitude-squared coherence $\hat{\gamma}_{s_1, s_2}$ between two signals s_1 and s_2 as:

$$\hat{\gamma}_{s_1, s_2}^2 = \frac{|\hat{S}_{s_1, s_2}|^2}{\hat{S}_{s_1, s_1} \hat{S}_{s_2, s_2}} \quad (5.4)$$

The part of the spectra \hat{S}_{s_2, s_2} which is uncorrelated with \hat{S}_{s_1, s_1} is given by:

$$\hat{S}_{s_2, s_2}^{\text{uncr.}} = \hat{S}_{s_2, s_2} (1 - \hat{\gamma}_{s_1, s_2}^2) \quad (5.5)$$

In the case under consideration, if s_1 is the fluctuating pressure measured by one of the sensors and s_2 is the same quantity measured at a distance sufficiently large for the turbulent fluctuations to be uncorrelated, then $\hat{S}_{s_2, s_2}^{\text{uncr.}}$ coincides with $\hat{S}_{p, p}^{\text{turb.}}$.

The second issue is related to the fact that the effect of turbulent structures smaller than the sensor's area is spatially averaged due to the limited spatial resolution [62]. Corcos [64] computed an attenuation curve $\hat{C} = \hat{S}_{pp}^{\text{msrd}} / \hat{S}_{pp}^{\text{true}}$ of the measured turbulent wall pressure spectra $\hat{S}_{pp}^{\text{msrd}}$ for the case of fully turbulent flow over a flat plate. He reported the correction values in tabular form as a function of the non-dimensional radian frequency $\omega r_s / U_c$ where r_s is the radius of a circular pressure sensor mounted flush with the plate surface and U_c is the 'eddy convection velocity'. An interpolating curve of such attenuation is reported in Figure 5.8.

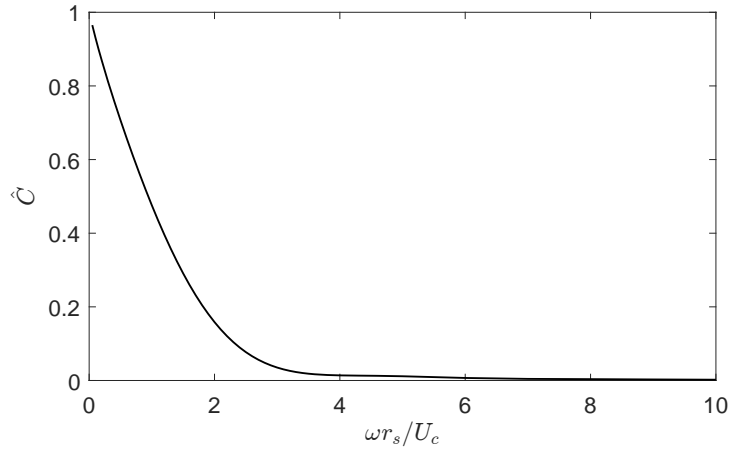


Figure 5.8: Interpolating curve for tabular values of the attenuation \hat{C} of the measured wall pressure spectrum $\hat{S}_{pp}^{\text{msrd}}$ of a turbulent boundary layer relative to the ‘true’ value $\hat{S}_{pp}^{\text{true}}$ if no spatial averaging were present. Adapted from Corcos [64].

Regarding the convection velocity U_c , literature studies suggest that its value relative to the average velocity U is in the range $0.6 \leq U_c/U \leq 0.8$ while citing the structural response of the sensor’s diaphragms the radius r_s is usually substituted by an ‘equivalent radius’ $r_e = 0.6 \cdot r_s$ [63]. Also, the validity of the attenuation curve of Fig. 5.8 has been confirmed up to values of $\omega r/U_c < 3.5 - 4$, while experimental evidence of its validity is weaker for larger values, e.g. [62, 65].

Flush-mounted condenser microphones

The magnitude-square coherence $\hat{\gamma}_{s_1, s_2}^2$ between the two flush-mounted condenser microphones at sections C-C’ and D-D’ for an average flow velocity U of 17 m/s ($M = 0.049$) is reported in Figure 5.9. Except for very low frequencies ($f \leq 700$ Hz) and up to roughly 14 kHz, $\hat{\gamma}_{s_1, s_2}^2$ is close to zero, indicating that the two measured signals are not coherent with each other. The higher peak at low frequencies is explained by the fact that larger turbulence structures are coherent over larger distances. The sharp increase for higher frequencies may instead be linked to the background noise common to the two instruments. This observation is also confirmed by the SNR of the instruments for the same test (Figure 5.10). Starting from roughly 14 kHz the SNR decreases under 10 dB/Hz, indicating a signal dominated by the sensors’ self-noise.

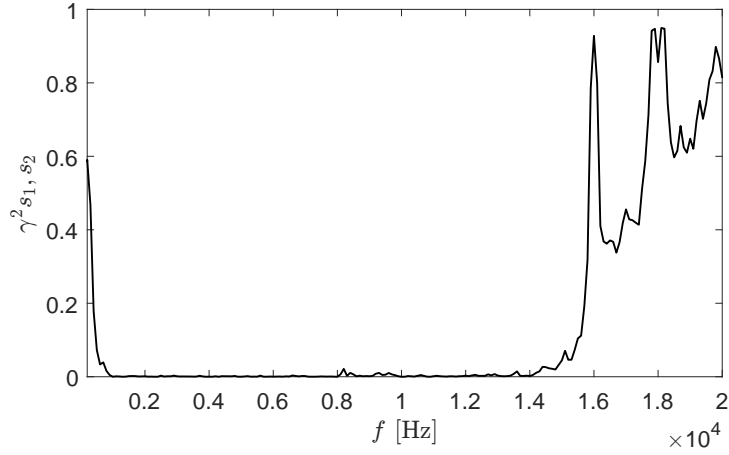


Figure 5.9: Magnitude-squared coherence $\hat{\gamma}_{s_1, s_2}^2$ between the two flush-mounted condenser microphones at sections C-C' and D-D' of Figure 5.3 for a pipe flow with average Mach number $M = 0.049$. Frequency resolution of 100 Hz.

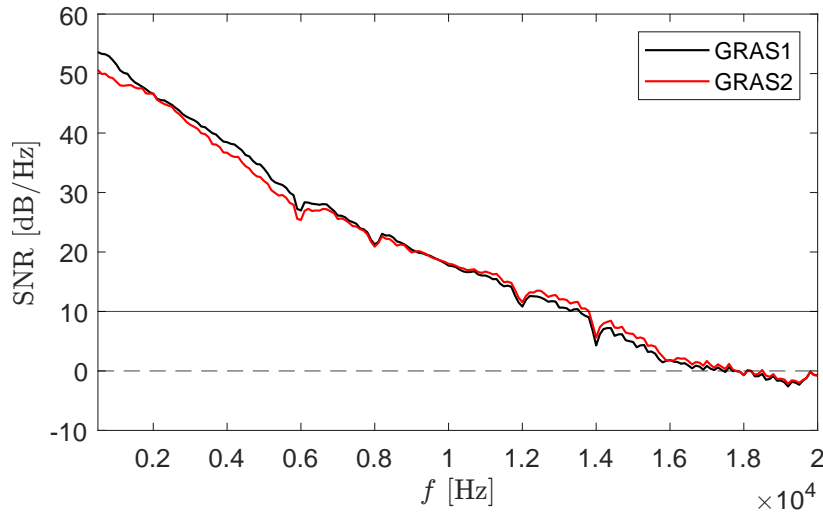


Figure 5.10: Signal-to-noise ratio (SNR) of the two flush-mounted condenser microphones at sections C-C' (GRAS1) and D-D' (GRAS2) of Fig. 5.3 for a pipe flow with average Mach number $M = 0.049$. Frequency resolution of 100 Hz.

The non-dimensional PSDs of the wall pressure at section C-C' for average duct Mach numbers M from 0.048 to 0.074 are reported in Figure 5.11 together with the experimental curve of (5.3). It can be seen that a very good collapse of the curves is obtained if the frequency is non-dimensionalized as the Strouhal number. The correction of the 'original' PSD through the

attenuation curve of Figure 5.8 is applied by imposing a maximum $St = 3.5$ and choosing $U_c/U = 0.8$. It can be seen that if the area-averaging effects of the sensor are accounted for, the measured \hat{S}_{pp} is in good qualitative agreement with the experimental fit obtained by Durant [63]. The mismatch in amplitude might instead be due to the fact that section C-C' is positioned at $9D_i$ from the flanged connection between the two pipes composing the test sections. This may introduce a disturbance of the boundary layer which might explain the overall shift in amplitude of the measured quantity when compared to the interpolating expression (5.3).

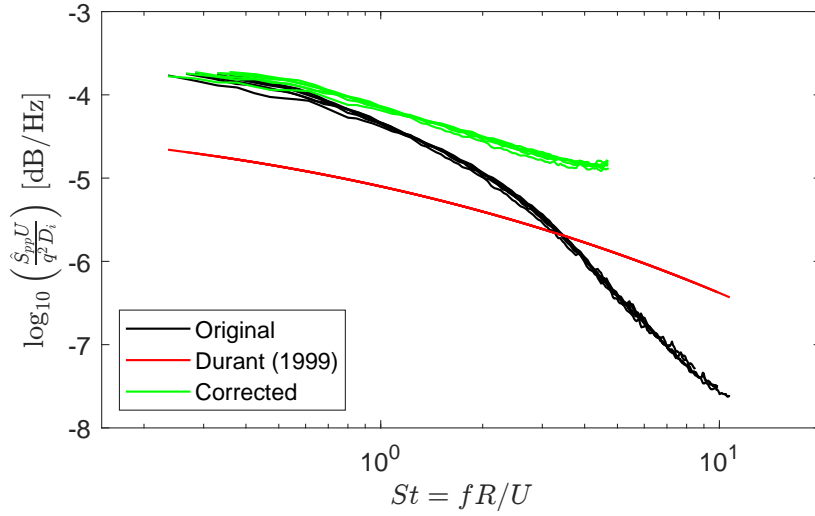


Figure 5.11: Non-dimensional PSD of the wall pressure fluctuations at section C-C' for pipe flow with Mach numbers from 0.049 to 0.074.

Recessed piezo-electric pressure sensors

In the original configuration of the experimental test bench, the piezo-electric pressure sensors PCB 113B28 at section E-E' were mounted flush with the inner pipe's wall at sections B-B', C-C' and E-E' [60]. To maximize the use of the available instrumentation, during the course of this thesis it was chosen to modify the installation by mounting the three sensors in a single section as described in 5.1.1. This in fact allows for a more in-depth analysis of the internal fluctuating pressure field, which at this distance from the perforated plate should be dominated by the acoustic component generated by the obstacle [41]. In particular, the position of the three microphones 90° apart along the same cross-section allows to identify the presence of the first azimuthal higher order modes (see 5.3).

In order to limit the effect of their large diaphragm size (1/4 inches) relative to the internal pipe diameter (≈ 1 inches), their configuration was

changed from flush to recessed. Such a configuration however modifies the basic FRF of the system, as the presence of a cavity connected through a neck to the inner pipe can be viewed as an example of a Helmholtz' resonator (Figure 5.12). The behavior of such system can as a first approximation be considered equivalent to a mass-spring system [26]. In fact, the volume of air contained within the neck can be seen to 'vibrate' as a mass which is connected to a cavity which reacts by either increasing or decreasing the pressure if the mass of air in the neck either moves downward or outward. The resonant frequency of the system f_r can be computed as:

$$f_r = \frac{c}{2\pi} \sqrt{\frac{A_n}{V_c l_n}} \quad (5.6)$$

where $A_n = \pi d_n^2/4$ is the area of the cross-section of the neck. If the cavity volume V_c is of the same order of magnitude of the volume of the neck $V_n = A_n l_n$, the resulting system can be approximated by the neck only. Hence, the resonant frequency is that of a simple pipe open at one end [66]:

$$f_r = \frac{c}{4l_n} \quad (5.7)$$

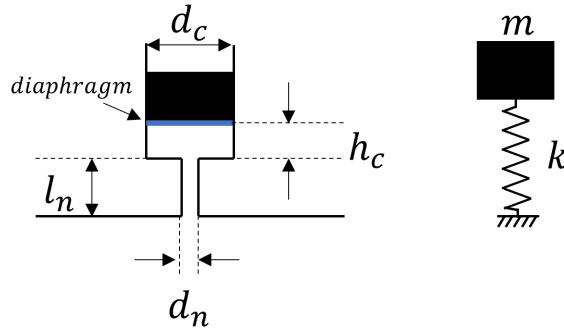


Figure 5.12: Schematic of the cylindrical Helmholtz' resonator resulting from the recessed installation of the fluctuating pressure sensor. Equivalent mass-spring system on the right.

For the case of the piezo-electric pressure sensors employed in this thesis, the installation suggested by the manufacturer is reported in Figure 5.13 while the sensor's dimensions are reported in Figure 5.14. It can be seen that the use of the cylindrical seal of 6.1 mm in length leaves a clearance h_c between the sensor's diaphragm and the neck of 0.13 mm. As for the dimensions of the neck's length ('A' or l_n) and diameter ('B' or d_n), no specific values are indicated. In the present work, a conservative value of the diameter $B = d_n = 1$ mm and a length $A = l_n = 3$ mm were chosen, resulting in a volume ratio of $V_n/V_c \approx 0.85$. Thus, (5.7) should be employed

for the computation of the resonant frequency f_r , which is found to be 25.2 kHz.

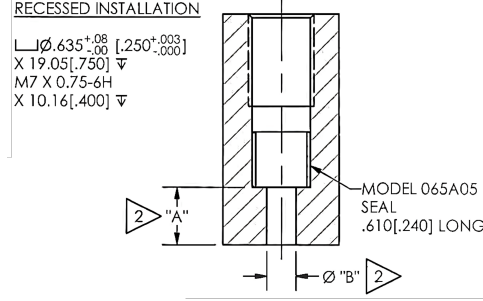


Figure 5.13: Installation requirements for recessed configuration of piezo-electric pressure sensor PCB 113B28 as indicated by the manufacturer. Dimensions outside of square brackets are in centimeters.

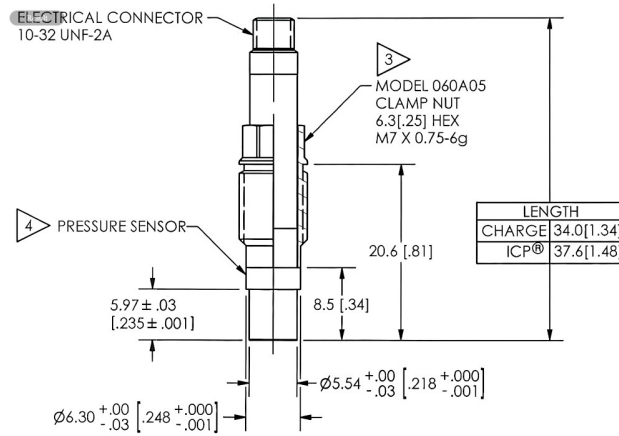


Figure 5.14: Piezoelectric sensor PCB 113B28 dimensions as provided by the manufacturer. Dimensions outside of square brackets are in millimeters.

The magnitude-squared coherence $\hat{\gamma}_{s_1, s_2}^2$ between the sensor couples are reported in Figure 5.15. It can be here seen that the coherence is larger at lower frequencies than in the case of the condenser microphones while after a steep decrease it remains approximately zero until roughly 8 kHz. From such threshold onward, the coherence steadily and equally increases for all sensor couples. The first observation is again explained by the fact that turbulence is correlated for slowly-evolving structures at low frequencies. The second observation can also again be explained by the presence of background (electrical) noise.

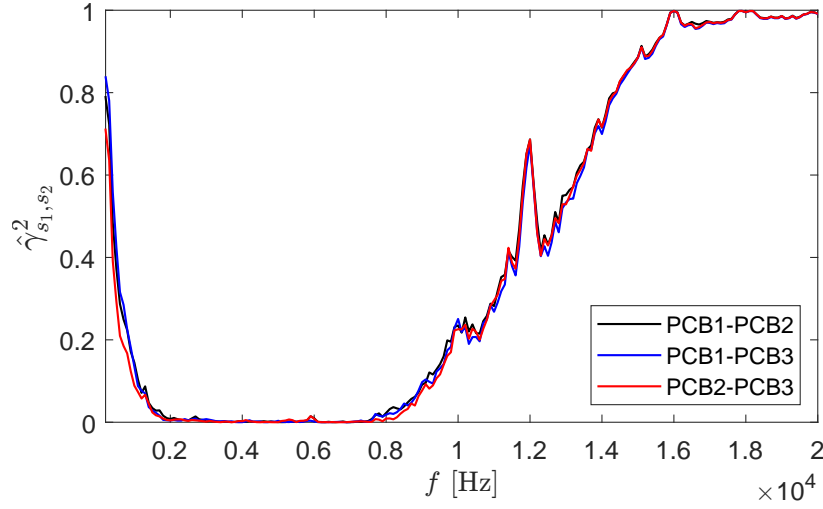


Figure 5.15: Magnitude-square coherence $\hat{\gamma}_{s_1, s_2}^2$ between the piezo-electric sensors PCB1-PCB2, PCB2-PCB3 and PCB1-PCB3 at section E-E' of Figure 5.3 for a pipe flow with average Mach number $M = 0.049$. Frequency resolution of 100 Hz.

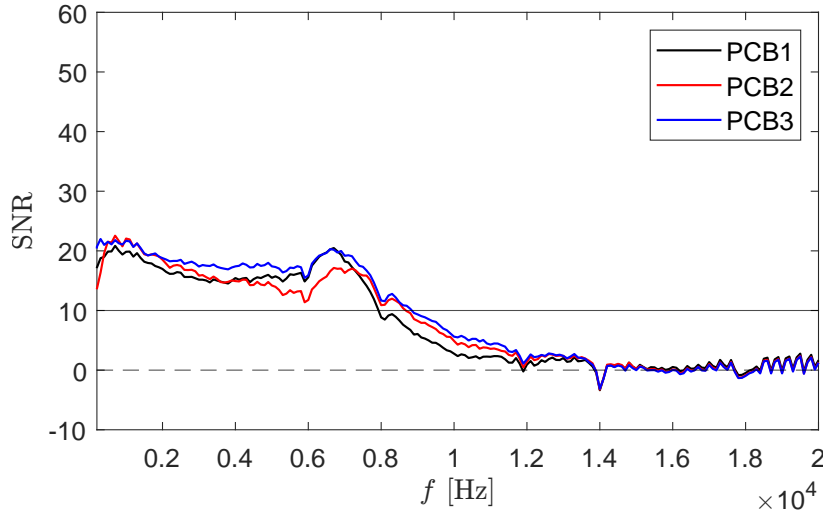


Figure 5.16: piezo-electric sensors PCB1, PCB2 and PCB3 at section E-E' of Figure 5.3 for a pipe flow with average Mach number $M = 0.049$. Frequency resolution of 100 Hz.

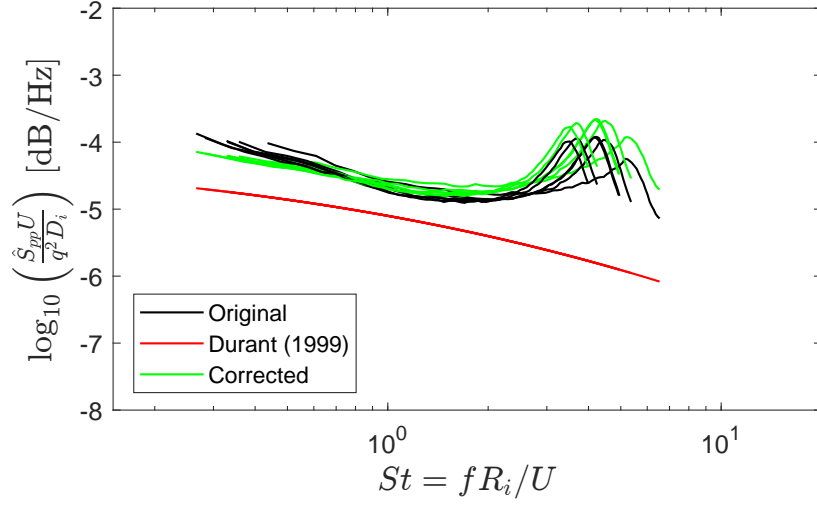


Figure 5.17: Non-dimensional PSD of the wall pressure fluctuations at section E-E' as recovered by the sensor PCB1 for empty pipe configuration and Mach numbers from 0.048 to 0.074.

The non-dimensional spectra of the sensor PCB1 for the same tests of Figure 5.11 are reported in Figure 5.17 for the frequency range 500 Hz to 7.5 kHz (in non-dimensional form) to avoid considering the part of the signal dominated by background noise (see Figure 5.16). A good collapse of the spectra is present for lower frequencies and the ‘corrected’ one closely follows the interpolating curve of Durant [63]. Broad peaks are however observed at higher frequencies. Such peaks are correctly collapsed in terms of amplitudes by the non-dimensionalisation of (5.2). However, plotting against the Strouhal number produces a ‘shifting’ of the curves, suggesting a phenomenon which is not linked to the flow velocity in terms of its frequency. This is confirmed if the ‘corrected’ spectrum is plotted against the dimensional frequency (Figure 5.18) where the peaks superpose at around 6400 Hz.

Such a result can be explained if the clearance between the sensor’s diaphragm and the neck is increased by 0.5 mm. In such a case, the ratio V_n/V_c would decrease to ≈ 0.17 and the resonant frequency of the system should be computed through (5.6), yielding $f_r = 6458$ Hz.

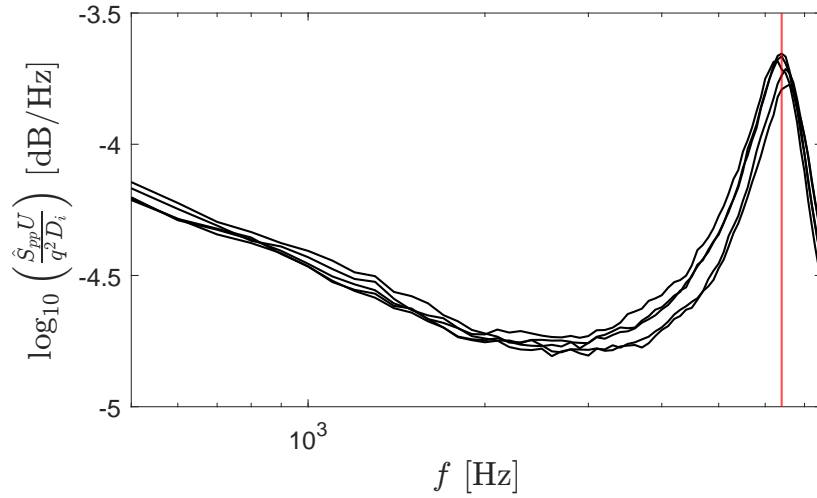


Figure 5.18: Non-dimensional PSD of the wall pressure fluctuations at section E-E' as recovered by the sensor PCB1 for empty pipe configuration and Mach numbers from 0.048 to 0.074 with no frequency scaling.

Concluding remarks

The previous discussion has highlighted the fact that the experimental setup allows for the correct measurement of the wall pressure fluctuations at least for the sections C-C' and D-D', where flush-mounted condenser microphones are employed. Some issues were instead encountered with the recessed piezoelectric sensors at section E-E', where an error in the installation is the most probable cause of a peak in the PSD of the wall pressure fluctuations. However, in the present work, the sensors are employed nonetheless by referencing each measured signal to that obtained by the other two. While obtaining only 'relative' information on the phenomenon studied, this way of proceeding provides useful hints for its better understanding, as shown in 5.3.1. Further confirmation for this use can also be found in Appendix B, where an attempt at a calibration of the recessed sensors through an external source is reported.

5.3 Results

A detailed analysis of the results of an experimental campaign on the 'thick' perforated plate geometry C4 is first provided. Then, a more general discussion on the results obtained for the 'A' and 'B' geometries follows. This subdivision arises from the fact that the C4 plate is the only one for which no whistling was recorded for any of the tested conditions. This allows to better investigate the role of the acoustic higher-order modes in broadband-only noise generation by subsonic flows.

5.3.1 Thick multi-orifice perforated plate

The C4 plate was tested by imposing a constant upstream pressure at section A-A' of 2.5 barA while gradually opening the downstream globe valve. A total recording time of 20 s was considered sufficient to obtain steady-state conditions.

Fluid-dynamic behavior

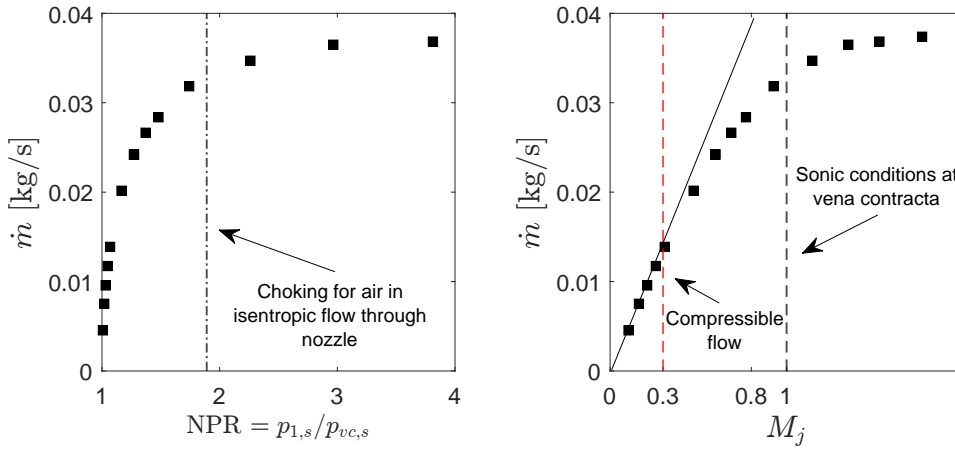


Figure 5.19: Mass flow rate \dot{m} versus Nozzle Pressure Ratio (NPR) (left) and versus the jet Mach number M_j (right) for ‘thick’ plate C4 with fixed upstream pressure of 2.5 barA.

The mass flow rate \dot{m} against the Nozzle Pressure Ratio (NPR) and the jet Mach number M_j are shown in Figure 5.19. The *vena contracta* pressure has been computed employing the concept of ‘liquid pressure recovery factor’ F_L discussed in Chapter 2; its measurement is reported in Appendix A. Choking is reached for values slightly higher than the theoretical limit for air of 1.89 (2.1.4), confirming the fact that the ‘thick’ geometry does not allow for important enlargements of the *vena contracta* (see also Figure 5.32). Nonetheless, its expansion is visible through the increase of \dot{m} even after sonic conditions are reached at such section. The deviation of the linearity between \dot{m} and M_j due to the increasing importance of compressibility from $M_j = 0.3$ is also observable. The same effect is also the cause for the deviation of the resistance coefficient K_L from its constant value in Figure 5.20. The discharge coefficient C_d (2.1.3) is also reported for NPR lower than 1.8 in Figure 5.21. Due to the limited expansion of the *vena contracta*, C_d is not too sensitive on the value of NPR, an observation which is in accordance with previous literature on the subject [67].

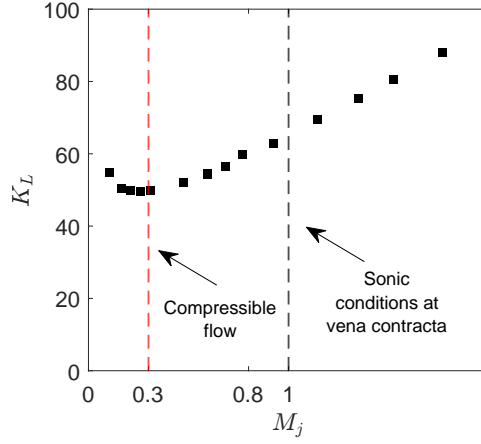


Figure 5.20: Resistance coefficient K_L against the jet Mach number M_j of plate C4 for the tested conditions.

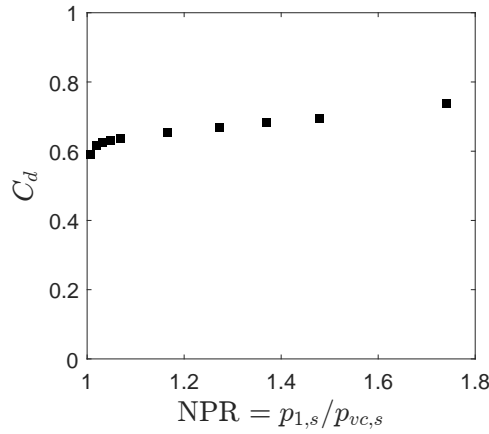


Figure 5.21: Discharge coefficient of plate C4 for incompressible and subsonic flow.

Pipe wall pressure fluctuations

The PSD of the pipe wall pressure fluctuations \hat{S}_{pp} at sections C-C' and D-D' for $M_j \approx 0.75$ are reported in Figure 5.22. For reference, the same quantity for the section D-D' for the empty pipe with equal average upstream Mach number ($\text{Ma} \approx 0.06$) is reported together with the two previous quantities in Figure 5.23. Peaks at the theoretical cut-on frequencies are clearly discernible, indicating the important contribution of acoustic pressure fluctuations to \hat{S}_{pp} . The difference in magnitude between the 'empty pipe' configuration and the one with the plate is also apparent from Figure 5.23, especially so for increasing frequencies, for which the 'no obstacle' case displays a sharp decrease in magnitude until reaching levels of background

noise (the two peaks at roughly 16 kHz and 18 kHz coincide with those of Figure 5.7).

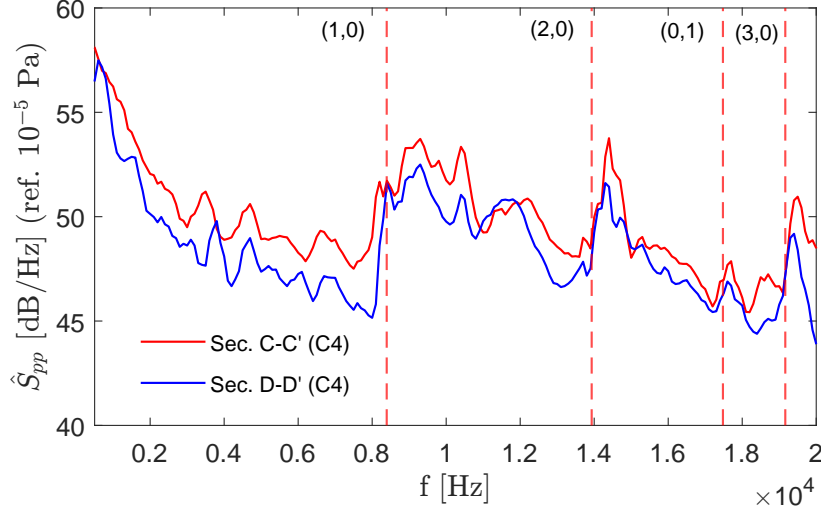


Figure 5.22: PSD of pipe wall pressure fluctuations at sections C-C' and D-D' for $M_j \approx 0.75$ for C4 plate. Cut-on frequencies of higher-order modes are included as dashed red lines. Bandwidth 100 Hz.

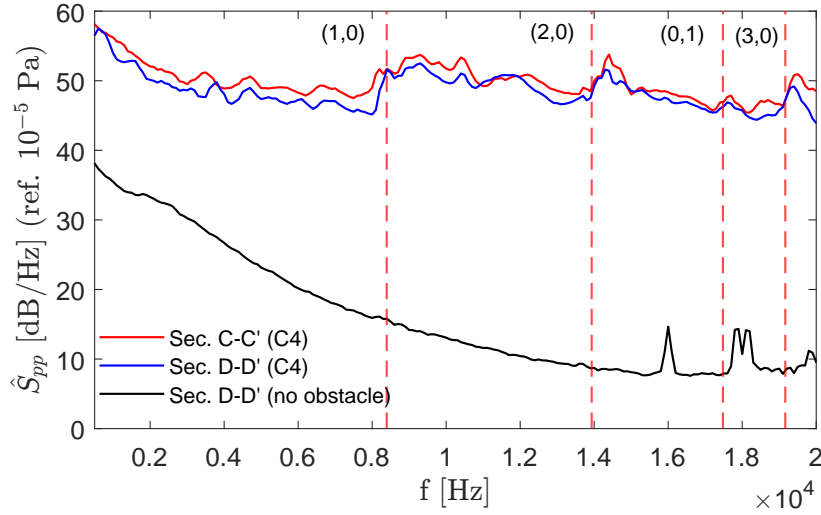


Figure 5.23: PSD of wall pipe pressure fluctuations at sections C-C' and D-D' for $M_j \approx 0.75$ for C4 plate and same quantity for equivalent flow through empty pipe (same average duct Mach numbers $Ma \approx 0.06$). Cut-on frequencies of higher-order modes are reported as dashed red lines. Bandwidth 100 Hz.

Some insights on the type of acoustic source produced by the flow through

the perforated plate can be obtained by computing the power law exponent α for the acoustic power law $W_a \propto M_j^\alpha$ (see also 4.3.2). As discussed in Chapter 2, to compute W_a for the whole frequency range of interest (500 Hz, 20 kHz) the modal composition in terms of the propagating higher-order modes would be needed. However, such operation is not possible with the current experimental set-up. Hence, the analysis is limited to the frequency range where only plane waves are propagating, i.e. from 500 Hz to 8 kHz. The acoustic power in this case can be computed through [7]:

$$W_a = \frac{p_{rms}^2 A}{\rho_0 c_0} \quad (5.8)$$

where p_{rms} is the root mean square of the pressure fluctuations. In order to account only for the frequencies within the range (500 Hz, 8 kHz), such quantity can be computed from \hat{S}_{pp} as [68]:

$$p_{rms} = \sqrt{\sum_{\bar{f}=f_1}^{f_2} \hat{S}_{pp}(\bar{f}) \Delta \bar{f}} \quad (5.9)$$

where f_1 and f_2 are two center frequencies of bandwidth $\Delta \bar{f}$. The resulting trend of W_a against M_j for $0.2 < M_j < 1$ is reported in Figure 5.24. A good linearity is obtained if both W_a and M_j are expressed in logarithmic form, indicating the presence of a power law of the type $W_a \propto M_j^\alpha$. A ‘best fit’ line for the available points results in an exponent $\alpha \approx 3$.

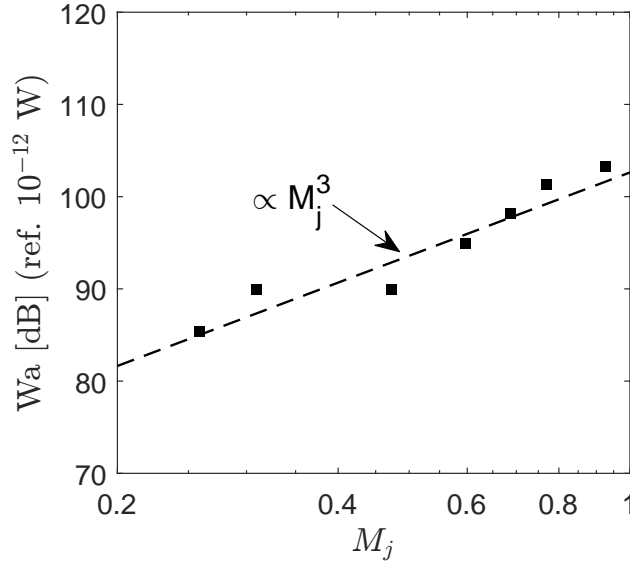


Figure 5.24: Total emitted acoustic power W_a against jet Mach number M_j for the plane wave-only frequency range $500 \text{ Hz} \leq f \leq 8 \text{ kHz}$ for the ‘thick’ perforated plate C4.

According to the review of the theory in Chapter 3 and considering the results in Chapter 4, this result comes unexpected. An acoustic source showing a dipole-like behavior would in fact translate into a dependence with $\alpha \propto 4$ while a quadrupole-like behavior would instead translate to $\alpha \propto 6$. However, the relative close positioning of the microphone to the obstacle ($9D_i$) might have played a role. Previous literature ([69]) suggests that already at distances of roughly 10 pipe diameters from a thin orifice plate in subsonic flows the pressure fluctuations are mainly of acoustic type. However, such a statement could be very much dependent on the specific geometry of the tested device and in the case under consideration hydrodynamic pressure fluctuations could be partly the cause for the result obtained.

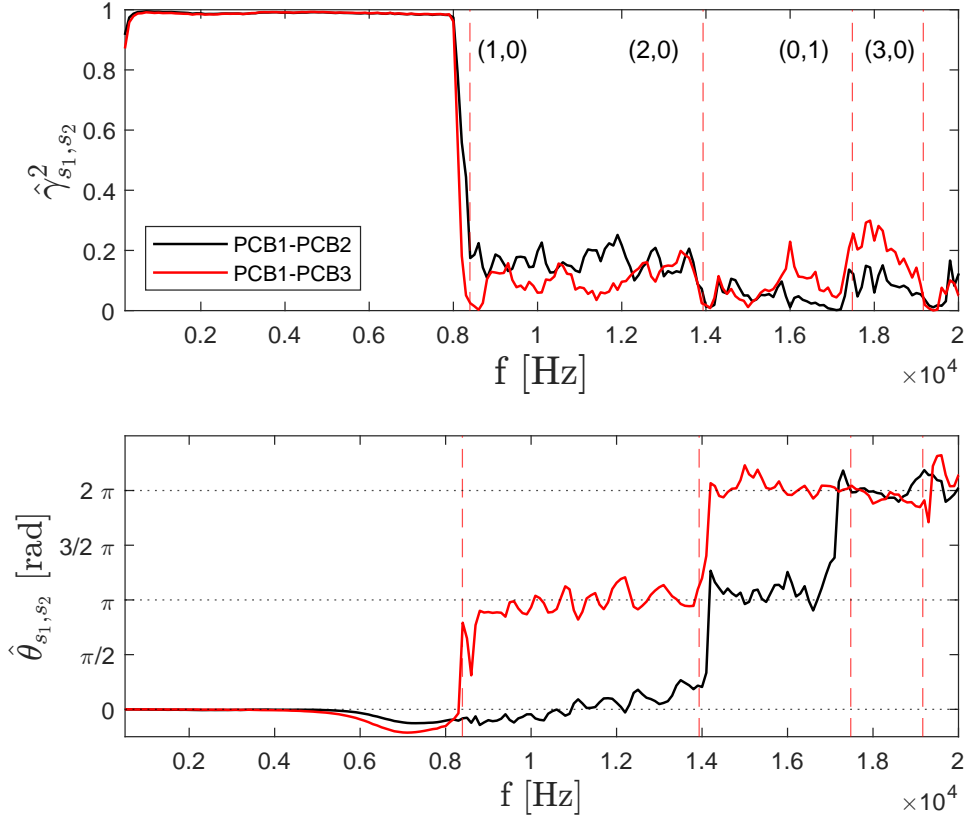


Figure 5.25: Magnitude-squared coherence $\hat{\gamma}_{s_1, s_2}^2$ and relative phase $\hat{\theta}_{s_1, s_2}$ between sensor pairs at section E-E' for $M_j \approx 0.75$ and C4 plate. Cut-on frequencies are indicated as dashed red lines. Bandwidth 100 Hz.

Regarding the presence of higher-order modes, the analysis of the magnitude-squared coherence $\hat{\gamma}_{s_1, s_2}^2$ and the phase differences $\hat{\theta}_{s_1, s_2}$ between the signals recorded by the sensors at section E-E' can be useful (Figure 5.25). For the same test conditions as above, the magnitude-squared coherence is al-

most exactly 1 in the plane wave frequency range while it abruptly drops to values lower than 0.3 as soon as the first cut-on mode (1,0) becomes propagational. This leads to some interesting observations. Firstly, the almost unitary value of $\hat{\gamma}_{s1,s2}^2$ suggests that the pipe wall pressure fluctuations at this section are dominated by the acoustic component. As it was shown in 5.2.2, in the absence of an obstacle, turbulence is correlated over very short distances and at lower frequencies. The sudden drop in $\hat{\gamma}_{s1,s2}^2$ at the cut-on frequency of the first higher order mode also confirms the acoustic cause for such high value of coherence. The same drop may instead suggest that the acoustic pressure field is now composed of a multi-modal distribution which shows low levels of intermodal correlation between the cut-on modes. This last observation is in agreement with results from the literature [40, 69].

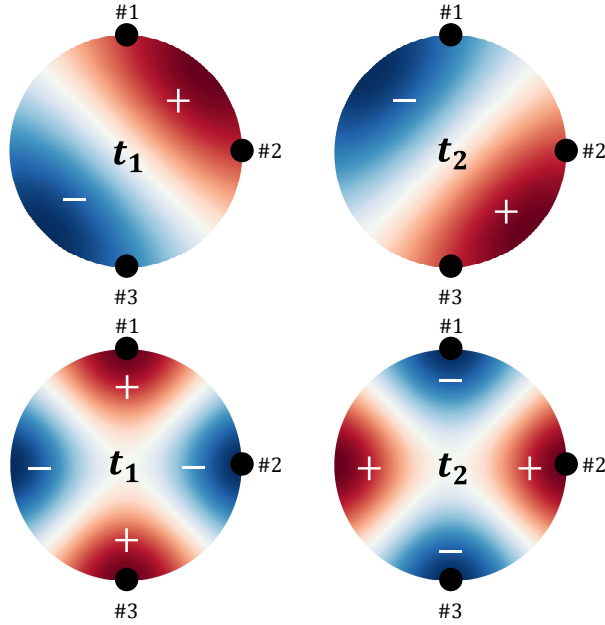


Figure 5.26: Acoustic pressure distribution of mode (1,0) (top) and mode (2,0) (bottom) at two time instants t_1 and t_2 for section E-E'.

These remarks can also be confirmed if the relative phase $\hat{\theta}_{s1,s2}$ between the sensors is considered. The sensors are perfectly in phase ($\hat{\theta}_{s1,s2} = 0$) up until roughly 6 kHz, where the resonance due to the faulty installation discussed in 5.2.2 influences the behavior of the instruments. As the first higher-order mode becomes propagational however, differences between the sensor couples arise. By referring to Figure 5.26 and focusing on the frequency range for which the (1,0) mode is the only higher-order mode propagational, were the acoustic field mostly characterized by such acoustic pressure distribution, any phase difference between two sensors 90° apart (1-2 in the present

case) should be $\pi/2$: the maximum amplitude of the pressure fluctuation at one microphone would be reached when the other is subject to a zero pressure disturbance. Contrarily, two sensors 180° apart (1-3 in this case) would always be out of phase, i.e. $\hat{\theta}_{s_1, s_2} = \pi$. Considering instead an acoustic field where the main propagating mode were the (2,0) one, the two sensors 180° apart would always be in phase and those 90° apart out of phase. The results presented in the bottom plot of Figure 5.25 only partly agree with the qualitative reasoning above. In fact, the sensor pair 1-2 shows that for the frequency range where only the mode (1,0) is propagational the phase difference measured between the two sensors is roughly zero, in contrast to the expected $\pi/2$ shift. This might indicate the presence of a standing wave in the azimuthal direction. In fact, recalling (2.36) and assuming that the amplitudes $C_{\pm 10}$ of the clockwise ($m = 1$) and anticlockwise ($m = -1$) spinning modes are the same, then the pressure fluctuations relative to such mode ‘degenerate’ to:

$$p'_{a,10}(r, \theta, x_3) = 2C_{10}N_{10}J_{10}(k_{r,10}r) \cos(\theta) e^{-i(\omega t - k_{10}x_3)} \quad (5.10)$$

Referring to Fig.5.27, it can be seen that depending on the position assumed by the axial nodal line, the sensor pair 1-2 can either be in phase or π out of phase while the sensor pair 1-3 will always be π out of phase.

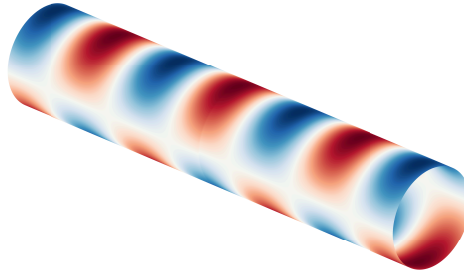


Figure 5.27: Colour plot of the distribution of pressure fluctuations for a standing azimuthal mode (1,0) along the walls of a pipe. Propagation of the wave is from left to right.

It can be also noticed that the cut-on of the radial mode (0,1) does not cause a localized phase shift as could be expected by a field dominated by such mode.

Pipe wall acceleration

To conclude the analysis of the noise produced by the ‘thick’ orifice plate C4, the SNR as defined in (5.1) of the pipe’s wall acceleration for the same test conditions is reported in Figure 5.28. For reference, the same quantity for the

empty pipe with equivalent average downstream Mach number ($M \approx 0.06$) is reported too. It can be seen here that the two signals superpose with each other up until roughly 4 kHz with values of SNR above 10 dB/Hz. After such threshold, the ‘empty pipe’ configuration shows very low values of SNR, indicating a very poor signal quality. If the obstacle is present instead, two distinct localized increases of SNR arise in the vicinity of the cut-on frequencies of the two azimuthal modes (1,0) and (2,0). A plot of the magnitude-squared coherence $\hat{\gamma}_{s1,s2}^2$ between each sensor at section E-E’ and the accelerometer is reported in Figure 5.29. While the overall level is generally low, the increase of such value at the cut-on of the first higher-order mode is clearly discernible.

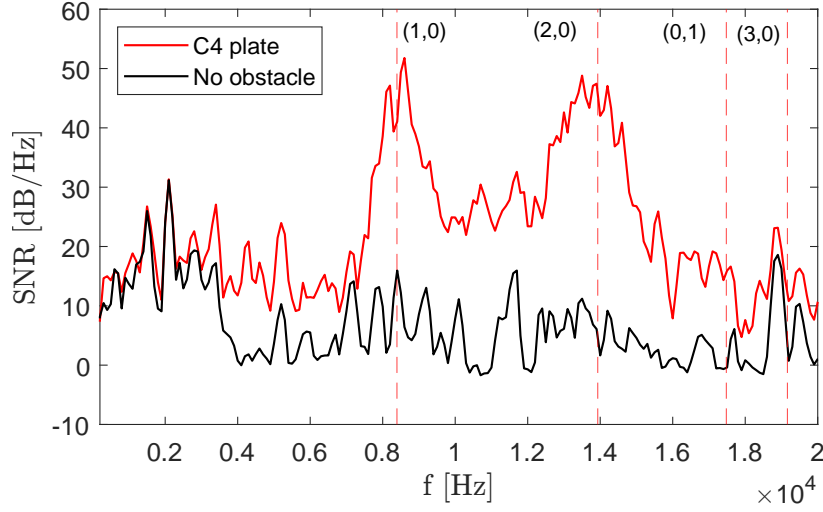


Figure 5.28: Signal-to-noise ratio (SNR) for accelerometer positioned $\approx 45D_i$ downstream of perforated plate both in the presence of the C4 plate and in the empty duct configuration. Cut-on frequencies are indicated as dashed red lines. Bandwidth 100 Hz.

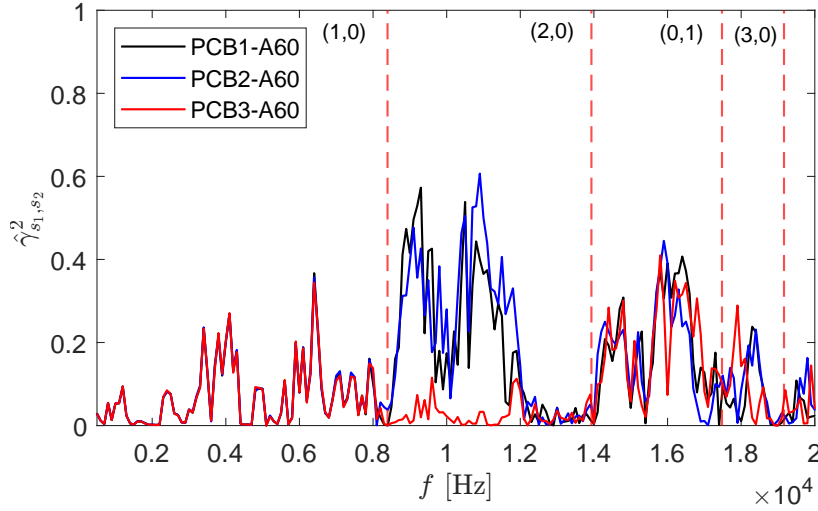


Figure 5.29: Magnitude-squared coherence $\hat{\gamma}_{s_1, s_2}^2$ between each sensor at section E-E' and the accelerometer positioned $\approx 45D_i$ downstream of perforated plate. Cut-on frequencies are indicated as dashed red lines. Bandwidth 100 Hz.

5.3.2 Effect of relative thickness, orifice number and disposition

All of the seven configurations for the two relative thicknesses $t^* = 0.4, 1$ have been tested by imposing an upstream static pressure $p_{1,s} = 2$ barA and gradually opening the downstream globe control valve. The total recording time is again set to 20 s for both fluid-dynamic and vibro-acoustic quantities. As stated above, all geometries showed the presence of whistling at the tested operating conditions. While this is an interesting finding *per se*, such phenomenon is beyond the main subject of investigation of the thesis (broadband noise generation). A general description of the obtained results is nonetheless provided for reference and some comments related to the role of higher order modes with whistling are made.

Fluid-dynamic behavior

A preliminary experimental campaign on the 'Control Valve' water loop was performed, as in the case of the C4 plate, in order to obtain the 'liquid pressure recovery factor' F_L . However, the fluid-dynamic instabilities arising in the case of the 'A' geometries prevented its correct computation for such cases (see Appendix A for more details). As the knowledge of F_L is necessary for the estimation of both the NPR and M_j (Chapter 2), it was decided here to report the results in terms of the relative pressure drop $x = \Delta p_R / p_{1,s}$, a parameter most commonly used by the valve engineering

community and defined in the international standard IEC 60534-8-3 [61]. The non-dimensional mass flow rate \dot{m}^* versus \sqrt{x} is reported for all the tested geometries for the two relative thicknesses $t^* = 0.4, 1$ in Figure 5.30. The trend of the resistance coefficient K_L versus \sqrt{x} for the same tests is also reported in Figure 5.31. It can be seen that the relative thickness t^* is the principal quantity affecting the fluid-dynamic behavior of the perforated plate, with the thinner ‘A’ plates opposing the greatest resistance to the flow. Furthermore, the same plates display a more irregular pattern which is particularly visible in the trend of K_L versus \sqrt{x} shown in Figure 5.31. This behavior was not dependent on whether the tests were performed by either opening or closing the globe control valve, as superposition of the points was obtained in the two cases.

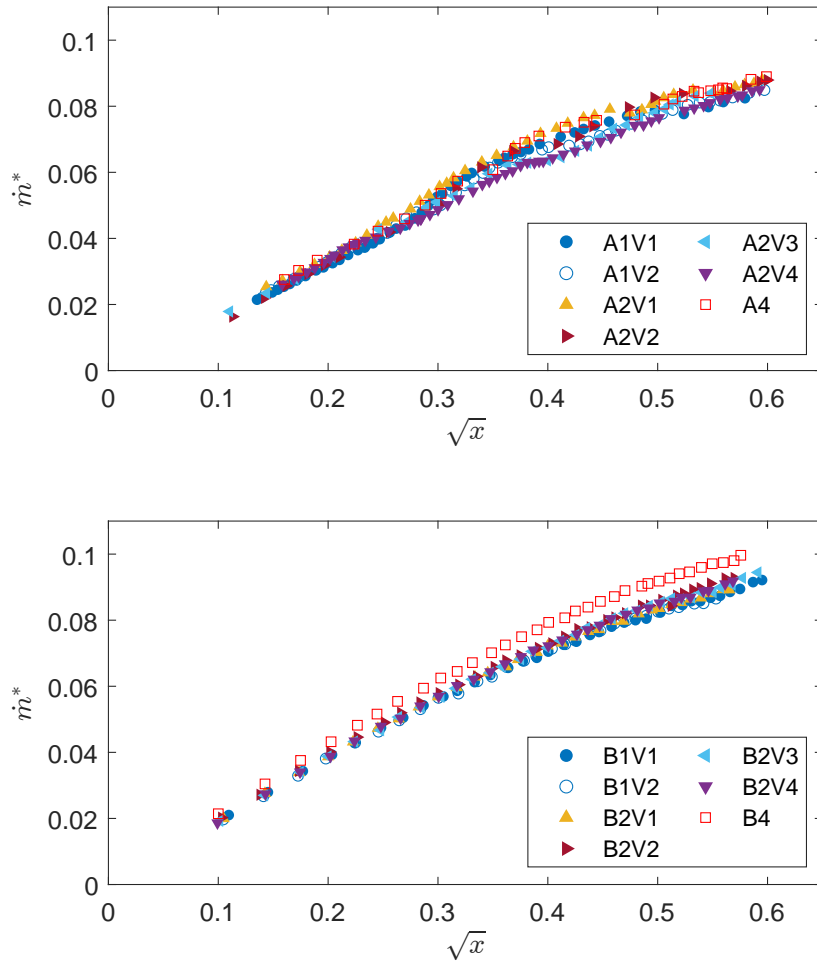


Figure 5.30: Non-dimensional mass flow rate \dot{m}^* versus squared root of the relative pressure drop (\sqrt{x}) for all tested geometries at the two relative thicknesses $t^* = 0.4$ (top) and $t^* = 1$ (bottom).

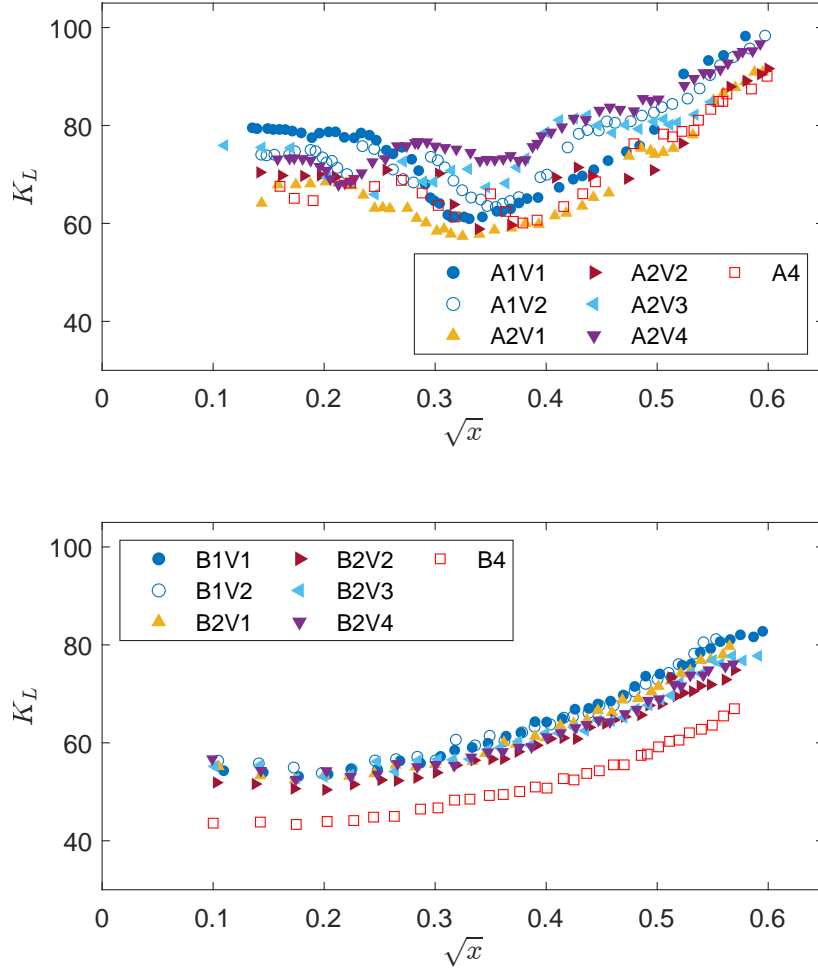


Figure 5.31: Resistance coefficient (K_L) versus squared root of the relative pressure drop (\sqrt{x}) for all tested geometries for the two relative thicknesses $t^* = 0.4$ (top) and $t^* = 1$ (bottom).

The abrupt changes in K_L can be explained by the following reasoning. From its definition of (2.3), a constant value of K_L indicates that the ratio $\Delta p_R / \rho_1 U_1^2$ is constant. As the upstream density ρ_1 is held approximately constant during the tests, the sudden drops of K_L must be due to the fact that the increase in pressure drop Δp_R does not ‘balance’ the increase of U_1^2 . In other words, the pressure drop caused by the device is lower than what would be expected if a constant K_L were present, i.e. the device dissipates less energy. Such a change could be linked to a reattachment of the flow to the inner walls of the orifice bore due to the expansion and retreat of the *vena contracta* for compressible flows discussed in 2.1.4. A qualitative drawing of this mechanism is reported in Figure 5.32. As explained in 2.1.2, this in fact causes a lower exit velocity from the orifice and therefore lower

pressure losses due to mixing.

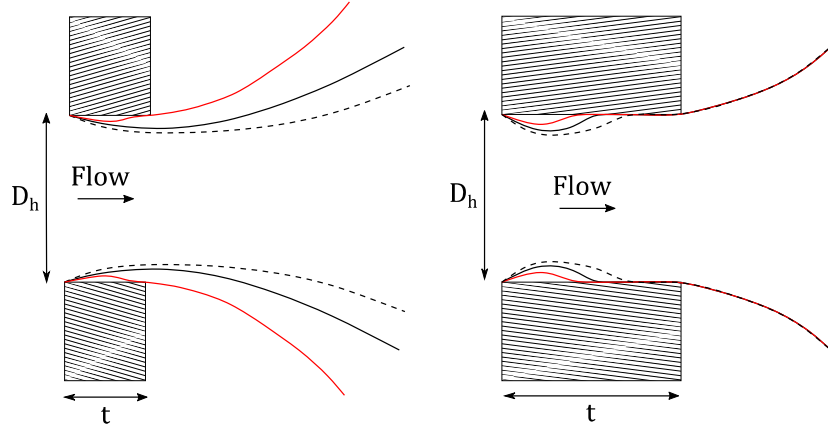


Figure 5.32: Mechanism of reattachment of the flow due to the expansion of the *vena contracta* for increasing jet Mach numbers. On the left, a ‘transitional’ plate, on the right a ‘thick’ plate.

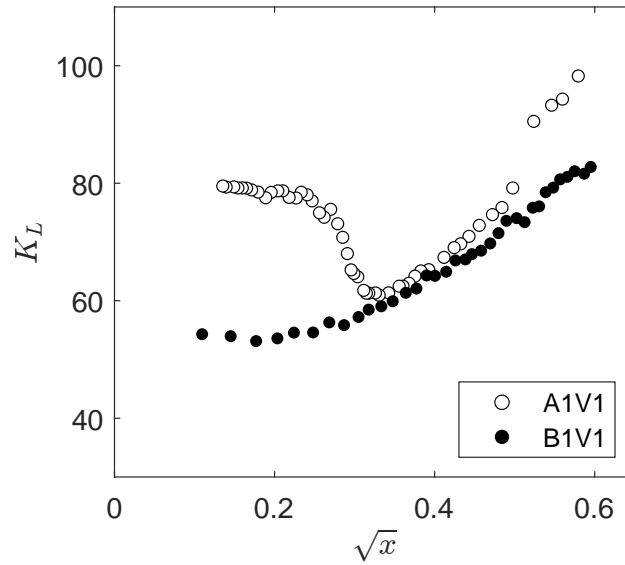


Figure 5.33: Resistance coefficient K_L against the squared root of the relative pressure drop \sqrt{x} of plates A1-V1 and B1-V1.

Such an interpretation is particularly convincing if the trend of the resistance coefficient K_L of the two single-hole A1-V1 and B1-V1 plates are compared (Figure 5.33). After an initial approximately constant value of K_L for the two cases, it can be seen that the trend for the A1-V1 plate drops dramatically until practically superposing with the one of the B1-V1 plate. As

this last geometry can be considered as ‘thick’ due to its relative thickness $t^* > 0.8$, the fact that the A1-V1 plate approaches its trend may indicate a similar ‘flow geometry’ with the flow occupying the whole cross section of the bore. The same behavior is not seen for the other geometries, where however either the asymmetry of the orifice position (A1-V2, B1-V2) or the presence of multiple jets (all remaining geometries) may affect its onset.

Pipe wall pressure fluctuations

The colour maps of the non-dimensional \hat{S}_{pp}^* at section D-D’ for increasing values of \sqrt{x} for both the ‘A’ and the ‘B’ plates are reported in Figures 5.34 and 5.35. The C4 plate’s map is also reported for reference. The relative thickness t^* is the most important parameter in determining the acoustic behavior of the perforated plates, with the thinner plates ‘A’ responsible for the highest noise generation. This same parameter also seems to be linked to the presence of whistling, visible in the maps as a concentration of energy within very thin bandwidths. In general, the phenomenon is pronounced for the ‘A’ plates, it is still present for the ‘B’ ones and it is completely absent for the C4 geometry. In this respect, the orifices’ disposition has a non negligible effect. In fact, the two-holed symmetric configurations (A/B2-V1, V2, V3) display this phenomenon to a lower degree, especially so for the ‘A’ geometries. Asymmetry on the other hand (A/B1-V2 and A/B2-V4) tends to exacerbate whistling. The number of orifices also particularly influences the onset of whistling for the thicker ‘B’ plates, as is the case for the single-holed geometries (B1-V1 and B1-V2), while for the four-holed B4 geometry this is limited to lower values of \sqrt{x} .

An interesting observation can be made if the resistance coefficient K_L is reported together with the previous colour maps. This is here done in Figure 5.36 for the symmetric single-holed geometries A1-V1 and B1-V1. Clearly, a change in the frequency of whistling is accompanied by a change in the resistance coefficient, especially so for the case of the transitional ‘A’ geometry. While no attempts to model this behavior are here made, it can be supposed that the change in the internal ‘flow geometry’ due to the possible reattachment of the flow within the perforation induces a modification on the whistling mechanism too.

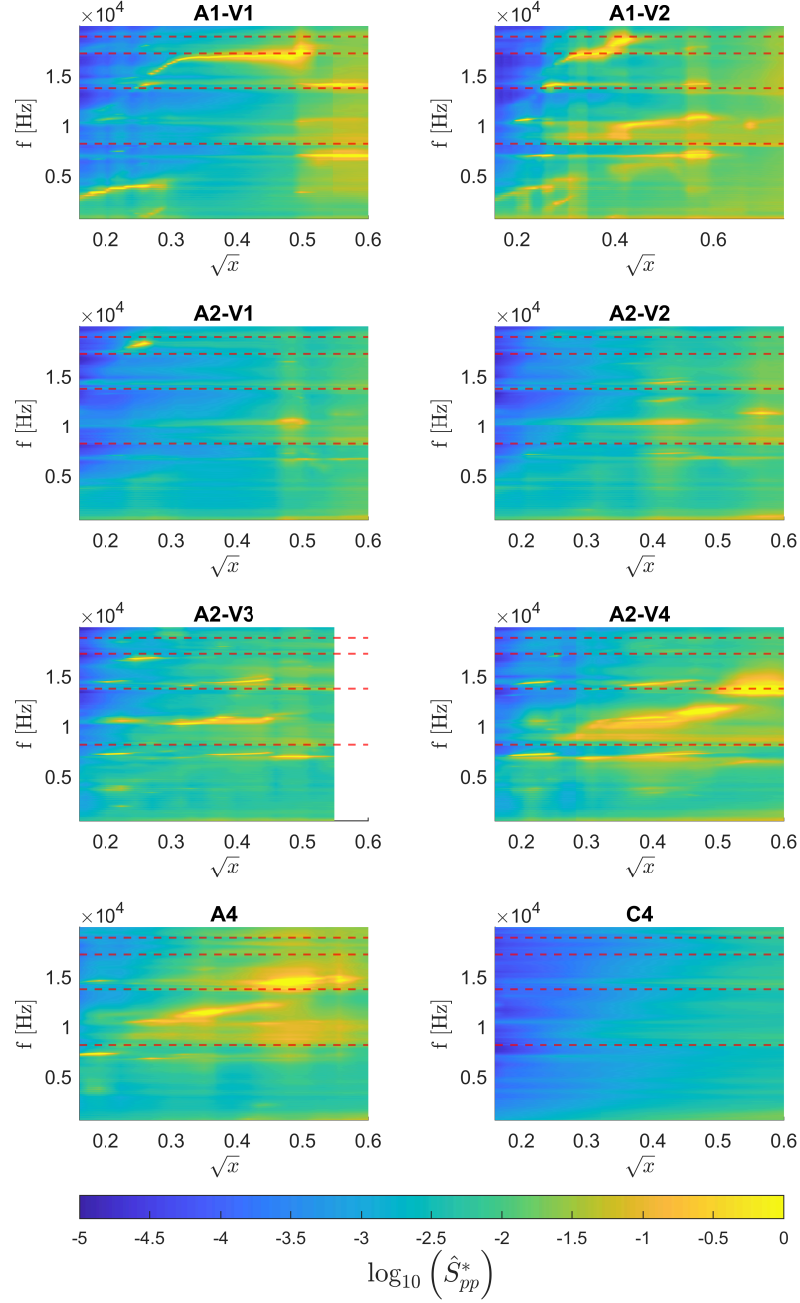


Figure 5.34: Color map of the non-dimensional PSD \hat{S}_{pp} at section D-D' for increasing squared root of the relative pressure drop \sqrt{x} for 'A' plates ($t^* = 0.4$).

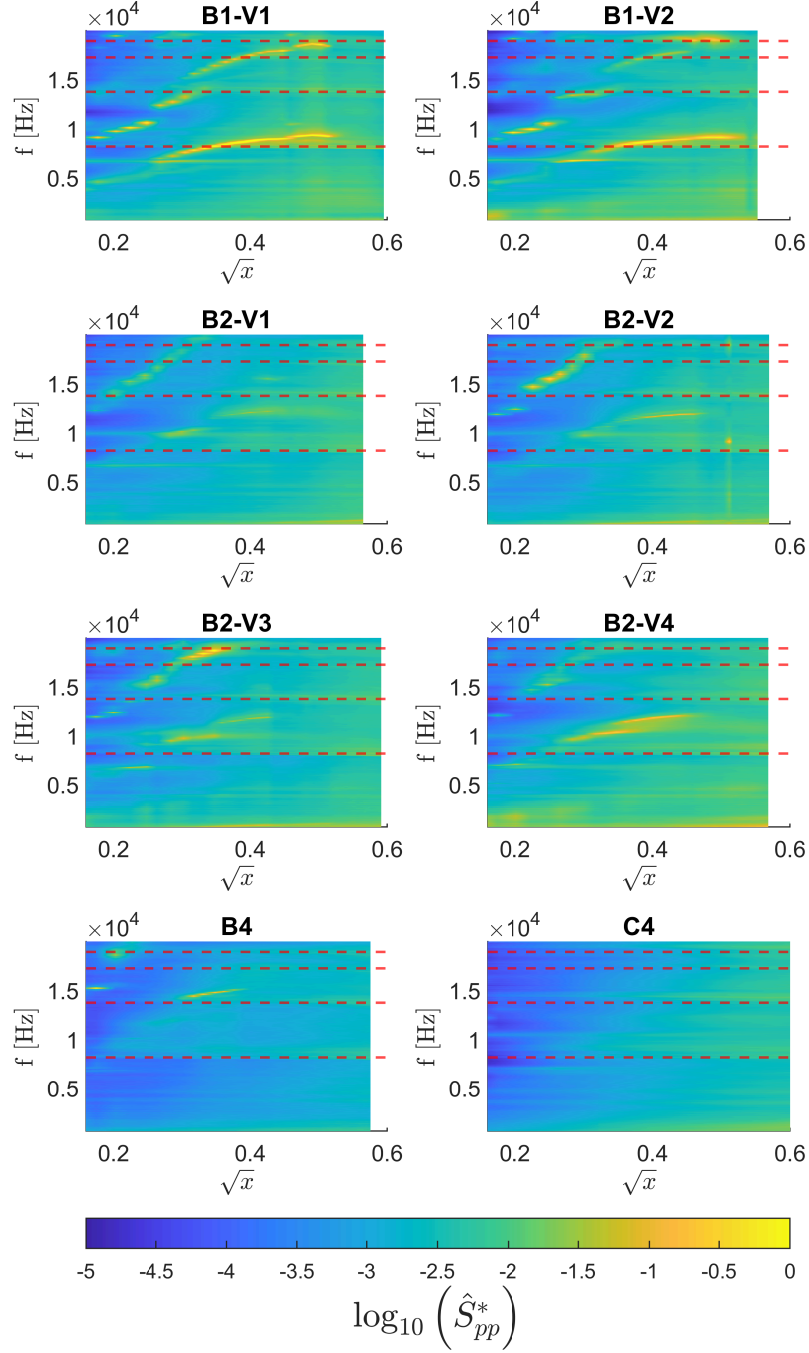


Figure 5.35: Color map of the non-dimensional PSD \hat{S}_{pp}^* at section D-D' for increasing squared root of the relative pressure drop \sqrt{x} for 'B' plates ($t^* = 1$).

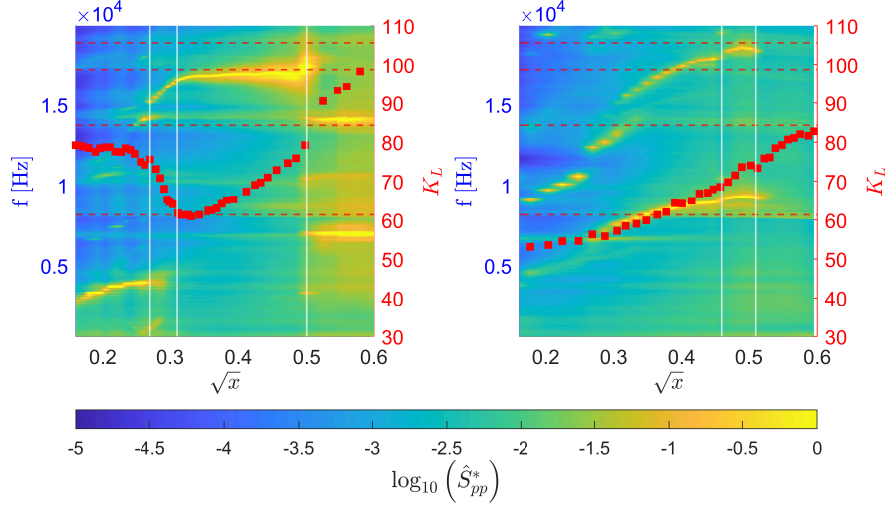


Figure 5.36: Resistance coefficient K_L superposed on the colour map of the non-dimensional PSD \hat{S}_{pp}^* at section D-D' for increasing squared root of the relative pressure drop \sqrt{x} for A1-V1 plate (left) and for B1-V1 plate (right).

No general remarks can be made on the whistle frequencies. However, for some geometries, the whistles tend to stabilize with \sqrt{x} in the vicinity of the cut-on frequencies of some modes (e.g. A1-V1, B1-V1, B1-V2).

In order to better understand whether the higher-order modes play any role in such phenomenon, an analysis involving the use of the magnitude-squared coherence $\hat{\gamma}_{s_1, s_2}^2$ and the relative phase $\hat{\theta}_{s_1, s_2}$ information between sensors as done for the C4 plate (5.3.1) is performed. In Figure 5.37, these two quantities between two sensors 180° apart at section E-E' are reported together with the dimensional PSD \hat{S}_{pp} recorded at section D-D' for the case of the B1-V1 plate at $\sqrt{x} = 0.37$, so that the lower whistling frequency almost coincides with that of cut-on of the first higher-order mode (1,0). The same quantities for the C4 plate are also reported for reference. It can be seen that while the drop in $\hat{\gamma}_{s_1, s_2}^2$ starts in the vicinity of the cut-on frequency of the mode (1,0), a recovery up to values around 0.5 occurs. This is in contrast with the drop to almost 0 of the C4 plate, as could be expected from the resonant conditions of the cut-on mode at such frequency. The π phase shift is also retarded with respect to the C4 plate. The second whistle occurs at frequencies of roughly 16.7 kHz. Again, a sharp peak in the value of $\hat{\gamma}_{s_1, s_2}^2$ and a shift in $\hat{\theta}_{s_1, s_2}$ in correspondence of such frequency are visible.

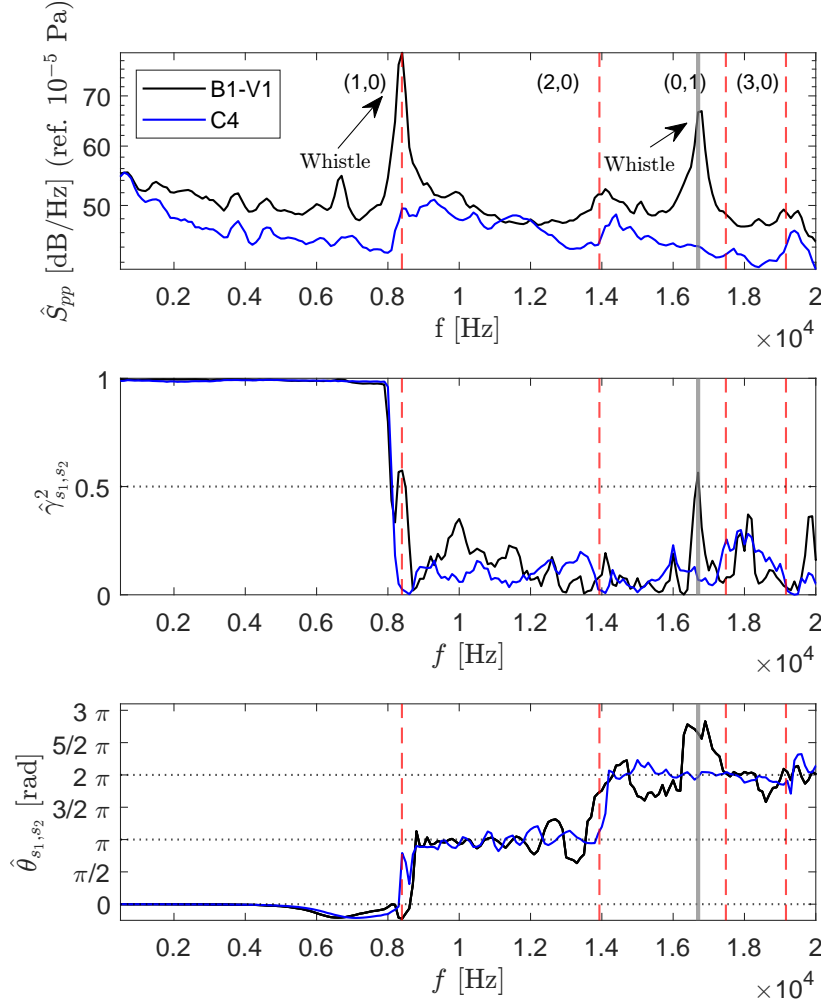


Figure 5.37: Dimensional PSD \hat{S}_{pp}^* for a microphone at section D-D', magnitude-squared coherence $\hat{\gamma}_{s_1, s_2}$ and relative phase $\hat{\theta}_{s_1, s_2}$ between two sensors 180° apart at section E-E'. Frequency resolution of 100 Hz.

5.4 Summary

This chapter dealt with the results of an experimental campaign on aerodynamic noise generation by subsonic flows through perforated plates in a circular pipe. Also, the procedure followed for validating a newly-assembled experimental set-up and its results were reported. All of the plates had the same porosity $\phi = 0.16$ and presented circular, sharp-edged perforations. Three different relative thicknesses t^* (0.4, 1, 2) were tested, with the effect of the number of orifices and their disposition investigated for two values of such parameter ($t^* = 0.4, 1$).

It was shown that the relative thickness t^* plays an important role in determining both the fluid-dynamic and acoustic behavior of the plate. In particular, the only geometry with $t^* = 2$ was also the only plate not to show evidence of whistling in the tested operating conditions. This phenomenon was instead detected for the two thinner plate ‘families’ with $t^* = 0.4, 1$, with increased importance for the case of $t^* = 0.4$.

The excitation of the higher-order modes was evident in the broadband-only noise generation by the thickest plate, as well as their prominent role in causing an enhanced response by the pipe wall in terms of vibrations. Through coherence-based measurements between sensors positioned at the same cross-section, it was inferred that the internal fluctuating pressure field at $\approx 40D_i$ from the obstacle is mainly acoustic in nature. Also, a drop in coherence levels starting from frequencies for which higher-order acoustic modes are propagational and relative phase measurements between the same sensor pairs suggest that such modes are dominant with respect to the plane wave one.

The presence of whistling for the cases of $t^* = 0.4, 1$ impeded the study of the effect of orifice number/disposition on the broadband noise generated by the plates and the possible ‘selective modal excitation’ observed for the incompressible flow case treated in Chapter 4. However, a possible link between the reattachment of the flow within the perforation bore after the *vena contracta* and the whistling behavior was found.

This thesis has dealt with broadband aerodynamic noise generation by perforated plates with circular, sharp-edged orifices in both rectangular and circular ducts, subject to incompressible and weakly compressible flows. The work has been mainly experimental in nature, having involved the use of two different experimental setups owned by two different research groups. In particular, part of the work was devoted to setting up and validating the experimental test bench used at the home institution (Polytechnic University of Milan). Theoretical considerations regarding the dependence on the orifices' disposition of the emitted acoustic power in terms of higher-order modes guided the experimental campaigns. The main findings discussed in the thesis are now summarized and possible research paths for future developments are provided.

6.1 Main findings

In the case of incompressible air flows and rectangular ducts, the orifice disposition and number do have an impact on the modal content of the emitted acoustic power by thin perforated plates. In particular, maximizing the superposition of the orifices' edges with the maxima of the squared cross-sectional distribution of the acoustic pressure of a given propagating higher-order mode favors the amplitude of such mode. Such behavior seems to confirm the fact that the main acoustic source at play is to be found in the pressure fluctuations at the edges of the orifices, as observed for a thin orifice plate in a circular pipe by Tao et al. [37]. A PIV campaign has shown that the (turbulent) velocity fluctuations in the vicinity of the plate's surface are concentrated at the edges of the orifices, on both the upstream and the downstream sides, decreasing exponentially for increasing distances. As such velocity fluctuations can be related to the pressure fluctuations, this is a further confirmation of the results of Tao et al. [37]. An easily computable

‘modal efficiency coefficient’ Ψ_{mn} taking into account the orifice disposition and the modal shape function of mode (m, n) was found to be in qualitative agreement with the obtained results. In particular, it was shown that the plate showing the highest values on average of such coefficient for the propagating modes was also the noisiest geometry.

In the case of subsonic air flows through perforated plates in circular pipes, whistling was observed independently of the orifice number/disposition for plates with relative thicknesses $t^* = 0.4, 1$. The only tested geometry with $t^* = 2$ did not show any evidence of the phenomenon. The presence of whistling impeded to make general considerations on the effect of the orifice number/disposition on broadband noise generation. However, an analysis of the wall pipe pressure fluctuations for the $t^* = 2$ geometry has shown that the newly set up experimental test bench at Polytechnic University of Milan is able to correctly detect the presence of higher-order modes. In fact, it was shown that at a distance of $40D_n$ downstream of the perforated plate the wall pipe pressure fluctuations were mostly acoustic in nature in the frequency range 500 Hz to 20 kHz. Furthermore, for the frequency range for which higher-order modes are propagational, coherence-based measurements indicated that the internal pressure field is dominated by such higher-order modes. An interesting finding related to the thinner ‘whistling’ plates $t^* = 0.4, 1$ is that the changes in whistling frequency were accompanied by changes in the values of the loss coefficient K_L . While no model was applied to explain this behavior, a possible explanation was linked to a change in the ‘flow geometry’ occurring as the flow reattached within the bore of the perforation due to the expanding *vena contracta* as compressibility effects became more important. This was particularly clear for the radially symmetric single-hole geometries, for which the resistance coefficients K_L overlapped for increasing values of the relative pressure drop x .

6.2 Possible developments

An interesting addition to the experimental work relative to the incompressible flow through perforated plates discussed in Chapter 4 would be to extend the analysis to thick plates ($t^* > 0.8$). In fact, no studies relative to the surface pressure fluctuations on the plate for thicker geometries are known to the author. While not directly measuring such pressure fluctuations, a PIV campaign would anyway allow to obtain some information on such quantity, as was shown for the thin plates subject of this study (see 4.3.3). Furthermore, the presence of a clearly-defined recirculating region within the orifice bore could itself influence the modal composition of the produced acoustic power based again on the orifice position within the duct cross-section. Finally, a further study employing the proposed ‘modal

efficiency coefficient' Ψ_{mn} defined in (3.25) could be to produce plates minimizing its value for an increasingly larger number of propagating modes (m, n) within a frequency range for a fixed plate porosity ϕ and number of orifices. As it was shown that orifice disposition (and to a certain extent the number) does not influence greatly the pressure drop characteristics of the device (see 5.3.2), this could allow to study the feasibility of employing Ψ_{mn} to produce a plate generating lower noise with the specified pressure drops characteristics (which are mostly dependent on t^* and ϕ).

Regarding the work on subsonic flows in circular pipes treated in Chapter 5, the obvious addition would be to test the same geometries of the thinner plates ('A' and 'B') with increasing values of t^* . This would allow to identify whether the appearance of whistling is linked to a specific value of t^* , as possibly hinted at by the fact that the only geometry with $t^* = 2$ (plate C4) does not show any evidence of the phenomenon. Furthermore, the 'AirLab' experimental setup could be adapted so as both to correct some of the issues encountered during its validation and make it possible to separate the first few azimuthal higher-order modes. In fact, it was shown that the sensors mounted in a recessed configuration 90° apart at the same cross-section at $40D$ downstream of the tested device suffered from the presence of an acoustic resonance (see 5.2). This resonance was linked to a clearance between the sensor's head and its seat of roughly 0.5 mm. If such value was accepted as constant, increasing the diameter of the neck of the recessed installation would allow to correct the issue by increasing the neck-to-chamber volume ratio. For high enough values, (5.7) would be valid and the 'design' resonance frequency of 25.2 kHz should be obtained instead of the measured one at roughly 6.4 kHz. The information of the three sensors at 90° apart could then be used to separate the contribution to the total acoustic pressure field by the first two azimuthal modes (1,0) and (2,0) through the 'time average' separation method as described by Kerschen [70]. The addition of a fourth sensor at the same cross-section would also in principle allow to extend the analysis to include the (3,0) and (4,0) modes [40].

Bibliography

1. Baines, A. *Woodwind instruments and their history* Unabr. republ. of the 3. ed. eng. ISBN: 978-0-486-26885-9 (Dover, New York, 1991).
2. Lele, S. K. & Nichols, J. W. A second golden age of aeroacoustics? en. *Philosophical Transactions of the Royal Society A: Mathematical, Physical and Engineering Sciences* **372**, 20130321. ISSN: 1364-503X, 1471-2962. <https://royalsocietypublishing.org/doi/10.1098/rsta.2013.0321> (2023) (Aug. 2014).
3. Reethof, G. Turbulence-Generated Noise in Pipe Flow. en. *Annual Review of Fluid Mechanics* **10**, 333–367. ISSN: 0066-4189, 1545-4479. <https://www.annualreviews.org/doi/10.1146/annurev.fl.10.010178.002001> (2022) (Jan. 1978).
4. Miller, D. S. *Internal flow systems* Reprint. eng. *BHRA Fluid Engineering Series* **5**. ISBN: 978-0-900983-78-8 (BHRA Fluid Engineering, Cranfield, 1984).
5. Lighthill, M. J. On sound generated aerodynamically I. General theory. en. *Proceedings of the Royal Society of London. Series A. Mathematical and Physical Sciences* **211**, 564–587. ISSN: 0080-4630, 2053-9169. (2022) (Mar. 1952).
6. Lighthill, M. J. On sound generated aerodynamically II. Turbulence as a source of sound. en. *Proceedings of the Royal Society of London. Series A. Mathematical and Physical Sciences* **222**, 1–32. ISSN: 0080-4630, 2053-9169. <https://royalsocietypublishing.org/doi/10.1098/rspa.1954.0049> (2022) (Feb. 1954).
7. Norton, M. & Karczub, D. *Fundamentals of Noise and Vibrations for Engineers* 2nd. en (Cambridge University Press, 2003).

-
8. Doak, P. Excitation, transmission and radiation of sound from source distributions in hard-walled ducts of finite length (I): The effects of duct cross-section geometry and source distribution space-time pattern. en. *Journal of Sound and Vibration* **31**, 1–72. ISSN: 0022460X. (2022) (Nov. 1973).
 9. Norton, M. & Bull, M. Mechanisms of the generation of external acoustic radiation from pipes due to internal flow disturbances. en. *Journal of Sound and Vibration* **94**, 105–146. ISSN: 0022460X. <https://linkinghub.elsevier.com/retrieve/pii/S0022460X84800085> (2022) (May 1984).
 10. Reader-Harris, M. *Orifice Plates and Venturi Tubes* en. ISBN: 978-3-319-16879-1 978-3-319-16880-7. <http://link.springer.com/10.1007/978-3-319-16880-7> (2022) (Springer International Publishing, Cham, 2015).
 11. Idelcik, I. E., Ginevskij, A. S. & Idelčik, I. E. *Handbook of hydraulic resistance* 4., rev. and augmented ed. en. ISBN: 978-1-56700-251-5 (Begell House, Redding, Conn., 2007).
 12. Malavasi, S., Messa, G., Fratino, U. & Pagano, A. On the pressure losses through perforated plates. en. *Flow Measurement and Instrumentation* **28**, 57–66. ISSN: 09555986. (2022) (Dec. 2012).
 13. Adam, N. J., De Cesare, G. & Schleiss, A. J. Influence of geometrical parameters of chamfered or rounded orifices on head losses. en. *Journal of Hydraulic Research* **57**, 263–271. ISSN: 0022-1686, 1814-2079. <https://www.tandfonline.com/doi/full/10.1080/00221686.2018.1454518> (2022) (Mar. 2019).
 14. Ward-Smith, A. Critical flowmetering: The characteristics of cylindrical nozzles with sharp upstream edges. en. *International Journal of Heat and Fluid Flow* **1**, 123–132. ISSN: 0142727X. <https://linkinghub.elsevier.com/retrieve/pii/0142727X79900286> (2022) (Sept. 1979).
 15. Maynes, D., Holt, G. J. & Blotter, J. Cavitation Inception and Head Loss Due to Liquid Flow Through Perforated Plates of Varying Thickness. en. *Journal of Fluids Engineering* **135**, 031302. ISSN: 0098-2202, 1528-901X. <https://asmedigitalcollection.asme.org/fluidsengineering/article/doi/10.1115/1.4023407/373987/Cavitation-Inception-and-Head-Loss-Due-to-Liquid> (2022) (Mar. 2013).
 16. Lichtarowicz, A., Duggins, R. K. & Markland, E. Discharge Coefficients for Incompressible Non-Cavitating Flow through Long Orifices. en. *Journal of Mechanical Engineering Science* **7**, 210–219. ISSN: 0022-2542, 2058-3389. http://journals.sagepub.com/doi/10.1243/JMES_JOUR_1965_007_029_02 (2022) (June 1965).
-

-
17. Durrieu, P. *et al.* Quasisteady aero-acoustic response of orifices. en. *The Journal of the Acoustical Society of America* **110**, 1859–1872. ISSN: 0001-4966. (2022) (Oct. 2001).
 18. Binder, C. *et al.* Experimental Study on Pressure Losses in Circular Orifices for the Application in Internal Cooling Systems. en. *Journal of Turbomachinery* **137**, 031005. ISSN: 0889-504X, 1528-8900. <https://asmedigitalcollection.asme.org/turbomachinery/article/doi/10.1115/1.4028347/378522/Experimental-Study-on-Pressure-Losses-in-Circular> (2022) (Mar. 2015).
 19. *IEC 60534-2-3: Industrial-process control valves - Part 2-3: Flow capacity - Test procedures* en-fr. 1997.
 20. Papaxanthos, N. *et al.* Pressure-based integral formulations of Lighthill–Curle’s analogy for internal aeroacoustics at low Mach numbers. en. *Journal of Sound and Vibration* **393**, 176–186. ISSN: 0022460X. <https://linkinghub.elsevier.com/retrieve/pii/S0022460X17300536> (2022) (Apr. 2017).
 21. Curle, N. & Lighthill, M. J. The influence of solid boundaries upon aerodynamic sound. *Proceedings of the Royal Society of London. Series A. Mathematical and Physical Sciences* **231**, 505–514 (1955).
 22. Testud, P., Aurégan, Y., Moussou, P. & Hirschberg, A. The whistling potentiality of an orifice in a confined flow using an energetic criterion. en. *Journal of Sound and Vibration* **325**, 769–780. ISSN: 0022460X. <https://linkinghub.elsevier.com/retrieve/pii/S0022460X09002995> (2022) (Sept. 2009).
 23. Manera, J. *et al.* *Kelvin-Helmholtz Instabilities Occurring at a Nacelle Exhaust* en. in *14th AIAA/CEAS Aeroacoustics Conference (29th AIAA Aeroacoustics Conference)* (American Institute of Aeronautics and Astronautics, Vancouver, British Columbia, Canada, May 2008). ISBN: 978-1-60086-983-9. <https://arc.aiaa.org/doi/10.2514/6.2008-2883> (2023).
 24. Rienstra, S. W. & Hirschberg, A. *An Introduction to Acoustics* en. <https://www.win.tue.nl/~sjoerdr/papers/boek.pdf> (2021).
 25. Blake, W. K. *Mechanics of Flow-Induced Sound and Vibration* 2nd ed. eng. ISBN: 978-0-12-809274-3 978-0-12-809273-6 (Academic press, London, 2017).
 26. Ingard, K. U. *Notes on acoustics* en. ISBN: 978-1-934015-08-7 (Infinity Science Press, Hingham, Mass, 2008).
 27. NASA. *Aeroacoustics of Flight Vehicles: Theory and Practice. Volume 2: Noise Control* en (Harvey, Hubbard, Aug. 1991).
-

-
28. Soedel, W. *Vibrations of Shells and Plates* 3rd. en. ISBN: 978-0-429-21627-5. <https://www.taylorfrancis.com/books/9780203026304> (2022) (CRC Press, Aug. 2004).
 29. Bull, M. & Norton, M. The proximity of coincidence and acoustic cut-off frequencies in relation to acoustic radiation from pipes with disturbed internal turbulent flow. en. *Journal of Sound and Vibration* **69**, 1–11. ISSN: 0022460X. <https://linkinghub.elsevier.com/retrieve/pii/0022460X80904307> (2022) (Mar. 1980).
 30. Nelson, P. & Morfey, C. Aerodynamic sound production in low speed flow ducts. en. *Journal of Sound and Vibration* **79**, 263–289. (2022) (Nov. 1981).
 31. Oldham, D. & Ukpoho, A. A pressure-based technique for predicting regenerated noise levels in ventilation systems. en. *Journal of Sound and Vibration* **140**, 259–272. ISSN: 0022460X. (2022) (July 1990).
 32. Gordon, C. G. Spoiler-Generated Flow Noise. II. Results. en. *The Journal of the Acoustical Society of America* **45**, 214–223. ISSN: 0001-4966. <http://asa.scitation.org/doi/10.1121/1.1911359> (2022) (Jan. 1969).
 33. Heller, H. H. & Widnall, S. E. Sound Radiation from Rigid Flow Spoilers Correlated with Fluctuating Forces. en. *The Journal of the Acoustical Society of America* **47**, 924–936. ISSN: 0001-4966. (2022) (Mar. 1970).
 34. De Jong, A. & Golliard, J. *Towards a Universal Scaling for Broadband Turbulent Noise in Internal Flow Devices* en. in *Volume 14: Vibration, Acoustics and Wave Propagation* (American Society of Mechanical Engineers, San Diego, California, USA, Nov. 2013), V014T15A019. ISBN: 978-0-7918-5643-7. (2022).
 35. Kårekull, O., Efraimsson, G. & Åbom, M. Revisiting the Nelson–Morfey scaling law for flow noise from duct constrictions. en. *Journal of Sound and Vibration* **357**, 233–244. ISSN: 0022460X. (2022) (Nov. 2015).
 36. Tao, F. *Experimental Study of Restrictor Noise in Ventilation Duct Systems* en. PhD. thesis (University of Southampton, 2016).
 37. Tao, F. *et al.* Investigation of the sound generation mechanisms for in-duct orifice plates. en. *The Journal of the Acoustical Society of America* **142**, 561–572. (2022) (Aug. 2017).
 38. Davies, H. G. & Williams, J. E. F. Aerodynamic sound generation in a pipe. en. *Journal of Fluid Mechanics* **32**, 765–778. ISSN: 0022-1120, 1469-7645. (2022) (June 1968).
 39. Jenvey, P. Gas pressure reducing valve noise. en. *Journal of Sound and Vibration* **41**, 506–509. ISSN: 0022460X. <https://linkinghub.elsevier.com/retrieve/pii/S0022460X75801143> (2022) (Aug. 1975).
-

-
40. Kerschen, E. & Johnston, J. A modal separation measurement technique for broadband noise propagating inside circular ducts. en. *Journal of Sound and Vibration* **76**, 499–515. ISSN: 0022460X. (2022) (June 1981).
 41. Agarwal, N. The Sound Field In Fully Developed Turbulent Pipe Flow Due To Internal Flow Separation, Part 2: Modal Amplitude And Cut-off Frequencies. en. *Journal of Sound and Vibration* **175**, 65–76. ISSN: 0022460X. (2022) (Aug. 1994).
 42. Laffay, P., Moreau, S., Jacob, M. & Regnard, J. Experimental study of the noise radiated by an air flow discharge through diaphragms and perforated plates. en. *Journal of Sound and Vibration* **434**, 144–165. ISSN: 0022460X. <https://linkinghub.elsevier.com/retrieve/pii/S0022460X18304802> (2022) (Nov. 2018).
 43. Laffay, P., Moreau, S., Jacob, M. & Regnard, J. Experimental investigation of the noise radiated by a ducted air flow discharge through diaphragms and perforated plates. en. *Journal of Sound and Vibration* **472**, 115177. ISSN: 0022460X. (2022) (Apr. 2020).
 44. Mi, J., Kalt, P., Nathan, G. J. & Wong, C. Y. PIV measurements of a turbulent jet issuing from round sharp-edged plate. en. *Experiments in Fluids* **42**, 625–637. ISSN: 0723-4864, 1432-1114. (2022) (Mar. 2007).
 45. Trabelsi, H. *Banc d’essai et procédure pour la caractérisation des éléments d’un SCA par un système* PhD Thesis (2011). <http://www.theses.fr/2011COMP1924>.
 46. Trabelsi, H., Zerbib, N., Ville, J.-M. & Foucart, F. Passive and active acoustic properties of a diaphragm at low Mach number: Experimental procedure and numerical simulation. en. *European Journal of Computational Mechanics* **20**, 49–71. ISSN: 1779-7179, 1958-5829. (2022) (Jan. 2011).
 47. David, A., Hugues, F., Dauchez, N. & Perrey-Debain, E. Vibrational response of a rectangular duct of finite length excited by a turbulent internal flow. en. *Journal of Sound and Vibration* **422**, 146–160. ISSN: 0022460X. (2022) (May 2018).
 48. Lavrentjev, J. & Åbom, M. CHARACTERIZATION OF FLUID MACHINES AS ACOUSTIC MULTI-PORT SOURCES. en. *Journal of Sound and Vibration* **197**, 1–16. ISSN: 0022460X. <https://linkinghub.elsevier.com/retrieve/pii/S0022460X96905143> (2022) (Oct. 1996).
 49. Åbom, M. Modal decomposition in ducts based on transfer function measurements between microphone pairs. en. *Journal of Sound and Vibration* **135**, 95–114. ISSN: 0022460X. <https://linkinghub.elsevier.com/retrieve/pii/0022460X89907578> (2022) (Nov. 1989).

-
50. Bendat, S. J. & Piersol, A. G. *Random Data: Analysis and Measurement Procedures* 4th. en (Wiley, 2010).
 51. Lavrentjev, J., Åbom, M. & Bodén, H. A measurement method for determining the source data of acoustic two-port sources. en. *Journal of Sound and Vibration* **183**, 517–531. ISSN: 0022460X. (2022) (June 1995).
 52. Kirkwood, A. *Aerodynamic noise generation in control valves* en. PhD. thesis (University of Manchester, Manchester, 1992).
 53. Raffel, Willert, Wereley & Kompenhans. *Particle image velocimetry: a practical guide* 2nd ed. en. ISBN: 978-3-540-72307-3 (Springer, Berlin, 2007).
 54. Prasad, A. K. Particle Image Velocimetry. *Current Science* **79**, 51–60 (2000).
 55. Dickey, N. S., Selamet, A. & Ciray, M. S. An experimental study of the impedance of perforated plates with grazing flow. en. *The Journal of the Acoustical Society of America* **110**, 2360–2370. ISSN: 0001-4966. <http://asa.scitation.org/doi/10.1121/1.1400736> (2023) (Nov. 2001).
 56. Bendat, J. S. & Piersol, A. G. *Engineering applications of correlation and spectral analysis* 2. ed., rev. and expanded. eng. ISBN: 978-0-471-57055-4 (Wiley, New York, 1993).
 57. Åbom, M., Allam, S. & Boij, S. *Aero-Acoustics of Flow Duct Singularities at Low Mach Numbers* en. in *12th AIAA/CEAS Aeroacoustics Conference (27th AIAA Aeroacoustics Conference)* (American Institute of Aeronautics and Astronautics, Cambridge, Massachusetts, May 2006). ISBN: 978-1-62410-021-5.
 58. Mak, C. & Oldham, D. The Application of Computational Fluid Dynamics to the Prediction of Flow Generated Noise in Low Speed Ducts. Part 1: Fluctuating Drag Forces on a Flow Spoiler. en. *Building Acoustics* **5**, 123–141. ISSN: 1351-010X, 2059-8025. (2022) (June 1998).
 59. Mak, C. M. & Au, W. M. A turbulence-based prediction technique for flow-generated noise produced by in-duct elements in a ventilation system. en. *Applied Acoustics* **70**, 11–20. ISSN: 0003682X. (2022) (Jan. 2009).
 60. Fenini, L. *Numerical modelling of flow-induced noise emitted by control devices* en. PhD Thesis (Politecnico di Milano, 2019).
 61. *IEC 60534-8-3: Industrial-process control valves - Part 8-3: Noise considerations - Control valve aerodynamic noise prediction method* en-fr. 2010.
-

-
62. Goody, M. Empirical Spectral Model of Surface Pressure Fluctuations. en. *AIAA Journal* **42**, 1788–1794. ISSN: 0001-1452, 1533-385X. <https://arc.aiaa.org/doi/10.2514/1.9433> (2023) (Sept. 2004).
 63. Durant, C. *Etude expérimentale de l'excitation et de la réponse vibroacoustique d'une conduite sollicitée par un écoulement interne* fr. PhD. thesis (École Centrale de Lyon, 1999).
 64. Corcos, G. M. Resolution of Pressure in Turbulence. en. *The Journal of the Acoustical Society of America* **35**, 192–199. ISSN: 0001-4966. <http://asa.scitation.org/doi/10.1121/1.1918431> (2023) (Feb. 1963).
 65. Schewe, G. On the structure and resolution of wall-pressure fluctuations associated with turbulent boundary-layer flow. en. *Journal of Fluid Mechanics* **134**, 311. ISSN: 0022-1120, 1469-7645. http://www.journals.cambridge.org/abstract_S0022112083003389 (2023) (Sept. 1983).
 66. Walter, P. L. *Air Blast and the Science of Dynamic Pressure Measurements* en. Technical Notes TN-31 (PCB Piezotronics).
 67. Deckker, B. E. L. & Chang, Y. F. Paper 7: An Investigation of Steady Compressible Flow through Thick Orifices. en. *Proceedings of the Institution of Mechanical Engineers, Conference Proceedings* **180**, 312–323. ISSN: 0367-8849, 2058-3362. http://journals.sagepub.com/doi/10.1243/PIME_CONF_1965_180_307_02 (2022) (June 1965).
 68. Solomon, O. J. *PSD Computations Using Welch's Method* Technical report SAND91-1533 (Albuquerque, New Mexico 87185 and Livermore, California 94550, 1991).
 69. Kerschen, E. & Johnston, J. Modal content of noise generated by a coaxial jet in a pipe. en. *Journal of Sound and Vibration* **76**, 95–115. ISSN: 0022460X. <https://linkinghub.elsevier.com/retrieve/pii/S0022460X81902947> (2022) (May 1981).
 70. Kerschen, E. & Johnston, J. *Modal Content Noise Generated by a Coaxial Jet in a Pipe* en. 1978.
 71. Of America, I. S. *Considerations for evaluating control valve cavitation* en. OCLC: 1064844027. ISBN: 978-1-55617-572-5 (Instrument Society of America, Research Triangle Park, N.C., 1995).
 72. Malavasi, S., Rossi, M. M. A. & Ferrarese, G. GreenValve: hydrodynamics and applications of the control valve for energy harvesting. en. *Urban Water Journal* **15**, 200–209. ISSN: 1573-062X, 1744-9006. <https://www.tandfonline.com/doi/full/10.1080/1573062X.2016.1175483> (2022) (Mar. 2018).
-

-
73. Boffi, P. *et al.* Coherent optical fiber interferometric sensor for incipient cavitation index detection. en. *Flow Measurement and Instrumentation* **66**, 37–43. ISSN: 09555986. <https://linkinghub.elsevier.com/retrieve/pii/S0955598618300943> (2022) (Apr. 2019).
74. Chaves, H., Knapp, M., Kubitzek, A., Obermeier, F. & Schneider, T. Experimental Study of Cavitation in the Nozzle Hole of Diesel Injectors Using Transparent Nozzles. en. *SAE Technical Paper 950290*, 950290. <https://www.sae.org/content/950290/> (2022) (Feb. 1995).

Appendices



Appendix: ‘liquid pressure recovery factor’ calculation

In the present Appendix, the experimental setup and the procedure for the determination of the ‘liquid pressure recovery factor’ F_L defined in Chapter 2 is described. Then, the results for the circular perforated plates subject of the study in Chapter 5 are presented. Some comments on the behavior of the ‘transitional’ geometry A1-V1 are finally provided.

A.1 Experimental setup and methods

The determination of the F_L is carried out on the ‘Control Valve’ experimental setup located at the ‘G. Fantoli’ Hydraulics’ Laboratory of the Polytechnic University of Milan. Such experimental bench is an hydraulic circuit designed for the testing of control valves as specified by the international standards ISARP 75.02.0 and IEC 60534-2-3 [61, 71] and has been employed in a number of other works [72, 73].

Referring to Figure A.1, water is drawn from an elevated tank (≈ 13 m above the test section) to a control section made up of two stainless steel pipes of 1 inch nominal diameter D and different lengths flanged together through the perforated plate under test. The flow is regulated by a valve positioned sufficiently far downstream of the tested device so as not to affect the results. The water is then collected by a large reservoir at a lower level than the test section to allow for low pressures to develop downstream of the plate. A pump connecting the upper and the lower reservoirs permits recirculating the water. To attain higher pressures upstream of the perforated plate, a pressure-boost system can be added between the elevated tank and the test section.

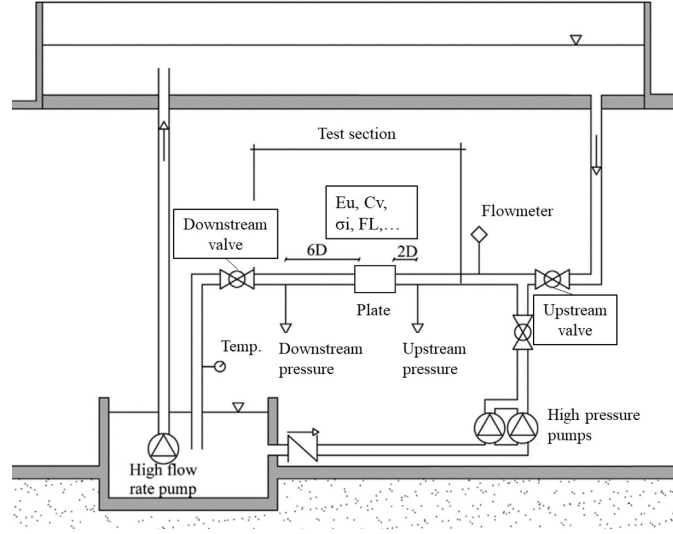


Figure A.1: Scheme of ‘Control Valve’ experimental test bench.

The absolute pressure $2D$ upstream of the perforated plates is measured through a pressure transducer (KPT DF3A60) with an accuracy of 0.1% of its set full scale (FS), which for this case is set to 10 bars. The pressure drop caused by the device is evaluated by a differential pressure transducer (SDT - SGM Lektra) between the same upstream pressure tap used for the absolute pressure and another located $6D$ downstream of the tested plate. The accuracy of such instrument is 0.075% of its FS, which is again set to 10 bars. A magnetic flowmeter (Toshiba LF400) is installed to measure the volumetric flowrate Q with an accuracy of 0.2% of its FS if in the range 0-50% of FS or with an accuracy of 0.4% of its FS if in the range 50-100% of FS. A piezo-electric shear accelerometer (PCB 352A60) is rigidly mounted on the pipe wall at one diameter downstream of the tested device as recommended in [71] for the measurement of the wall pipe vibrations. The data from the pressure transducers and the flowmeter are acquired through a National Instruments module with a sampling frequency of 100 Hz for a duration of 30 s. All such measurements are then averaged over the recorded time history. The data from the accelerometer are instead sampled at 51200 Hz through another module for a duration of 3 s.

A.1.1 Determination of F_L

The standard IEC 60534-2-3 provides an expression of the ‘liquid pressure recovery factor’ as a function of the maximum (volumetric) flow rate Q_{max} and the dimensional ‘flow coefficient’ C_V for a fixed inlet static pressure $p_{1,s}$, see (2.19).

To determine Q_{max} , the flow rate Q^I with the downstream throttling valve completely open is recorded. Then, another test is performed after reducing by 10% the pressure differential $\Delta p_R = p_{1,s} - p_{2,s}$ and maintaining a constant upstream pressure $p_{1,s}$. If the flow rate Q^{II} measured in this case is within 2% of Q^I , then $Q^I = Q_{max}$. In this condition, a fully cavitating flow have been reached and the flow is choked.

The determination of C_V is done by recording the flow rate Q at various openings of the downstream throttling valve, causing different pressure drops Δp_R . Plotting Q against $\sqrt{\Delta p_R}$ allows to identify the region for which such relationship is linear, corresponding to a constant resistance coefficient K_L (see 2.1.2). The slope of a ‘best fit’ line in such region then corresponds to the ‘flow coefficient’ C_V , except for a constant conversion term depending on the dimensional units chosen for Q and Δp_R . In the present work, unless specified, all tests are performed starting from the fully open position for the downstream throttling valve and gradually closing it to obtain closely spaced pressure drops Δp_R .

The standard IEC 60534-2-3 [19] states that the procedure specified allows to retrieve the sizing coefficients with an uncertainty of $\pm 5\%$. Validations of the experimental setup have confirmed the estimates [12].

A.1.2 Test conditions

The thinner ‘A’ geometries and the ‘thick’ plate C4 have been tested by imposing a constant absolute upstream pressure $p_{1,s} = 9$ barA. The ‘B’ plates have instead been tested with a constant upstream pressure of 6 barA. The higher value for the ‘A’ geometries was required in order to obtain a large enough flow rate Q so that fully cavitating conditions could be reached. The use of the same upstream pressure for the C4 geometry is simply due to the test being performed during the same experimental campaign for the ‘A’ plates. As long as the upstream absolute pressure is high enough ($p_{1,s}^{min} = 1.9$ barA in the most conservative specifications by the standard), its value does not influence the result.

A.2 Results and discussion

The results obtained for all geometries tested are reported in Table A.1. The loss coefficient K_L computed through (2.21) from the C_V is also reported for reference and comparison with the values obtained in the compressed air experimental plant and discussed in Chapter 5. The data points relative to such values are plotted as Q versus $\sqrt{\Delta p_R}$ in Figure A.2, Figure A.3 and Figure A.4 respectively for the ‘A’ geometries, the ‘B’ ones and the C4 plate. The fitting lines for the computation of the ‘flow coefficient’ C_V are

also reported. For lower values of $\sqrt{\Delta p_R}$, the linearity of the relationship Q versus $\sqrt{\Delta p_R}$ is evident. However, while for the thicker plates ‘B’ and C4 the loss of such linearity is abrupt when cavitating conditions occur, for the case of the ‘A’ plates the shift to choking is preceded by a more gradual change. This leads to some issues in computing the F_L , as the formula (2.19) suggested by the standard IEC 60534-2-3 employs the average C_V in the non-cavitating region. The presence of a transitional ‘linear’ region makes the expression (2.19) more difficult to be applied correctly. However, following some remarks discussed in A.2.1, it has been decided to report the results by considering only the C_V relative to the first linear region.

Plate ID	K_L [-]	C_V [gpm/psi ^{0.5}]	F_L [-]
A1-V1	76.29	3.13	0.8866
A1-V2	77.54	3.10	0.9096
A2-V1	83.86	2.98	0.8651
A2-V2	69.55	3.28	0.8777
A2-V3	73.28	3.19	0.8923
A2-V4	76.06	3.13	0.9032
A4	67.30	3.33	0.8810
B1-V1	51.30	3.82	0.7076
B1-V2	51.61	3.80	0.7205
B2-V1	46.66	4.00	0.7066
B2-V2	48.61	3.92	0.7135
B2-V3	49.04	3.90	0.7229
B2-V4	48.15	3.94	0.7319
B4	44.08	4.12	0.7107
C4	46.13	4.02	0.6891

Table A.1: Summary of the results of the experimental campaign on the ‘Control Valve’ hydraulic loop.

The values of K_L are in close agreement with those obtained in the ‘AirLab’ experimental plant for low values of \sqrt{x} (for which compressibility can still be neglected) in Figure 5.20 and Figure 5.31. The orifice disposition and number has a limited effect on the values of C_V and K_L , while the relative thickness t^* affects the results more considerably. In particular, varying t^* from 0.4 to 1 and maintaining a constant geometry produces a decrease in K_L of roughly 25% on average and an increase in C_V of roughly 33%. A further increase of t^* from 1 to 2 does not seem to produce any appreciable change in both values, but evidence is limited only to the C4 geometry, which has slightly different positions of the orifices with respect to B4 and A4. This result would however have to be expected if the flow were fully reattached flow within the perforation for both plates, as is the case with

$t^* = 1$ and $t^* = 2$.

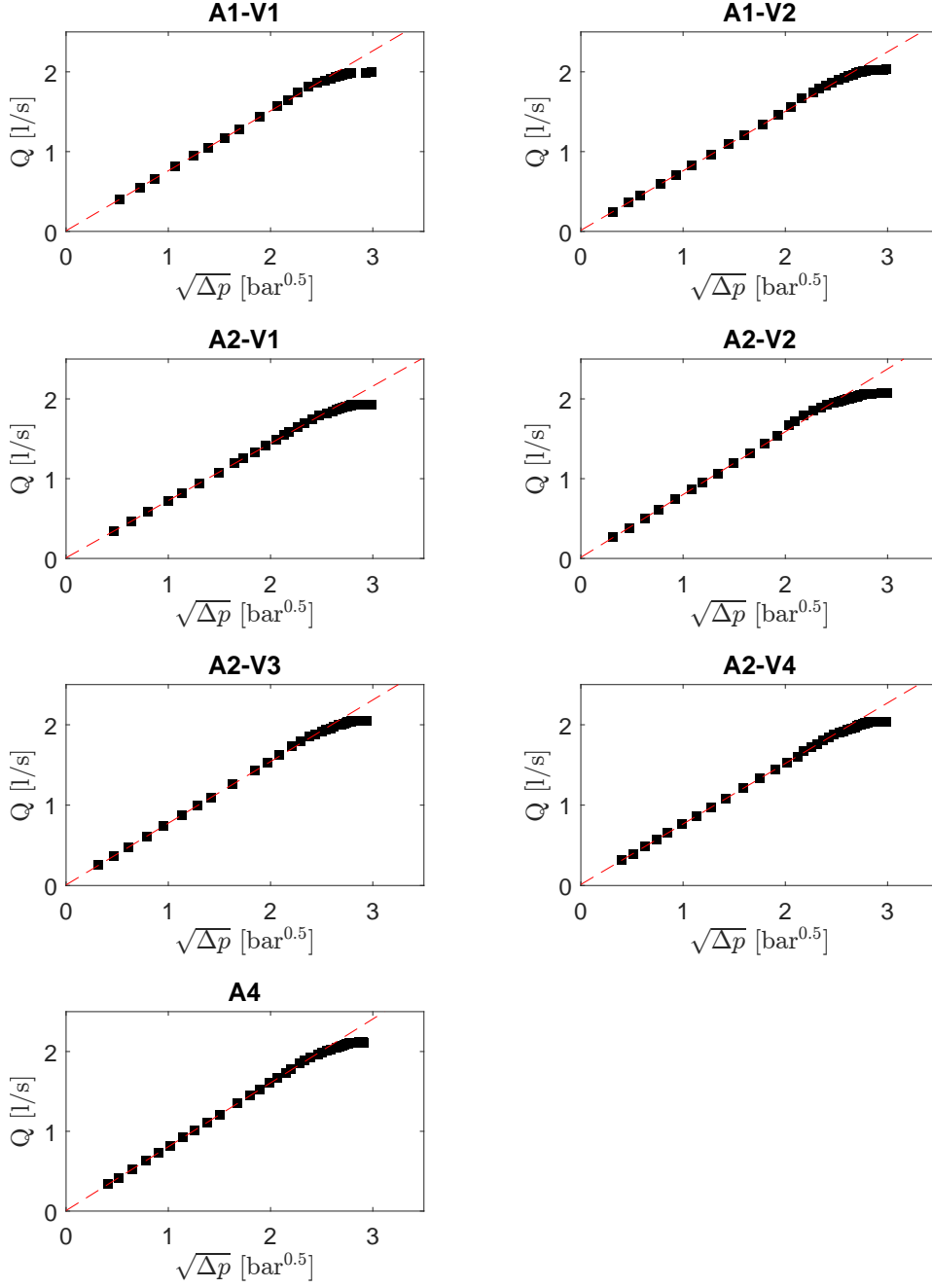


Figure A.2: Flow rate Q versus squared root of the pressure drop $\sqrt{\Delta p_R}$ between $2D$ upstream of the ‘A’ plates and $6D$ downstream for different openings of the downstream throttling valve and an absolute upstream pressure of $p_{1,s} = 9 \text{ barA}$. Fitting line for computing C_V is highlighted in red.

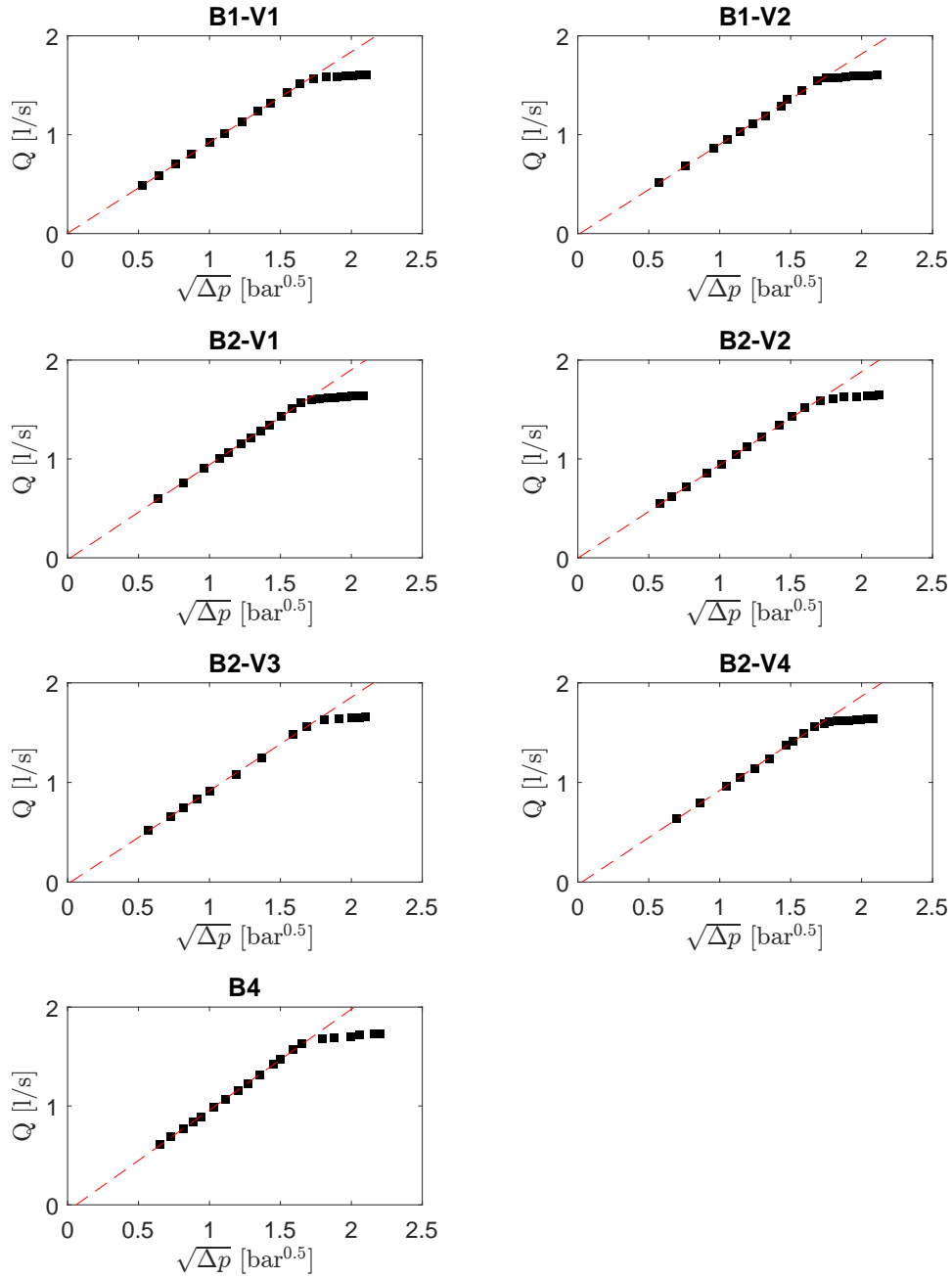


Figure A.3: Flow rate Q versus squared root of the pressure drop $\sqrt{\Delta p_R}$ between $2D$ upstream of the ‘B’ plates and $6D$ downstream for different openings of the downstream throttling valve and an absolute upstream pressure of $p_{1,s} = 6 \text{ barA}$. Fitting line for computing C_V is highlighted in red.

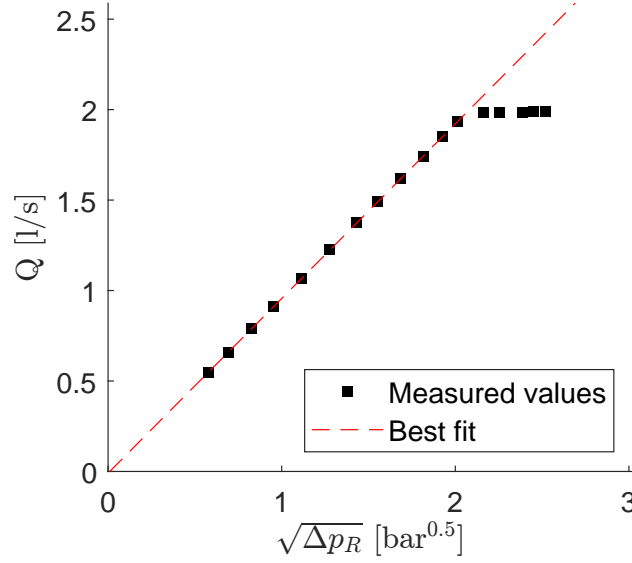


Figure A.4: Flow rate Q versus squared root of the pressure drop $\sqrt{\Delta p_R}$ between $2D$ upstream of the C4 plate and $6D$ downstream for different openings of the downstream throttling valve and an absolute upstream pressure of $p_{1,s} = 9$ barA. Fitting line for computing C_V is highlighted in red.

A.2.1 Cavitating behavior of A1-V1 plate

To further investigate the behavior observed for the ‘A’ geometries, the A1-V1 plate was tested under an additional two different constant upstream pressures $p_{1,s}$ (5 barA and 7 barA) and the measured loss coefficient K_L was plotted as a function of the ‘cavitation number’ σ , defined as [71]:

$$\sigma = \frac{p_{1,s} - p_{vap}}{p_{1,s} - p_{2,s}} = \frac{p_{1,s} - p_{vap}}{\Delta p_R} \quad (\text{A.1})$$

where the saturated vapor pressure p_{vap} is set to 0.015 bar relative to water at 15 °C. The cavitation number σ represents the ratio of the effects promoting cavitation (the lower the difference $p_{1,s} - p_{vap}$ the closer the liquid is to boiling) and the effects counteracting it (the higher $p_{2,s}$, the higher will be $p_{vc,s}$) [74]. The results are reported in Figure A.5 both as a function of the pipe Reynolds number Re_p and of σ . From the plot of K_L versus Re_p , it can be seen that after an initial dependence, K_L becomes independent of Re_p , i.e. self-similarity is reached. Afterwards, before showing a steep increase with Re_p , a localized drop is observed for all upstream pressures. If K_L is reported against the cavitation number σ , a good collapse is obtained between the curves relative to the different upstream pressures. This indicates that cavitation is involved in the observed behavior.

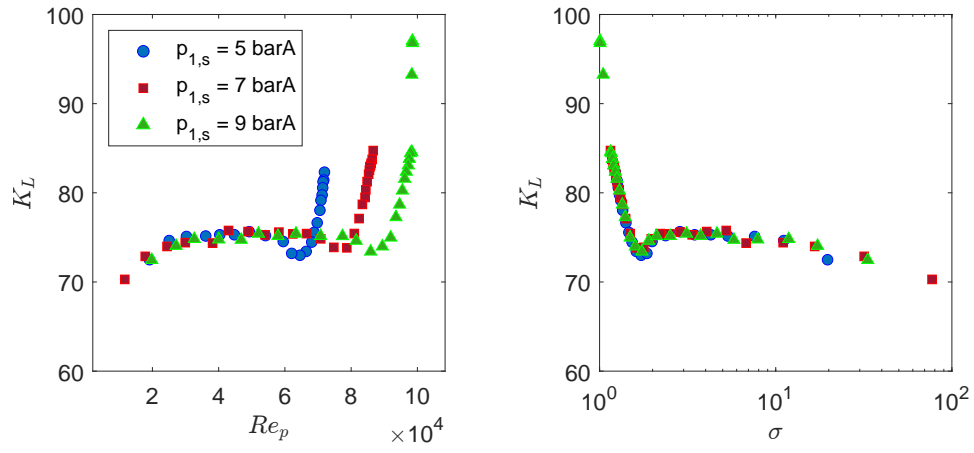


Figure A.5: Trend of loss coefficient K_L against pipe Reynolds number Re_p and cavitation number σ for plate A1-V1 subject to different upstream pressures $p_{1,s}$.

Appendix: recessed sensors characterization

The design of the three piezoelectric dynamic pressure sensors at section E-E' of the AirLab test bench presented in Chapter 5 suggests a preferred method of installation as flush with the inner surface of the pipe. Due to the excessive dimension of the sensors' diaphragm (1/4 in.) relative to the pipe's internal diameter (1 in.), it was decided during the course of the present thesis to install the sensors in a 'recessed' configuration (see Fig. 5.13). In the present Appendix, the procedure followed to further characterize the custom recessed installation of the sensors is described and the results are presented.

B.1 Experimental setup and methods



Figure B.1: External acoustic source (loudspeaker) installed at the upstream end of the downstream pipe of the AirLab's test line.

The characterization of the PCB sensors is performed using an external source. A tweeter compression driver (beyma CD10Fe) of 1 in. diameter and rated for a frequency range between 1-18 kHz is placed on the upstream

end of the downstream test section so that the speaker of the compression driver occupies the pipe's cross section (Fig. B.1). Leakage was prevented by sealing the loudspeaker's borders with a multipurpose putty adhesive. The loudspeaker is powered by an amplifier board (Fosi Audio ZK-1002L) with a 24 V DC power supply; the gain can be set through a handle on the board.

A Gaussian white noise signal $V_1(t)$ is fed into the power amplifier over the operative frequency range of the loudspeaker (1-18 kHz) and the output signals $V_{2,i}(t)$ of the PCB sensors are recorded in order to estimate their frequency responses $\hat{H}_{PCB,i}$. The system composed of the power amplifier, the loudspeaker and the pipe however modifies the input signal $V_1(t)$ so that the output sound pressure emitted by the loudspeaker within the pipe $P(t)$ is not anymore a 'pure' Gaussian white noise. To retrieve the filtering effect of such system (i.e., its frequency response function or FRF, $\hat{H}_{amp+LS+pipe}$), the flush mounted GRAS2 microphone installed at $9D_n$ downstream of the loudspeaker is used to measure $P(t)$ assuming that its FRF is flat over the frequency range of interest (i.e., no distortion or delay is added by the microphone to the measured signal). This hypothesis should be considered as valid as the flatness of the microphone's frequency response is specified by the manufacturer and its flush installation within the pipe is obtained by means of an adapter also produced by the manufacturer. The measurement chain for the PCB sensors can be graphically represented as the block diagram in Fig.B.2.

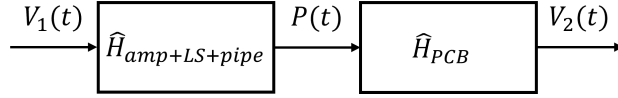


Figure B.2: Block diagram of PCB piezoelectric sensors measurement chain.

Through FRF algebra, the overall FRF of the system \hat{H}_{sys} transforming the signal $V_1(t)$ into the signals $V_{2,i}(t)$ is given by [56]:

$$\hat{H}_{sys,i} = \hat{H}_{amp+LS+pipe} \cdot \hat{H}_{PCB,i} \quad (B.1)$$

The frequency response of the sub-system composed of the power amplifier, the loudspeaker and the pipe $\hat{H}_{amp+LS+pipe}$ can be computed as [50]:

$$\hat{H}_{amp+LS+pipe} = \frac{\hat{S}_{PV_1}}{\hat{S}_{V_1V_1}} \quad \left[\frac{Pa}{V} \right] \quad (B.2)$$

where \hat{S}_{PV_1} is the cross-power spectral density of the input signal $V_1(t)$ (in V) and the measured signal by the GRAS2 microphone $P(t)$ (in Pa) while $\hat{S}_{V_1V_1}$ is the power spectral density of the input signal $V_1(t)$. Through the

same logic, the overall frequency response of the system starting from the input signal $V_1(t)$ and the output signal $V_{2,i}(t)$ of the i -th piezoelectric sensor $\hat{H}_{syst,i}$ can be computed as:

$$\hat{H}_{syst,i} = \frac{\hat{S}_{V_{2,i}V_1}}{\hat{S}_{V_1V_1}} \left[\frac{V}{V} \right] \quad (\text{B.3})$$

Finally, the response of each PCB sensor can be obtained from (B.1):

$$\hat{H}_{PCB,i} = \frac{\hat{H}_{syst,i}}{\hat{H}_{amp+LS+pipe}} \left[\frac{V}{Pa} \right] \quad (\text{B.4})$$

The signal is fed for a total time of 45 s and all the analyses in the frequency domain are performed with a frequency resolution of 50 Hz, allowing for roughly 2000 averages for the final results. The PSD of the signal is reported in Fig. B.3.

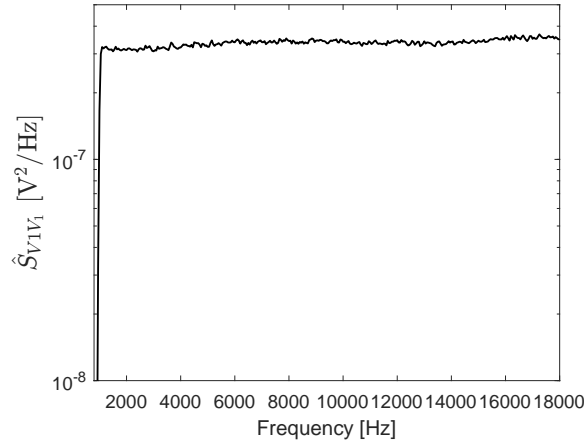


Figure B.3: PSD of Gaussian white noise fed to the loudspeaker. Frequency resolution of 50 Hz.

B.2 Results

The frequency response of the system composed of the power amplifier, the loudspeaker and the pipe ($\hat{H}_{amp+LS+pipe}$) in terms of its gain and phase is reported in Fig. B.4. A first glance at the gain clearly shows how the actual signal produced by the system is different than the input white noise $V_1(t)$ due to the loudspeaker's characteristics.

The frequency responses of the overall measurement chain of the PCB sensors are reported in Fig. B.5 while those obtained through (B.4) for each PCB sensor are reported in Fig. B.6. Focusing on the latter, a few considerations can be made. Regarding the gain, a good superposition between the

sensors is obtained up until frequencies of roughly 9000 Hz. Furthermore, the frequency response of the three instruments is flat in the frequency range 1-4 kHz (except for small fluctuations) and the gain is close to the nominal gain factor of the sensors ($1.45 \cdot 10^{-5}$ V/Pa). After such threshold, a rather broadband peak is observed for all sensors around 6 kHz, with the PCB3 sensor's peak value slightly lower than the remaining two sensors. Considering instead the phase, it is instead clear that the three sensors display the same behavior, with a good superposition of the three curves.

From the above considerations, it can be seen how the three PCB sensors mounted in a recessed configuration have been impacted by installation issues. While any quantitative measurement in terms of amplitude of the pressure fluctuations would be subject to too much of an uncertainty, phase measurements however seem much less sensitive to the installation. This, coupled with the observations in 5.2.2, lead to the choice of employing the sensors only for relative phase measurements.

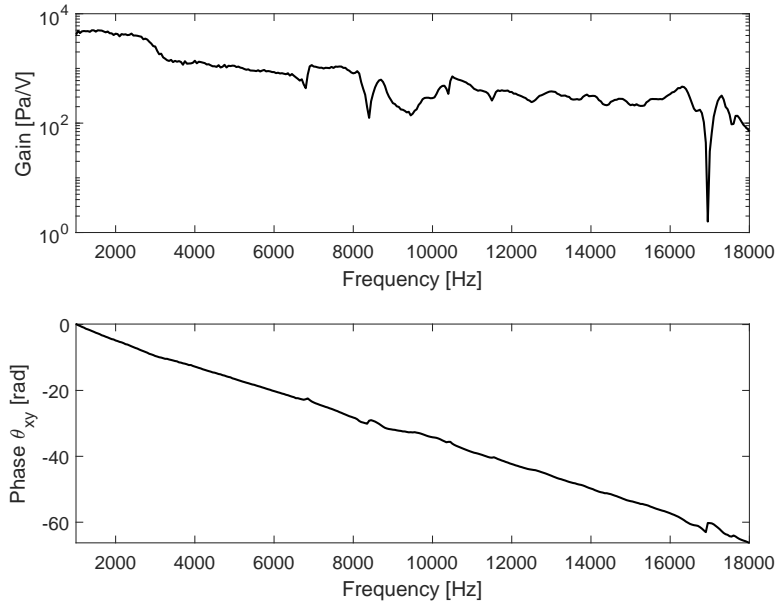


Figure B.4: Frequency response function of the system composed of power amplifier, loudspeaker and pipe within the frequency range 1-18 kHz. Frequency resolution of 50 Hz.

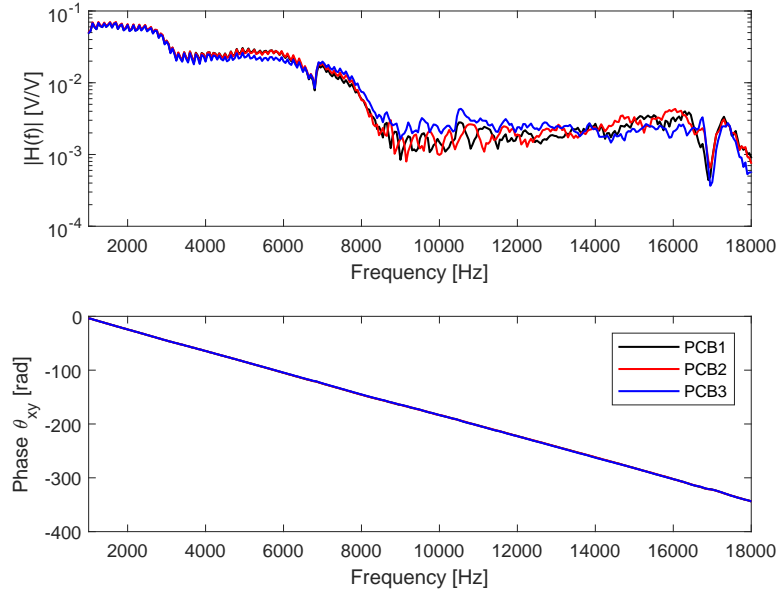


Figure B.5: Frequency response function of the system composed of power amplifier, loudspeaker, pipe and PCB sensors within the frequency range 1-18 kHz. Frequency resolution of 50 Hz.

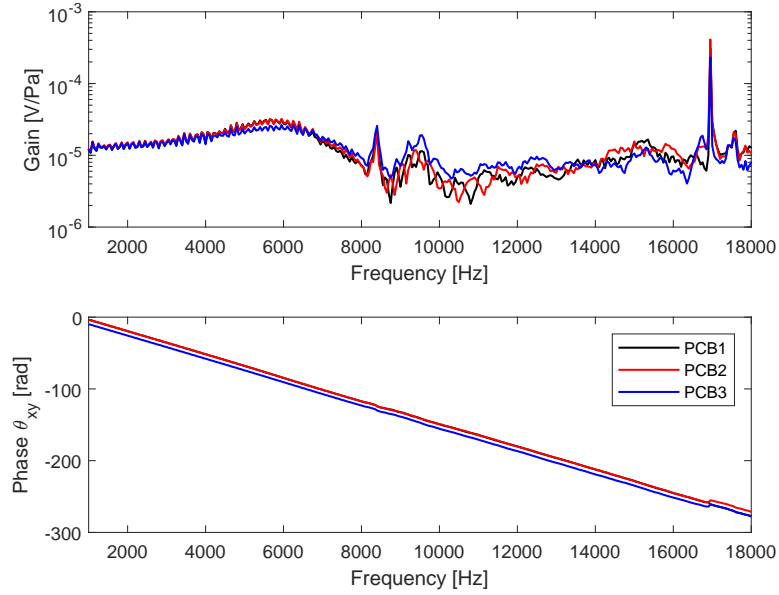


Figure B.6: Frequency response functions of the PCB sensors within the frequency range 1-18 kHz. Frequency resolution of 50 Hz.